The following publication Rare-earth-containing perovskite nanomaterials: design, synthesis, properties and applications. Chemical Society Reviews, 49(4), 1109-1143 is available at https://doi.org/10.1039/C9CS00330D

Rare-earth-containing perovskites nanomaterials: designs, synthesis, properties and applications

Zhichao Zeng[a], Yueshan Xu[a], Zheshan Zhang[a], Zhansheng Gao[a], Meng Luo[a], Chao Zhang[a], Jun Xu[a], Zongyou Yin[b], Feng Luo[a], Bolong Huang*[c], Yaping Du*[a] and Chun-Hua Yan[a,d,e]

As a star material, perovskites have been widely used in the fields of optics, photovoltaics, electronics, magnetics, catalysis, sensing, etc. However, some inherent shortcomings, such as low efficiency (power conversion efficiency, external quantum efficiency, etc.) and poor stability (against water, oxygen, UV light, etc.), limit their practical applications. Downsizing the materials into nanostructures and incorporating rare earth (RE) ions are effective means to improve their properties and broaden their applications. This review will systematically summarize the key points in the design, syntheses, properties improvements and application expansions of RE-containing (including both RE-based and RE-doped) halide and oxide perovskite nanomaterials. The critical factors of incorporating RE elements into different perovskite structures and the rational design of functional materials will be introduced/discussed in detail. The advantages and disadvantages of different synthesis methods for perovskite nanomaterials will be reviewed/discussed. This paper will also summarize some practical experiences on selecting suitable RE elements and designing multi-functional materials according to the mechanisms and principle of RE promoting the properties of perovskites. At the end of this review, we will provide an outlook on the opportunities and challenges of RE-containing perovskite nanomaterials in various fields.

1. Introduction

Perovskite nanomaterials (PNMs) is becoming a research hotspot and have been extensively studied for their variable formulae, flexible and structures, numerous unique properties and broad applications.[1-4] The earliest identified perovskite is $CaTiO_3$, and later the formula has been derived into a wealth of new forms, such as ABX_3, $A_3B_2X_9$, $A_2BB'X_6$, A_2BX_6, A_4BX_6, and so on, in which A and B are cations (A has a larger radius than B), and X is halide or oxide anion. Perovskites contain BX_6 octahedrons in their crystal structures while A atoms locate in the interstitial void of neighboring octahedrons.[5-8] The diverse compositions and structures endow perovskite materials with various properties and widely applications:[4, 5, 9, 10] luminescent perovskites have been used in the field of illumination, display, sensing and biological imaging, etc.;[11-14] some photoelectric perovskites have been applied in the aspects of photovoltaics, photo-catalysis, electro-catalysis, etc.;[15-19] electrical perovskites are used to prepare dielectric devices, ionic conductor, etc.;[20-22] magnetic perovskites are used in magnetic refrigeration, information storage, biomedical imaging and other fields.[23-25]

With the increasing attention on the nanotechnology, scientists have been trying to downscale the perovskite structures into the nano regime, so as to further boost their performances.[1, 26, 27] Compared with bulk counterpart, nanosized perovskites exhibit a series of advantages: for the fabrication of thin films and flexible devices, PNMs display a high processability;[28, 29] for catalysis, PNMs feature rich and modulatable facets and active sites;[30, 31] besides, benefiting from the small-size effect and quantum effect, PNMs are endowed with outstanding photo-electro-magnetic properties.[32-38] All these new characteristics help to enrich the performances of perovskites and broaden their applications.

However, pristine perovskites have some inherent drawbacks, such as poor stability (against water, oxygen, heat, light), and limited adjustability of optical, electrical and magnetic properties.[2, 10, 29, 39, 40] Scientists have been doping foreign metal ions into the PNMs to overcome these shortcomings.[27, 41, 42] Rare earth (RE) elements, known as 'the vitamin of modern industry', are extensively used as dopants to modulate the specific physical and chemical properties of different materials.[43] The RE elements, including 15 lanthanides (Ln: La, Ce, Pr, Nd, Pm, Sm, Eu, Gd, Tb, Dy, Ho, Er, Tm, Yb, Lu) and scandium (Sc) and yttrium (Y), have various multivalent ions: the RE^{3+} ions have the electron configurations of $[Xe]4f^{n-1}$ for Ln^{3+} (n=1–15), [Ar] for Sc^{3+} and [Kr] for Y^{3+}; the RE^{2+} (Sm^{2+}, Eu^{2+} and Yb^{2+}) and RE^{4+} (Ce^{4+}, Pr^{4+}, Nd^{4+}, Tb^{4+} and Dy^{4+}) ions have the electron configurations of $[Xe]4f^{n}$ and $[Xe]4f^{n-2}$, respectively.) The variable valence states and electronic structures endows RE ions with flexible redox properties, unique luminous and electromagnetic characteristics.[44] Therefore, REs have been widely incorporated into the perovskite nanostructures to improve their performances and broaden their applications.[45, 46] In addition, researchers also have been synthesized a series of RE-based perovskite functional materials.[47, 48] Both the RE-doped and RE-based PNMs exhibit satisfactory performances.[5, 49]

In view of the broad attention focused on RE-containing PNMs, this review will introduce their basic compositions, variable structures, preparation methods, properties and applications (Scheme 1). The rational design and controllable syntheses of RE-containing PNMs will be discussed in detail. Furthermore, the mechanisms of REs improving the performances of perovskites will be summarized. Also, the applications of PNMs in the fields of energy, environment, photo-electrics, and electromagnetics will be reviewed. This article will also discuss the possible solutions to the problems in the application by optimizing the compositions, structures and preparation methods. At the end of this review, the emerging opportunities and challenges for the development of RE-containing PNMs are provided.

2. Design RE-containing PNMs

In order to obtain multifunctional RE-containing PNMs with stable structure and excellent properties, their compositions and structures should be elaborately designed.[6, 7, 50, 51] Beyond the most typical metal oxide and halide compositions, many elements in the periodic table can serve as the component candidates, yet only a limited selection of them are able to construct stable perovskite structures. In addition, REs themselves can serve as the matrix element for stable perovskites. In particular, the stability of perovskite is dependent on the tolerance factor (*t*) and octahedral factor (μ),[52, 53] which strongly correlates to the difficulties of RE doping in the perovskites.[54] Furthermore, suitable chemical components can be selected and incorporated to construct functional perovskites according to the expected performances and applications.[55-57]

2.1 The diversity of perovskite crystal structures

In general, the ABX_3 perovskite usually display the six-coordinated B site with X by forming a octahedron structure, surrounded by A sites.[5] According to the arrangement of the octahedron and A site, perovskite can be divided into four types: zero-dimensional (0D) perovskites, one-dimensional (1D) perovskites, two-dimensional (2D) and three-dimensional (3D) perovskites (Fig. 1).[58] If the BX_6 octahedrons share X anions with adjacent ones in the three-dimensional directions, the octahedrons connect with each other, which corresponds to the 3D perovskite crystal.[59] In comparison, when the BX_6 is connected with the shared X anions only in two-dimensional plane, then forming 2D perovskite crystal are formed.[60] It is also noted when A sites are occupied by the groups than are too large, such as the long-chain alkyl amine cations, the typical lead halide perovskites would turn into the 2D Ruddlesden-Popper (RP) layered structure perovskites, which can be further classified by the layer number.[61] In a similar fashion, the 1D connection of BX_6 octahedron represent the 1D perovskite crystal.[62] In particular, if the BX_6 octahedron is separated by the excessive A atoms without any connections to each other, it is called the 0D perovskite crystal.[63] Owing to the varied crystal structures and compositions of perovskites, the doping of RE ions into the structures become much more flexible.[63-66] Therefore, the doping strategy of RE ions to perovskites opens new opportunities in designing the multi-functional RE-containing perovskite materials.

2.2 Tolerance factor and octahedral factor

Perovskite was first discovered as a common mineral with the chemical compositions of $CaTiO_3$, and later developed into a series of derivate with chemical formula of ABX_3. $A_3B_2X_9$, $A_2BB'X_6$, A_2BX_6, etc. (Fig. 2)[67-70] Perovskites can be divided into halides and oxides: for the halide perovskites, A is univalent cation (K^+, Na^+, Rb^+, Cs^+, R-NH_3^+, etc.), B is multivalent metal ion (Mg^{2+}, Zn^{2+}, $Pb^{2/4+}$, $Sn^{2/4+}$, Sb^{3+}, In^{3+}, Bi^{3+}, etc.), and X represents halide anion (F^-, Cl^-, Br^-, I^-); Oxide perovskites ($X = O^{2-}$) have the compositions of multi-valent metal cations (Ca^{2+}, Ti^{4+}, Fe^{3+}, Pb^{4+}, etc.), in which the cations with larger radius occupy the A sites while the smaller ions occupy site B, and X is O^{2-}.[5, 56, 71] In the ideal perovskite of ABX_3, the radii of all these cations and anions should meet the tolerance factor ($t = (R_A+R_X)/[\sqrt{2}(R_B+R_X)]$) and octahedral factor ($\mu = R_B/R_X$), and R_A, R_B, R_X refer to the ionic radii of A, B and X, respectively.[7, 52] The *t* value often varies from 0.81 to 1.11; otherwise, the cubic or cubic-like crystal structure would be distorted, and even destroyed.[4] A smaller *t* value would result in the lower-symmetrical tetragonal or orthorhombic structures. The *t* value of ideal cubic structure waves in the range from 0.89 to 1.0.[52] The value of μ ranges between 0.44 and 0.90, which determines the stability of the octahedral, and further affect the stability of the perovskite structure.[72] For the most well-known perovskite $CsPbBr_3$, the ionic radii of Cs^+, Pb^{2+} and Br^- are about 170 pm, 119 pm and 195 pm, respectively, which derive the value of *t* of 0.82, the μ value of 0.62.

$$t = \frac{[(1-m)R_A+mR_{\mathrm{A}'}]+[(1-p)R_X+pR_{\mathrm{X}'}]}{\sqrt{2}\{[(1-n)R_B+nR_{\mathrm{B}'}]+[(1-p)R_X+pR_{\mathrm{X}'}]\}} \qquad (1)$$

$$\mu = \frac{(1-n)R_B+nR_{\mathrm{B}'}}{(1-p)R_X+pR_{\mathrm{X}'}} \qquad (2)$$

$$\tau = \frac{R_X}{R_B} - n_A\left[n_A - \frac{R_A/R_B}{ln(R_A/R_B)}\right] \qquad (3)$$

$$t' = \frac{\sqrt{2}(R_A+R_X)}{R_B+R_{\mathrm{B}'}+h_X} \qquad (4)$$

In the polyatomic hybrid perovskite systems, such as $AB_{1-n}B'_nX_3$, $A_{1-m}A'_mBX_3$, $A_{1-m}A'_mB_{1-n}B'_n(X_{1-p}X'_p)_3$, and even other complex systems, the factors of *t* (Eq. (1)) and μ (Eq. (2)) are otherwise deduced, where R is the ionic radii for different ions.[6, 66, 73] While, as for the double perovskites of A_2BX_6, owing to the numerous B-site vacancies, *t* is not a proper index for evaluating the stability of its structure. So a new tolerance factor τ (Eq. (3)) is proposed ($\tau < 4.18$), where R is the ionic radii, and n_A is the oxides state of A ion. As τ decreases, the probability of being perovskite increases.[53, 69] The τ value is more suitable for evaluating the stability of double perovskites, according to the theoretical calculation and experimental verification.[74] In addition, another tolerance factor *t'* (Eq. (4)) for $A_2BB'X_6$ has been reported, where R is the ionic radii, h_X represents the effective height of X in the rigid cylinder.[51] Therefore, the possibility of forming double perovskites and its stability can be quantitatively described.

According to the tolerance factor and octahedral factor, we can select proper RE ions to replace the positions of A and B in perovskite structures, to further construct new functional perovskite materials. RE ions can replace the B site in the halide perovskites, and occupy the A site or B site in the oxide perovskites.[43, 75, 76] In addition, some articles reported the theoretical calculation results and experimental data to support the possibilities of incorporating RE elements into perovskite crystal structures.[77, 78] It is worth mentioning that Eu has been identified that acts the redox shuttle in the perovskite to selectively oxidize Pb^0 and reduce I^0 defects for the long-term stability of perovskites.[9] Based on the previous reports and theories, researchers can rationally design various RE-doped multifunctional perovskite materials.

2.3 Theoretical Investigation

Owing to the development of theoretical calculation and simulations, we are allowed to carry out theoretical investigations beyond the traditional experimental characterizations, which provide insightful information of the electronic behaviours and energetic behaviours for perovskite. This approach supplies the possible routes to design and synthesize RE-containing perovskite materials based on the mechanism studies. Guo and his co-workers declared that the A(B) vacancy can easily bind with the RE^{3+} when in the O-rich areas.[6, 54, 79] As for the halides and oxides perovskites, RE can be easily introduced into structures, for instance, in $CsPbBr_3$ perovskite, the ionic radius of divalent Pb^{2+} is about 119 pm, and the RE^{2+} (Eu^{2+}, Yb^{2+}, Sm^{2+}, etc.) has the radius between 102 pm and 117 pm;[43, 80] as for $Cs_2AgBiCl_6$ double perovskite, the radius of Bi^{3+} is 103 pm, which is very similar to the radius of RE^{3+} (Y^{3+}, La^{3+}, Nd^{3+}, etc.) (86–103 pm),[81, 82] indicating a lower barrier for RE doping in the halide perovskite materials. Pazoki and Kullgren further demonstrated the RE-doped iodide as the potential photo-absorbers for PV applications, which are ascribed to the dominant contribution to the valence band maximum by the localized f-electrons.[83]

For the oxides based perovskite, such as $CeAlO_3$, $LaMnO_3$ and $SmNiO_3$, which are very easy to incorporate other RE ions, because the chemical properties of different RE elements are extremely similar.[84-86] By using $CaTiO_3$ as an example, Lu et al demonstrate the RE ions doping trend based on systematic DFT calculations. For heavier RE ions, the substitution of Ca and Ti sites are favoured under p-type for trivalent state and n-type growth for divalent, respectively. Meanwhile, the Ca sites doping dominates the light RE ions.[87]

Theoretical calculations are also of great importance in revealing the electroactivity of RE-doped perovskite. For the high electroactivity of RE-doped perovskite, Kilner et al. reported the unique electronic configuration of RE, in which the partially occupied d-orbital of RE and the associated partial covalence instead of the complete ionization are responsible for the catalytic behaviours.[88] Furthermore, Shao and his co-workers demonstrate the A-site ionic electronegativity (AIE) as the indicator in perovskite to predict the HER performance. DFT studies demonstrate that optimal AIE value of ~2.33 indicates the optimal electronic states of active B-sites in perovskites due to the inductive effects and electron exchange interactions between A-sites and B sites.[89]

2.4 Evaluation of RE-incorporating

Many works have been reported the improved properties and performances of perovskite can be improved and promoted by the RE doping.[11, 90] It is well all known that Pb-halide-based perovskites have excellent optical and electrical properties, which are widely used in the field of perovskite solar cells (PSCs), and some of them have outstanding performances.[67] However, those pristine phases of Pb-based halides have various natural drawbacks, such as poor stability against heat, light, and humidity, etc.[29, 91] In order to overcome these shortcomings, the RE ion pair $Eu^{2/3+}$ was incorporated into the $CsPbI_3$ perovskite, where the redox characteristics of $Eu^{2/3+}$ can stabilize the structure.[9, 92] The $Eu^{2/3+}$: $CsPbI_3$ encapsulated solar cell not only exhibits high photoelectric conversion efficiency (PECE) but also has a durable service life. In addition, when serving as light-absorbing materials for solar cell, halide perovskites show an absorption ability of halide perovskites is relatively limited from ultraviolet to visible light,[59] which largely waste the solar light in the infrared region and limits the PECE of PSCs. In this regard, RE^{3+} (Yb^{3+}, Ce^{3+}) were doped into perovskites show the evidentially extended light absorption towards the near-infrared (NIR) region, and the prepared PSCs show high PECE.[90, 93]

Halides perovskites, such as $CsPbBr_3$ and $Cs_2AgBi_{1-n}Sb_nBr_6$ nanocrystals, have some excellent photoluminescence (PL) properties. However, because their emission wavelength can be regulated only in the visible light region, it is difficult for them to emit near-infrared light, and the emission peaks generally have broad full width at half maximum (FWHM) of emission peak, the PL decay time is very short.[42, 94, 95] Beyond this, the emission spectra of PNMs can be adjusted from ultraviolet, visible to near infrared region by doping the RE^{3+} (Tm^{3+}, Ce^{3+}, Tb^{3+}, Sm^{3+}, Eu^{3+}, Er^{3+}, Ho^{3+}, Dy^{3+} and Yb^{3+}). RE ions have special luminescence properties: the emission peaks of RE ions are very narrow, with the FWHM only a few nanometers; the luminescence decay time is relatively long, which can reach to several microseconds; the emission spectra cover a wide range from ultraviolet, visible to NIR.[44, 96] Some works have been reported on the RE-doped perovskites, in which the RE ions greatly broaden the spectral range of perovskite materials.[36, 97] Furthermore, the addition of RE ions can also improve the luminescence efficiency and the stability of PNMs.[11, 12, 98]

Compare with the halide perovskites, the oxide perovskite materials display various special functions by incorporating RE ions.[99-101] By doping luminescent RE ions into oxide perovskites, a series of optical materials are prepared, which can be used in lighting, display, detection, biological imaging and other fields.[102, 103] For example, $GdFeO_3$ perovskite oxides exhibit a high sensitive gas response to NO_x and a low detection level at 2 ppm, which show a high resistance variation to NO.[104] The perovskites containing magnetic RE ions also have been studied in the fields of biomedical imaging, magnetic devices.[25, 105-107] For example, Gd(Tb)FeO_3 has good magnetic properties, which shows great potential in biomedical field as the T_2 MRI contrast agents. In addition, the excellent dielectric properties are noted in some RE-based oxide perovskites, which are serving as dielectrics in various electric devices.[108]

Different from direct doping strategy, the RE-based oxide perovskites are important catalyst materials with high thermal and environmental stability.[5] The multivalent RE ions endow perovskite materials with excellent redox properties and further give the catalysts special catalytic activity, which is widely used in energy conversion, environmental purification chemical industry, and other fields.[18, 109-111] There are numerous works of RE-based oxide perovskite as catalysts in different catalysis processes. $LaNiO_3$ can act as efficient electro-catalyst for oxygen evolution reaction (OER) for new rechargeable zinc-air batteries.[112] $LaFeO_3$ has been reported as photo-catalyst for the degradation of organic dyes;[113] $La_{0.5}Ba_{0.5}MnO_3$ has high stability and catalytic activity for CO and CH_4 oxidation.[114] $La_{1-n}Ce_nMnO_3$ could catalyse NO reduction to NH_3 at low temperature.[115] $CeAlO_3$ can serve as catalyst, promoting glycerol steam hydrogenolysis and dehydrogenation-dehydration to produce hydrogen.[116] All in all, RE ions play an indispensable role in oxide perovskite catalysts, and the RE ions are remarkable candidate dopants and important components which can improve the catalytic activities.[3] Moreover, the RE based perovskites can be easily functionalized by the combination the unique perovskite structure and the specific RE ions.[117-119]

2.5 RE-containing PNMs

In view of both of the PNMs and RE ions have excellent properties, it is necessary to combine them systematically. The RE-containing PNMs possess special optics, magnetics, electronics and catalytic performances. These unique properties originate from the effectively shielded electrons in the 4*f* subshell are effectively shielded by the electrons in outer 5*s* and 5*p* subshells.[120] Therefore, by doping RE ions, adjusting the sizes and morphologies of PNMs can yield unprecedented and unexpected new multifunctional materials.[32, 121, 122]

Recently, there have various work about RE-containing PNMs been reported. In the photovoltaics, RE-doped perovskite nanofilms materials have been reported featuring high PEC and durable stability.[43, 123] As for LED lighting, RE-containing perovskite nanocrystals not only improve the luminescence efficiency, broaden the spectral range, but also have high stability.[4, 11, 12, 100, 103] And RE-containing PNMs exhibit good optical properties in the fields of non-linear optics and lasers.[1, 124] Besides, in electronics, RE-containing perovskite nanopowder materials can improve the dielectric properties of materials and expand the applications of materials in electronics.[2, 125] In the biomedical fields, RE-containing perovskite nanocrystals can be used as contrast agents for bioimaging.[44, 126] RE-based nanocatalysts have unique catalytic properties.[17, 127] In the field of analysis and detection, RE-containing perovskite materials have high sensitivities and fast responses to some metal ions, gases, temperature, X-ray, and so on.[14, 104, 128-132] Finally, with the above classical cases, we can design the RE-containing PNMs catering to the different requirements in practical applications.

3. Synthetic methods

The preparation process is of pivotal importance in studying the compositions, structures and performances of nanomaterials.[50] Developing highly efficient and controllable syntheses strategies of RE-containing PNMs are very important to design and modulate the new functional materials, and is also essential for understanding the intrinsic mechanisms of the enhanced performances of PL, catalysis, photovoltaic effect and ferroelectric effect.[121, 133-135] Presently, the major challenge of RE-containing PNMs syntheses is to achieve flexible control in replacing the position of cations (B or A) in the perovskites structure with RE ions.[34, 37, 118, 136]

Over the past years, various synthesis methods have been reported on preparing RE-containing PNMs (Fig. 3). These methods can be divided mainly into three categories: wet chemical synthesis methods, high-temperature synthesis processes and other synthesis approaches.[72, 101, 137, 138] These advanced methods are feasible for the preparation of RE-containing PNMs for applications in different fields. Although there are many ways to synthesize nanomaterials, all of these processes involve two core steps, nucleation and growth.[139] The raw materials release abounding free atoms or ions under heating liquifation, solution ionization and high voltage plasma. These free atoms or ions accumulate into small aggregates, namely, crystal nuclei, to complete the nucleation step.[82, 140, 141] Then continuously released free atoms or ions bond or assemble on the surface of the nucleus, which corresponds to the growth step of nanocrystals.[137] The nanomaterials are obtained by stopping the supply of free ions or atoms via cooling or adding anti-solvents.[11, 36] Different preparation methods of materials have their special advantages and disadvantages, and thus it is very important to select the suitable preparation methods according to the characteristics of raw materials and target compounds.

3.1 Wet chemical (WC) synthetic methods

Wet chemicals synthesis methods have been widely used in the preparation of nanomaterials, including sol-gel (SG) method, thermal decomposition (TD) approach, hot injection (HI) method, solvothermal (ST) synthesis, co- precipitation (CP) and so on.[36, [142-145] Among these methods, the HI, RP and TD approaches have been demonstrated to be the most effective method to synthesize RE-containing halide PNMs, whereas SG and ST are widely used to synthesize oxide PNMs.

3.1.1 Hot injection (HI) and thermal decomposition (TD) method

As for the preparation of PNMs, HI and TD have the advantages of simple operation and good repeatability. Meanwhile, the materials prepared by HI and TD method have uniform sizes, controllable morphologies and excellent dispersibility (Fig. 4),[11, 137] which is essential requirements for achieving good performances. Typically, HI and TD methods require solvents or surfactants with high boiling points, such as 1-octadecene (ODE), oleic acid (OA) and oleylamine (OM), and the reaction are carried out in the flask protected by inert gases.[141]

HI method is suitable for the preparation of halide RE-doped PNMs: certain amount of preheated (100~120 °C) precursor (Cs-oleate) solution is rapidly injected into another higher-temperature (150 ~180 °C) precursor ($REX_{2/3}$, PbX_2, X=Cl, Br and I) solution, after a period of reaction, the desired nanomaterials were obtained by rapid cooling; the desired nanomaterials can be obtained by washing the products with nonpolar solvents (toluene or hexane).[36, 41, 98] In addition to the injection of Cs-oleate solution, injecting halogen sources (trimethyl chlorosilane, trimethyl bromosilane, acyl chloride, etc.) is also available for HI.[146, 147] In this case, metal (Pb^{2+}, Cs^{+}) acetates are used as metal sources. Organic halogen reagents decompose at high temperature to form free halide ions, which combine with metal ions to form halide perovskite nanocrystals.

Since most halide perovskite materials are ionic compounds, they have relatively poor stability in polar solvents, which easily change their morphologies and lead to degradation.[146, 148] In addition, the nucleation and growth processes of halide PNMs are very fast and sensitive to the reaction system such as the reaction temperature, polarity of the solvent and the ratio of the different surfactants. These factors show great influence on the size and the uniformity.[147] Therefore, all the solvents used in the HI injection reaction should be anhydrous and anaerobic, and other precursor reagents used should be of high-purity. Besides, the solvents used in the post-treatment process must also be purified, for example, the solvents cyclohexane, toluene, and hexane should be purified by distillation.

The TD method usually is applied to prepare some fluoride perovskites.[149],[150] Metal (Zn^{2+}, Mn^{2+}, Na^{+}) trifluoroacetate precursors are added to the mixture solution of OA, OM and ODE, and some small molecular impurities (O_2, H_2O, etc.) should be removed by heating under vacuum. The decomposition products of trifluoroacetates formed fluoride perovskite nanocrystals at higher temperatures.[151]

3.1.2 Co-precipitation (CP) method

The co-precipitation method is another common method to fabricate the PNMs (Fig. 5).[148, 152] The general process is that, dissolving precursors in benign solvents, the precipitation of precursor ions forming NCs by adding precipitators or changing the solubility of the reaction system. However, the morphologies of certain halides PNMs (i.e. $CsPbBr(Cl)_3$ and $Cs_3Bi_2Br_9$) are very difficult to control by using the CP method.[148, 153, 154] This is due to small amounts of polar solvents can promote the precursors to form bulk crystal instead of nanosized perovskites. Such nanomaterials are unstable in the dispersants in the long term, and they can easily to grow larger, aggregate or even be destroyed during the storage.[155] Once the morphologies of NCs change, their properties decline dramatically, as well as their performances, will degrade irreversibly. To suppress such morphology change issue, surfactants can be added to stabilize nanocrystals.[153] However, additional surfactants may also hamper the properties of the materials. Yet for the most oxides and fluorides, they have a high stability because of O^{2-} and F^{-} have large electronegativity, and only acidic conditions can destroy their structures.[140, 145, 152, 156]

3.1.3 sol-gel synthesis method

The sol-gel method is widely used to prepare oxide perovskite materials, and SG is not suitable for the preparation of halide perovskites. The raw materials ($Ln(NO_3)_3$, $TM(NO_3)_x$, citric acid, etc.) are dissolved and mixed in water, hydrolyse and condense to form a stable sol system, and then nanomaterials are formed after drying and sintering.[157] The morphologies of nanomaterials prepared by this method lacks uniformity, controllability and the dispersibility (Fig. 6). However, this method has its unique advantages; it can be used to prepare oxide perovskites with high phase-formation temperature.[158, 159] There are many oxide PNMs ($LaTiO_3$, $LaFeO_3$, Yb/Er: La_2CoMnO_6, etc.) synthesized by the SG method, and these functional materials show excellent performance.[157, 160, 161]

3.1.4 Solvothermal (ST) method

Solvothermal is one of the most commonly used approaches for preparing nanomaterials, which can be used to synthesize various perovskite materials, especially for nanostructured Pb-based, fluoride and oxide perovskites.[1, 118, 162] However, ST is not suitable for the syntheses of nanosized halide double perovskites.[163, 164], ST method is based on the hydrothermal method, which is carried out in a closed system such as autoclaves, the organic compounds as the solvents at a certain temperature, and autogenous pressures of the reaction solution provide dynamic conditions for the materials generating. In order to obtain desired nanomaterials with controllable morphologies and uniform sizes, it is often necessary to use some surfactants in the reaction. $CsPbX_3$ perovskite NCs was synthesized by ST method, certain amounts of the precursor solutions (Cs-oleate in OA/ODE, PbX_2 in OA/ODE/OM) were added into autoclave, and heated to 200 °C for 50 mins to form the nanomaterials.[164] For the Eu-doped $KZnF_3$ was synthesized by using NH_4F, metal (Eu^{3+}, Zn^{2+}) nitrates are the raw materials, and OA, n-butyl alcohol act as the solvents. The nanoparticles were obtained after the reaction kept 120 °C for 48 h.[165] Similarly, La-doped $SrTiO_3$ was synthesized by using metal (La^{3+}, Sr^{2+}) nitrates and tetrabutyltitanate in the solution of OA and ethanol, and heated in the autoclave at 180 °C for 12 h.[166] For the post-treatment process of ST reaction, polar or non-polar solvents (ethanol or hexane) can be used for washing oxides and fluorides, whereas the chlorides and bromides must be washed by non-polar solvents (hexane or toluene).

3.2 High-temperature (HT) method

HT method was developed and widely used to synthesize some inorganic materials with higher phase forming temperature, which has the merits of easy operation, and mass-produced processes. In addition, the materials synthesized by this method have high crystallinity, less defects, and high stability. Thus, some oxides perovskite materials with complex compositions can be easily synthesized by HT method. The HT method can be divided into solid state synthesis (SS) and molten salt reaction (MS). For example, $La_{1-x}Sm_xFeO_3$ perovskite was synthesized by SS method, for which La_2O_3, Sm_2O_3 and Fe_2O_3 were milled and annealed in air at 1473 K for 40 h to form micro-scale samples.[167], And Eu/Pr-doped $CaTiO_3$ can be synthesized by MS method, the raw materials were mixed and ground, then put into muffle furnace annealed at 820 °C for 3.5 h, and the micro-scale spheres were obtained by washing the products with distilled water and ethanol.[131] These two approaches also have common shortcomings: without ligand or organic molecule protection on the surface of the particles, the morphologies and the sizes of desired materials are difficult to control precisely.[24]

3.3 Others synthetic methods

In addition to the above-mentioned methods, there are other special synthetic processes, such as spin coating technique (SCT), pulsed laser deposition (PLD), electrospinning technique (EST), and chemical vapour deposition (CVD) approaches, which have been widely used for the preparation of the high quality thin films. And the as-prepared thin film materials possess the advantages of a few atoms thickness, uniform surface, high crystallinity and less defects.

3.3.1 PLD and CVD methods

RE perovskite film is an important research topic in the field of physics and materials. Thus, it is of great significance to prepare high-quality thin film materials to apply in the fields of microelectronics, magnetics and optoelectronics. PLD is known can deposit material layer by layer on the base surface, which is a common methods for preparing thin films. PLD is known as pulsed laser ablation, in which the active ions or atoms bombarded by laser radiation are deposited on different substrates to obtain thin films. This method is widely used to prepare RE-containing perovskite thin films such as $La_{0.8}Sr_{0.2}CoO_3$ film, $YBaCo_2O_6$ film, Sm-doped $NdNiO_3$ film, etc.[48, 168-171] These materials show superior performances in catalysis, electronics, magnetics, photovoltaics and other fields. Moreover, *h*-$TmFeO_3$ film has been successfully synthesized by PLD method, which has large ferroelectric polarization (4.7-8.5 $\mu C/cm^2$) to further inhibit the rapid recombination of the photo-induced electron-hole pairs.[172] Such a material obtained a better power conversion efficiency (PCE) than of the typical $BiFeO_3$. Manuel Bibes and his co-workers prepared the $NdNiO_3$ film by PLD method (Fig. 7).[139] The author observed a strong resistance contrast among the metallic and the insulating regions, and between the sample and the tip has a Schottky barriers. CVD is another effective deposition method to produce high quality, high-performance based on the vacuum deposition method. Huang et. al. synthesis of $CsPbBr_xI_{3-x}$ nanowires by CVD methods.[173] The as-prepared $CsPbBr_xI_{3-x}$ nanowires have uniform size and good crystallinity.

3.3.2 Spin-coating technique

Among various methods, SCT is a relatively simple approach to nanomaterials preparation. This method has the advantages of energy saving, low pollution, controllable thickness, massive production and high efficiencies. By adjusting the rotational speed and the viscosity of the precursor solution, the thickness of the film can be modulated easily. In order to obtain a high-quality film with uniform and smooth surface, the used salts or nanosized raw materials should be dissolved or dispersed in the colloid solution sufficiently. The last important factor for the film preparation is the heating temperature and heating rate, which determine the solvent volatilization speed, the nucleation and growth of the film on the substrate. Wang et. al. prepared Eu^{2+}/Eu^{3+} incorporating $CsPbI_3$ film by SCT, and the synthesized films are highly uniform, which have good compactness and mechanical properties.[9] In addition, Eu^{2+} was successfully introduced into the crystal structure of $CsPbI_2Br$ by SCT.[43] The grains of the films were refined and uniform by adding Eu^{2+}, and the efficiency and the stability of the corresponding devices were improved. This method has been widely used in the preparation of solar cell films and other films.

3.3.3 Electrospinning technique

Electrospinning technology (EST) is often used to prepare fibrous or spherical RE-containing PNMs. The precursor (metal salt, polymer) solution is added to the syringe. Under the high voltage electrostatic field, the polymer carries metal salt to form a microjet and deposits on the substrate. The organic matter is removed by sintering and obtains desirable nanomaterials.[174] As shown in Fig. 8, $La_{0.6}Sr_{0.4}Co_{0.8}Mn_{0.2}O_3$ nanofibers were prepared by EST.[175] The fibers prepared by this method have the uniform diameter and good dispersion. In recent years, this method is also extended to prepare the nanosized RE-containing oxide perovskite catalysts such as the electrode materials $La_{0.6}Sr_{0.4}Co_{0.2}Fe_{0.8}O_{3-\delta}/CeO_2$ nanofibers with heterojunction structure, which exhibits high activity and stability in solid oxide fuel cells.[176]

4. Properties and applications

4.1 Photovoltaic properties and applications

Solar cells, as a device of directly converting abundant solar energy into electrical energy, have been regarded as one of the most promising solutions to ease the global energy crisis. Since the utilization of $CH_3NH_3PbI_3$ perovskite in solar cells by Kojima in the year of 2009, the PECE of PSCs has been rapidly raised to 23.7%.[39, 91] Such a high PECE boosts perovskite-based solar cells (PSCs) closer to practical applications, with performances similar to those of commercial single crystal silicon-based solar cells.[18, 67, 74] However, the poor stability of halide perovskite materials against high temperature, humidity and oxidizing substances still severely limited their service life and industrial applications.[177] Moreover, the PECE of perovskite-based solar cells is still far from their theoretical maximum value.[91] To mitigate this problem, incorporating RE elements into halide perovskites has become an effective approach.[80, 138, 178]

RE elements, with various electronic configurations sizes, have been reported as key factors in enhancing the stability, broadening the absorption range, and regulating the band gaps of perovskite materials, therefore further improving the PECE and durability of the PSCs.[9, 172] All these improvements are essential for the future industrialization and application of PSCs.[90] There have been a significant amount of articles about RE-containing PSCs. The performances of RE-containing PSCs are summarized in Table 1, including the open-circuit voltage (V_{oc}), the short-circuit current density (J_{sc}), the fill factor (FF), and the PECE. In the following sections, current RE-containing PSCs are reviewed according to the functions of RE elements.

4.1.1 Stability enhancement

The superior performances of Pb-based PSCs are still leading the international research hotspots. However, Pb-based perovskites suffer from easy decomposition under humid or redox environments, resulting in significant degradation of performance.[126, 179-181] The incorporation of RE elements can stabilize the desired phase and increase the redox, humidity, and chemical resistance of halide perovskites.[9, 80] Other reports also highlight that incorporating RE ions into perovskite structures can be a promising method to enhance the performance of the lead-based PSCs.[43]

Table 1 The RE-doped perovskite material for Solar cells

Perovskites	RE	Band gap (eV)	PECE (%)	J_{SC} (mA/cm^2)	V_{OC} (V)	FF (%)	Ref.
$MAPbI_3$	Eu	1.55	21.52	23.5	1.1438	73.2	9
$CsPbI_2Br$	Eu	-	13.71	14.63	1.22	76.6	43
$MAPbI_3$	Eu	-	16.7	21.50	1.02	76.3	80
$CsPbCl_{1.5}Br_{1.5}$	Yb,Ce	-	21.5	39.8	0.65	-	90
$BaSnO_3$	Er/Yb	3.64	4.2	9.69	0.63	69	101
$CsPbBr_3$	La, Ce, Nd, Sm, Eu, Gd, Tb, Ho, Er, Er, Yb, and Lu	-	10.14	7.48	1.598	85.1	123
$CsPbI_3$	Eu	-	6.8	11.1	0.898	68	178
$MAPbI_3$	Nd		21.15	24.33	1.04	83.6	182
$MAPbI_3/TiO_2$	Sm	1.55	14.10	18.11	1.032	68.3	183
$MAPbI_3$	CeO_2		19.52	23.64	1.09	78.67	184
Glass-ceramic	Sm/Ce	-	7.84	17.85	0.822	83.44	185

For example, Duan et.al added RE^{3+} (RE = La, Ce, Nd, Sm, Eu, Gd, Tb, Ho, Er, Yb, and Lu) into $CsPbBr_3$ films for PSCs via a multistep solution processable technique.[123] The grain sizes of the films increased with the RE^{3+} concentration, which minimizes the grain boundaries. Meanwhile, the film becomes more and more compact with the decreasing of the atomic number of RE^{3+}. With the RE-doping, the carrier migration time is further prolonged, and the recombination of charges and holes on the surface of perovskite film is significantly suppressed. Without metal electrodes and hole transport layer consisted in the solar cells, the PECE of 10.14% is remarkably high, and the open-circuit voltage is also as high as 1.59 V. The batteries show high stability, with no obvious change in the PECE at 80% relative humidity for 110 days. Moreover, the cells still maintain high efficiency after working at 80 ºC for 60 days. As Fig. 9 shows, the photovoltaic performances of the PSCs have been significantly improved by adding RE. In addition, the stabilities of the PSCs are also improved.

In another report, Wang et al. prepared the Nd^{3+}-doped $MAPbI_3$ planar heterojunction films for PSCs. The Nd^{3+} incorporation improved the quality of the films, reduced the trap-states, inhibited the photocurrent hysteresis, prolonged the charge carrier lifetimes, and further improved the charge carrier mobilities.[182] Therefore, the devices reaches a high PECE of 21.15%, and the author also demonstrates a new strategy to enhance the photoelectric performance of PSCs.

Owning to the high PECE, the PSCs containing PbI_2 as the starting material has been extensively studied. However, the defects of Pb^0 and I^0 always exist. These defects greatly reduce the PECE and shorten the device service lifetime. In the past few years, few efforts have been made to successfully eliminate these defects simultaneously. Wang et al. introduced $Eu^{3+/2+}$ ions into the $CsPbI_3$ perovskite, in which the Pb^0 can be oxidized by Eu^{3+} ions and the I^0 can be reduced by Eu^{2+} ions (Fig. 10).[9] This reversible redox cycle ingeniously eliminate both Pb^0 and I^0 defects in the devices. As a result, the efficiency of the device is improved greatly (PECE: 21.52%, certified 20.52%), and the lifetime of the device is also prolonged. This redox shuffle strategy for eliminating defects provides a reference for stabilizing other perovskite materials.

There are two other reports on the incorporation of Eu^{2+} in PSCs. The doping of Eu^{2+} ions into the organic-inorganic $MAPbI_3$ perovskite enhances both stability and PECE of the solar cells.[80] It is also shown that EuI_2 can stabilize the metastable phase of $CsPbI_2Br$.[43] The corresponding devices exhibit a stable PECE of 13.34%. The electroluminescence test shows that the introduction of Eu^{2+} reduces the non-radiative recombination, and enlarge the open-circuit voltage to 1.27 V. In addition, the initial efficiency of the device can retain at 93% for 370 hours under 100 mW/cm^2 light illumination (Fig. 11).

4.1.2 Absorption range expansion

The natural sunlight covers a broad frequency range from the ultraviolet to the infrared region. However, most perovskite materials only absorb the ultraviolet and visible light, greatly limiting the utilization efficiency of solar energy. The unique electronic structure of RE ions opens the opportunities to extend the absorption range to infrared light for the perovskites. As a result, the RE-doped PSCs are capable of absorbing the light covering from ultraviolet to infrared regions, which further improves the PECE.

It is reported that when the Yb^{3+}/Ce^{3+} co-doped perovskite is used as the photoabsorption layer, the efficiency of the devices is enhanced from 18.1% to 21.5%.[90] In addition, $LaGaO_3$: Cr^{3+}, RE^{3+} (RE = Yb, Nd, Er) co-doped perovskite can absorb the NIR light and then transfer the energy to C-Si-based solar cells.[186] The energy transfer processes between RE ions and devices were studied, and the energy transfer efficiency was as high as 77%, effectively improving the PECE of the solar cells.

4.1.3 Band gap modulation

PSCs consist of electrodes, perovskite layer, hole and electron transport layer. Under the illumination, the holes and carriers are effectively separated and transferred from perovskites to electrodes. Such transfer requires the appropriate energy match between perovskites and transport layers. As a result, the large band gap limits the fast and efficient transportation of charge carriers, and then directly affects the efficiency of PSCs. By the introduction of RE elements, the band gaps and electronic structures can be used to modulate for boosting the photocurrent or carrier migration rate and the PECE.

The substitution of about 10% of Ba^{2+} lattice site by Yb^{3+}/Er^{3+} reducing the band gap change of $BaSnO_3$ NCs from 3.64 eV to 3.68 eV and increasing the electrical conductivity.[101] Moreover, the Yb^{3+}/Er^{3+}-doped $BaSnO_3$ utilize the full region of the sunlight, yielding a PECE of 4.2%. Compared with the undoped $BaSnO_3$ NCs (PECE: 3%), the PECE is increased by 40%. As shown in Fig. 12, with different Yb^{3+} and Er^{3+} substitution levels, both absorption and emission spectra shifts, implying a successful modulation of the band gap, leading to the improved J_{sc} and V_{oc}.

ZnO/CeO_x is an electron transport material (ETM) in PSCs (Fig. 13).[184] The incorporation of CeO_x regulates the unmatched energy levels and protects perovskite materials against UV light, high temperature and humidity. As a result, the PECE of PSCs increases from 16% (ZnO) to 19.5% (ZnO + 3% CeO_x), and the service time of the cell is also prolonged. All reports reviewed in this section show that RE elements play an important role in enhancing the photovoltaic performance regarding the flexible modulation in different aspects, which are also a crucial contribution to the photovoltaic industry.

4.2 Dielectric properties and applications

Perovskites are very good dielectric materials. Due to their high dielectric constant (ε_r), processability and stability, therefore, they are widely used in electric vehicles,[187] pulse weapon systems, energy storage[188], power electronics, etc.[189] Owning to the unique electronic structures and intrinsic elemental characteristics of RE elements, doping RE into the perovskites structure may significantly improve the dielectric performances.[190] In the future, the novel perovskite possess the great potential in applications of mobile communications, radio, television, and microwave technology, which requires new dielectric materials with low permittivity and loss. This section summarizes the recent progress of RE-containing PNMs as piezoelectric, pyroelectric, and ferroelectric materials. [119]

4.2.1 Piezoelectric materials

Recent studies have illustrated that RE doping improves the dielectric properties of PNMs,[191] providing a promising approach to access new piezoelectric materials. RE-doping can enhance the heterogeneity of perovskite structures. The increasing atomic diffusion rate promotes the densification of perovskite ceramics, reduces the sintering temperature, and simultaneously enables the applications of a higher polarization electric field.

Chen et. al. demonstrated that nanoparticles have more advantages than microparticles in improving electrical performance.[192] Fig. 14A showed the TEM images of well dispersed CeO_2 nanoparticles calcined at 800 °C, with an average diameter of 20 nm. BCTS ($Ba_{0.96}Ca_{0.04}Ti_{0.90}Sn_{0.10}O_3$)-nano CeO_2 (0.03 mol%) has better piezoelectric performances than other ceramics, and its SEM image (Fig. 14B) presents the dense microstructure of BCTS ceramics with the inclusion of nano CeO_2. The nano CeO_2 contributes to the improvement of piezoelectric properties (Fig. 14D) because of the morphotropic phase boundary (MPB) effect, which makes the domain a greater space in the rotational motion. Moreover, the improvement of dielectric properties of the ceramics is ascribed to the weakening of strain potential energy (Fig. 14C). Therefore, the inclusion of nano CeO_2 elevates the piezoelectric properties of BCTS ceramics (Fig. 14E).

In addition, as Fig. 14F-I shows, Chen and co-workers further demonstrated that the piezoelectric properties of BCTS-Y ($Ba_{0.90}Ca_{0.10}Ti_{0.9}Sn_{0.1}O_3$-$xY_2O_3$) ceramics could be improved by incorporating Y_2O_3.[193] TEM and SEM images showed that BCTS-Y ceramics have uniform and well-distributed microstructure, with the maximum value of d_{33} (596 pC/N) and K_p (0.571) obtained when 1% of nanoY_2O_3 is incorporated, and this material has higher d_{33} and K_p than those of the micro-Y_2O_3 incorporated samples reported in literature.[194] Hence, the incorporation of nanoscale RE-containing compounds is more effective than the micron-level RE-containing compounds for the piezoelectricity of perovskite materials.

Lead zirconate titanate [$Pb(Zr_xTi_{1-x})O_3$, PZT], a representative material simultaneously possessing outstanding dielectric, piezoelectric, pyroelectric, ferroelectric properties, has already been used in high-performance electronic devices.[37] However, the Pb-containing materials are harmful to the environment and our health. Currently, some lead-free perovskites have been extensively investigated for environmentally friendly piezoelectric systems.[125, 195, 196] On this foundation, developing high performance (low cost) lead-free piezoelectric RE-containing perovskites are of critical significance. Especially, these materials with remarkable performances have potential applications in the field of industrial ultrasonic testing, transducer, medical imaging and other fields.[197, 198]

4.2.2 Pyroelectric materials

RE-containing PNMs are capable of exhibiting outstanding pyroelectric properties. When pyroelectric effects are presented, the electricity is generated under the thermal stimulation, which provide an important way for energy conversion, and which is also useful for temperature sensing. Pyroelectric effect is associated with the electrically charged species of the crystal structure along the direction of charge polarization displacement.[199] This is usually caused by the asymmetry positive and negative charge centres, which constitutes the ferroelectric dipoles and shows the pyroelectric effect.[200]

A good thermoelectric material should have a large Seebeck coefficient, good conductivity and a low thermal conductivity coefficient.[201] Kaya et. al. prepared perovskite based $LaNiO_3$-La_2CuO_4 layered heterojunction materials on the substrates of $LaSrAlO_4$ by atomic layer-by-layer oxide molecular beam epitaxy technique.[202] The electrical conductivity decreases while the Seebeck coefficient increases with the reduced thickness of the heterojunction layers. HAADF-STEM showed that $La_2(CuCo)O_4$ solid solution was formed in the heterojunction with the thickness of the layer decreases (Fig. 16).

The thermopower and barrier potential of the material increase with a small amount of La^{3+} doping into $SrTiO_3$ perovskites with a particle size of 20 nanometers. The results show that RE doping can modify the grain boundary and further adjusted thermoelectric properties of materials.[203] Gd and W were introduced into $CaMnO_3$ to form double substituted $Ca_{1-x}Gd_xMn_{1-x}W_xO_{3-\delta}$. The thermoelectric properties were tested from 25 °C to 700 °C. With the amount of incorporated Gd and W increasing, the electrical conductivity of the sample improved and the thermopower reduced. When x=0.01, the material exhibits a thermoelectric figure of merit of 0.12 at 700 °C.[204] In addition, Kinemuchi, Y et.al. also demonstrated that doping of RE can improve the Seebeck coefficient of Y-doped $SrTiO_3$, and promote their pyroelectric performances.[205]

4.2.3 Ferroelectric materials

With the development of nanotechnology, some RE-containing perovskites are widely investigated as ferroelectric materials for sensors and other devices due to their outstanding dielectric and ferroelectric properties.[206] Incorporating RE elements into the lattice structure of perovskites decreases of the crystal size and distortion of lattice, which optimizes the ferroelectric performance of the materials.

Liu et.al demonstrated that when La^{3+} or Nd^{3+} ions are doped in the PZT lattice, they act as donors, effectively reducing the movement of defective charges including free electrons and oxygen vacancies. Meanwhile, the appearance of the morphotropic phase boundary (MPB) greatly improves the holistic electrical properties of films. The substitution of RE-elements at the A-site also eliminates oxygen vacancies. All above interpretation is shown in Fig. 15A-C.[37] In addition, Guo and co-workers studied Nd^{3+}-doped PZT films prepared by different deposition sequences and revealed that the BNF/PZT bilayer had better electrical properties than the corresponding PZT/BNF film, which is shown in Fig. 15D-F. Moreover, the P-E curve of pure PZT film was presented the upper inset in (F) and the lower inset is the DC leakage characteristics of the laminar film, implied that BNF/PZT bilayer composite films possess better ferroelectricity than those of BNF/ PZT.[199] A new idea for the design of multi-layer structures is therefore provided in terms of enhancing the ferroelectricity of RE-containing PNMs. Other examples of the dielectric properties of RE-containing PNMs are shown in Table 2.

Table 2 RE-containing perovskite nanomaterials for electrical properties

Perovskites	**RE^{3+}**	**Methods**	**Morphology**	**Performance**	**Application**	**Ref.**
$PbZr_{0.52}Ti_{0.48}O_3$	La/Nd	SG	NFs	RT, 100 Hz, ε_r = 1053.36; tanδ = 0.13; LC = $8.3*10^{-9}$ A/cm^2; d_{33} = 36.4 pC/N; P_r = 64.32 μC/cm^2; E_c = 57.40 kV/cm;		[37]
$Ba_{0.96}Ca_{0.04}Ti_{0.90}Sn_{0.10}O_3$	Ce	HT	NPTs	RT, 1 kHz, ε_r = 32945.8; d_{33} = 512 pC/N; k_p = 0.415; P_r = 14 μC/cm^2; γ = 1.44;		[192]
$Ba_{0.9}Ca_{0.1}Ti_{0.9}Sn_{0.1}O_3$	Y	HT	NPTs	d_{33} = 596 pC/N; k_p = 0.571;		[193]
La-Pb($Ni_{1/3}Sb_{2/3}$)-$PbZrTiO_3$	La	CP	NCs	d_{33} = 449 pC/N; T_c = 286 °C;	power harvesting	[207]
$Pb_{0.92}La_{0.08}Zr_{0.6}Ti_{0.4}O_3$	La	MBM	NPDs	RT, 1 kHz, ε_r = 2293; tanδ = 1.98; P_r = 30.7 μC/cm^2; E_c = 9.4 kV/cm; T_c = 190 °C; γ = 1.98;	sensors, actuators, transducers	[208]
$La_{1-x}Dy_xFe_{1-y}Mn_yO_3$	La, Dy	ME	NPTs	RT, 6 kHz, ε_r = 1340;	recording media	[209]
$BaTiO_3$	Y	SG	NPTs	RT,10 kHz, ε_r = 2069; tanδ = 0.05; T_c = 125 °C; γ = 1.0;		[142]
$SrTiO_3$	La,Ce,Nd,Sm,Gd,Tb,Y	ST	NCBs	RT, 100 Hz, ε_r = 1800; d_{33} = 380 pm/V; k_p = 0.45;		[205]
$La_{1-x}Na_xFe_{1-y}Mn_yO_3$	La	PR	NCs	RT, 1 kHz, ε_r = 1256; tanδ = 1.01;	capacitors, resonators and memories	[206]
$Bi_{1-x}Nd_xFe_{1-y}Co_yO_3$	Nd	SG	NPTs	RT, 100 Hz, ε_r = 1050; P_r = 26 μC/cm^2; E_c = 5.6 kV/cm;	intelligent devices	[210]
$YCrO_3$	Y	PR	NCs	T_c = 137 °C;		[211]
$BiFeO_3$	La/Nd	SG	NFs	RT, 100 Hz, ε_r = 195; tanδ = 0.191; P_r = 61.21 μC/cm^2; E_c = 44.86 kV/cm;	devices design	[135]
$Bi_{0.9}Nd_{0.1}FeO_3$ - $PbZr_{0.52}Ti_{0.48}O_3$	Nd	SG	NFs	LC = $4*10^{-8}$ A/cm^2; P_r = 11.39 μC/cm^2; E_c = 87.16 kV/cm;	device design	[199]
$PbZrO_3$	Dy	ME	NCs	RT, 1 GHz, ε_r = 16.02; tanδ = 0.275;	high frequency memory devices	[38]
$La_{1-x}Sr_xCo_{1-y}Fe_yO_3$	La	ME	NCs	RT, 15 MHz, ε_r = 103.35; tanδ = 0.57;	microwave devices	[212]
$CoFeO_3$	Nd	SG	NCs	RT, 100 Hz, ε_r = 31.08; tanδ = 0.16;	microwave devices	[213]
$La_xSr_{1-x}CoO_3$	La	SG	NPTs	RT, 100 Hz, ε_r = 16;	sensing, memories	[214]
$LaFeO_3$	Eu	ME	NPTs	RT, 30 MHz, ε_r = 14.18; tanδ = 0.52;	frequency devices.	[191]
$MnFeO_3$	Gd	SG	NCs	RT, 100 Hz, ε_r = 5.53; tanδ = 0.129;	microwave devices	[215]
$PbZr_{1-x}Ti_xO_3$	La	SC	NFs	P_r = 10.14 μC/cm^2; E_c = 42 kV/cm;		[216]
$CrFeO_3$	Gd, Er	CCB	NPTs	P_r = 1.94 μC/cm^2; E_c = 214.8 kV/cm;	data storage and camera flashe	[217]
$La_{0.05}Li_{0.85}NbO_3$	La	HT	NCs	P_r = 0.15 μC/cm^2; E_c = 1.31 kV/cm;		[218]
$PbZr_{0.52}Ti_{0.48}O_3$	La/Nd	SG	NFs	RT, 100 Hz, ε_r = 1053.36; tanδ = 0.13; LC = $8.3*10^{-9}$ A/cm^2; d_{33} = 36.4 pC/N; P_r = 64.32 μC/cm^2; E_c = 57.40 kV/cm;		[37]
$Ba_{0.96}Ca_{0.04}Ti_{0.90}Sn_{0.10}O_3$	Ce	HT	NPTs	RT, 1 kHz, ε_r = 32945.8; d_{33} = 512 pC/N; k_p = 0.415; P_r = 14 μC/cm^2; γ = 1.44;		[192]
$Ba_{0.9}Ca_{0.1}Ti_{0.9}Sn_{0.1}O_3$	Y	HT	NPTs	d_{33} = 596 pC/N; k_p = 0.571;		[193]
La-Pb($Ni_{1/3}Sb_{2/3}$)-$PbZrTiO_3$	La	CP	NCs	d_{33} = 449 pC/N; T_c = 286 °C;	power harvesting	[207]
$Pb_{0.92}La_{0.08}Zr_{0.6}Ti_{0.4}O_3$	La	MBM	NPDs	RT, 1 kHz, ε_r = 2293; tanδ = 1.98; P_r = 30.7 μC/cm^2; E_c = 9.4 kV/cm; T_c = 190 °C; γ = 1.98;	sensors, actuators, trans-ducers	[208]

Note: RT, Room temperature; SG, sol-gel method; HT, high temperature method; ST, Solvothermal method; CP, columbite precursor method; MBM, mechanochemical ball milling; PR, Pechini method; CCB, citrate auto combustion method; ME, micro-emulsion route; NCs, nanocrystals; NPTs, nanoparticles; NPDs, nanopowders; NFs, nanofilms; NCBs, nanocubes; ε_r, Dielectric constant; tanδ, Dielectric dissipation factor; d_{33}, Piezoelectric constant; LC, Leakage current; k_p, Planar electromechanical coupling coefficient; P_r, Remanent polarization; E_c, Coercive electric field; T_c, Curie temperature point; γ, Relaxation behaviour; DC, Direct current.

4.3 Luminescent properties and applications

Luminescent PNMs have various applications including (light-emitting diodes) illumination sources and anti-counterfeiting labels.[124] Currently, their applications are still constrained by the low stabilization energy and weak ionic bonding ability. RE ions have abundant 4f levels and variable ionic valences, which show excellent optical properties and environmental stability when doped with perovskite matrix materials.[219] In addition, the spectral range of perovskites have been greatly broadened by incorporating RE elements.[75, 81, 220]As follows, we choose several representative optical mechanisms and optical applications for detailed comparison and introduction. [11, 32, 221, 222]

4.3.1 Luminescent materials

Song et. al. systematically studied the optical properties of Ln^{3+}-doped $CsPbCl_3$ NCs (Ln=Yb, Er, Dy, Tb, Eu, Sm, Ce).[36] The absorption spectra of the Ln^{3+}-doped $CsPbCl_3$ NCs exhibit blue shift with the increase of atomic number of the doped Ln^{3+} ions, which is due to the lattice shrinkage caused by the radius of lanthanide ion shrink. Compared with the undoped $CsPbCl_3$ NCs, Ln^{3+}-doped samples emit characteristic peaks of each Ln^{3+} ions (Fig. 17). Yb^{3+}-doped sample exhibit a high PLQY of 143% due to the quantum tailoring effect.[32, 221, 223] The electrons in the conduction band and the holes in the valence band reach the intermediate defect states, and then the energy transferred to Yb^{3+} ions. The PLQY of Eu^{3+} is low for the electrons on the excited state transferred to the non-radiative emission level.

Zheng et. al., synthesized $LiYbF_4$:0.5%Tm@$LiYF_4$ sensitized $CsPbX_3$ (X=Cl, Br, I).[224] The upconversion photoluminescence (UCPL) spectra of RE ions are used to stimulate the CsPbX3 QDs to emit the luminescence. Under NIR excitation, the RE-based nanoparticles emit blue-violet light that excites perovskite QDs, which makes the QDs emit luminescence (Fig. 18). By adjusting halide cations, perovskite QDs can be emitted from perovskite structure sensitized by RE nanomaterials under NIR laser irradiation. This study realizes the radiative energy transfer up-conversion (RETU) system.

4.3.2 Anti-counterfeiting labels

In order to raise the NIR emission, Zhang et.al delineated a Yb^{3+} and Yb^{3+}/Er^{3+} doping $CsPbCl_3$ NCs with the total PLQY increased from 5% to 127.8%.[219] Meanwhile, the doped $CsPbCl_3$ NCs are more stable than the undoped one. Furthermore, Zhou and co-workers successfully synthesized Yb^{3+}/Ce^{3+}-doped $CsPbCl_{1.5}Br_{1.5}$ NCs by the modified HI method, the NCs exhibited strong infrared emission peak at 980 nm with a high PLQY of 146%.[90]

Table 3 Summary of the perovskites-type, decay curve and applications of some representative doped RE.

Perovskites	Emission	PLQY	Decay Curve	Application	Ref.
$CsPbBr_3$	Ce^{3+}/515 nm	89%	12.69 ns	-	11
$CsPbCl_3$	Ce^{3+}/430 nm	24.3%	9.7×10^{-3} μs	-	36
	Sm^{3+}/605 nm	14.1%	600 μs		
	Eu^{3+}/620 nm	27.2%	714 μs		
	Tb^{3+}/550 nm	31.2%	598 μs		
	Dy^{3+}/572 nm	27.6%	583 μs		
	Er^{3+}/548 nm	15.1%	654 μs		
	Yb^{3+}/982 nm	142.7	588 μs		
$CsPb_xM_{1-x}Br_3$	Mn^{2+}/Eu^{2+}/492 ~ 520 nm	75%	5.04 ns	-	63
$Cs_2AgInCl_6$	Yb^{3+}/994 nm	100%	2.7 ms	-	75
$CsPbX_3$ (X=Cl, Br, I)	Ce^{3+}/Eu^{3+}/398~620 nm	50%	-	LED	98
	Ce^{3+}/Sm^{3+}/399~604 nm	38%			
	Bi^{3+}/Eu^{3+}/403~620 nm	40%			
	Bi^{3+}/Sm^{3+}/401~604 nm	26%			
	Ce^{3+}/Mn^{3+}/450~592 nm	72%	4.9 ns		
$CsPbBr_3$	Eu^{3+}/545 nm	-	0.82 ms	-	154
	Tb^{3+}/612 nm	-	0.37 ms		
$CsPbCl_3$	Yb^{3+}/Er^{3+}/986 nm	127.8%	941.9 μs	-	219
	Yb^{3+}/Er^{3+}/1533 nm	-	868.2 μs		
K_3InF_6	Eu^{3+}/615 nm Tb^{3+}/615 nm Er^{3+}/548 nm Er^{3+}/656 nm	-	0.64 ms 0.45 ms 0.59 ms 0.57 ms	-	163
$LiNbO_3$	Er^{3+}/543 nm	-	-	Anticounterfeiting/ Toxicity Tests	225
$CsYbI_3$	675 nm	58 %	23.3 ns	Photodetector	133
$CsPbCl_3$	Yb^{3+}/990 nm	190%	280 ps	-	226
$K_xCs_{1-x}PbCl_3$	Y^{3+}/410 nm	17.6%	12.41 ns	-	227
	La^{3+}/410 nm	15.8%	9.29 ns		
	Eu^{3+}/410, 438, 455, 473, 495 nm	31.2, 38.8, 50.5, 80.8, 89.9%	10.55 ns		
	Lu^{3+}/410 nm	8.7%	14.17 ns		
$RbPbI_3$	Yb^{3+}/Er^{3+}/763.50 nm	-	4.9 ns	Resonator	228
$CsSrI_3$	Yb^{2+}/426 nm ~ 442 nm	-	10 μs	-	229
$KMnF_3$	Yb^{3+}/Er^{3+}/660 nm	-	589 μs	Biolabeling	230
$KMgF_3$	Eu^{2+}/$^{3+}$/360-590 nm	30%	3.2 ms	RL dosimeter	231
$KMnF_3$	Nd/Yb/Er/668 nm	0.023%	100 μs	-	232
$CaTiO_3$	Eu^{3+}/619 nm	-	0.8 ms	Lighting device	233
$BaLaMgSbO_6$	Mn^{4+}/700 nm	83%	0.90 ms	LED	234

Oxide and fluoride perovskite NPs have unique upconversion/downconversion photoluminescence (UC/DCPL) properties and good thermal stability, such as La^{3+}:$CsPb(Cl_{0.7}F_{0.3})_3$, RE^{3+}:$LiNbO_3$ (RE = Pr, Tm, Er, Yb), and 2% Yb^{3+}(5% Mn^{2+}, 0.01% Er^{3+} or Ho^{3+}):$KCdF_3$. These materials can serve as multilevel anti-counterfeiting materials. As shown in Fig. 19A, letter, Chinese characters and image patterns were fabricated via nanoprinting on the paper where the patterns printed by $CsPb(Cl_{0.7}F_{0.3})_3$:La^{3+} QDs would appear under the 365 nm UV light. Moreover, the Tm^{3+}, Er^{3+}, or Pr^{3+}-doped $LiNbO_3$ presented a luminescent rainbow (Fig. 19B), which meet the most anti-counterfeiting needs at the present. In Fig. 19C, printed luminescent red flower and green leaves by the inks of 2% Yb^{3+}/5% Mn^{2+}/0.01% Er^{3+}-doped $KCdF_3$ and 0.01% Ho^{3+}-doped $KCdF_3$, respectively. The intense luminescence together with multiple nanoprinting patterns show great potential of this anti-counterfeiting technology.

4.3.3 Lighting and Display screens

As a class of luminescent materials, perovskites have pure luminescent chroma and adjustable spectral range, which is highly desired in the field of the high resolution display screen. However, most luminescent halide perovskites emit weak blue and red spectra, which limit their practical applications as the displays screen materials.[4, 40] Owing to the RE ions that can emit narrow and sharp blue and red spectra, the RE-doped perovskites complement each other and promote the application of perovskite materials in the field of display and light emitting diode (LED).

Yao et. al. used Ce^{3+} doped $CsPbBr_3$ NCs to encapsulate LED devices (Fig. 20). The devices with and without Ce^{3+} were evaluated with and without Ce^{3+} systematically. Both the $CsPbBr_3$, Ce^{3+}-doped $CsPbBr_3$ samples and corresponding devices emit narrow and strong emission peaks. With Ce^{3+} doping, the brightness enhanced with the increase of device voltage. The current density and current efficiency of the devices with Ce^{3+} addition are greatly improved. The external quantum efficiency (EQE) of the Ce^{3+} doped devices is higher than that of Ce^{3+} undoped devices different voltages, which gave the highest EQE of 4.4%. There are some RE-doped PNMs, their optical performances were listed in Table 3.

4.4 Detection and sensing

The optical, magnetic and electrical properties of RE-containing perovskites can be sensitive to various external stimuli including metal ions, gases, temperature, electromagnetic waves, etc. These materials can, therefore, be used to fabricate sensors， selectively detecting certain external stimulus. This section summarizes the applications of RE-containing PNMs as sensors (Table 4).

Table 4 Various sensors based on RE-containing PNMs.

PNMs	RE	Morphology	Stimulus	Sensing performance	Ref
$YMnO_3$	Y	NPs, 50 – 100 nm	NO_2,	180 °C, 30%@10 ppm, 1 min	14
$GdFeO_3$	Gd	NPs, 10 – 35 nm	NO	140 °C, 2 ppm, 1~2 min	104
Yb/Er,Er:$NaYF_4$, $MeNH_3PbBr_3$	Yb/Er, Er	NWs, d = 150 nm	NIR, 980 nm; 1532 nm	980 nm, 2.5 – 17.5 W/cm^2; 1532 nm, 5 – 30 W/cm^2	124
Au/Cl, $LaFeO_3$	La	NPs, 29 nm	Ethanol gas	100 ppm, T_p=120 °C	129
$CsPbBr_3$		QDs, ~12 nm	Yb^{3+},Cu^{2+}	2 nM – 2 μM	128
$NaMgF_3$	Eu^{2+},Ce	/	X-ray	12 Gy	132
$Y_{0.2}Sr_{0.8}TiO_3$	Y	NCbs, 20 nm	Temperature	$S_{bk,}$ ~ 890 μV/K, 500 °C	205
$PrFeO_3$	Pr	NPDs, 10 – 100 nm	CO_2	2.36 ppm; T_p, 200 °C; 72% RH	235
$EuPO_4$,$CsPbBr_3$	Eu	NCs, 50 –300 nm	Temperature	303 – 483 K, S_a = 0.082 K^{-1}, S_r = 1.80% K^{-1}; l min	236
$DyFeO_3$	Dy	NPs, 26 nm	H_2S	340 °C, 5×10^{-5} volume %	237
$DyCoO_3$	Dy	NPs 0.2 – 8 μm	UV	E_e=100 mW/cm^2, 2 min ~ 0.5 s; Δ*I*, 0.027 – 0.1 mA;	238

4.4.1 Ions and gas sensing

The detections of toxic ions and gases are pivotal for human health. Luminescent and electrochemical detection of toxic ion and gases are quite successful approaches due to their advantages of high sensitivity, convenience, fast response and low cost. In recent years, PNMs also show great potential in this emerging area.

One example is the selective detection of Cu^{2+} ions using $CsPbBr_3$ nanocrystals.[128] As shown in Fig. 21, the addition of different metal ions induces very different response of the PL intensities. Cu^{2+} effectively quenches the luminescence of $CsPbBr_3$, whereas the response is negligible for other ions with a detection limit as low as nM. These results demonstrated the great potential of PNMs in detecting metal ions.

In other reports, PMNs are used to detect volatile organic compounds (VOCs) and toxic gases. The $PrFeO_3$ nanopowders can be used to detect CO_2 at a low concentration of 2.36 ppm, under the relative humidity of 72% at 200 ºC.[235] Moreover, $YMnO_3$, $GdFeO_3$ and $DyFeO_3$ nanomaterials were applied to detect NO_2, NO and H_2S, respectively.[14, 104, 237] $LaFeO_3$ nanoparticles, surface modified by Au and Cl, have been used to detect ethanol (Fig. 22).[129] The Au atom and Cl atom on the surface of the $LaFeO_3$

nanoparticles inhibited the pollution of foreign carbon atoms. The oxidation of ethanol molecules on the surface of the nanoparticles formed La carbonate and adsorb the oxygen species. The calculation results showed that the Au and Cl atoms enhanced the charge transformation from ethanol to Fe-O and terminated on the surface of $LaFeO_3$ (001) face, which is both beneficial for the response of $LaFeO_3$ to ethanol. Thus, the detection limit reaches as low as 100 ppm at 120 ºC. This method is also suitable for the detection of other gases, providing a new idea for the VOCs sensing.[235]

4.4.2 Detection of heat and electromagnetic waves

It is well-known that the optical properties of luminescent materials can be sensitive to temperature. As shown in Fig. 23 (A) and (B), the emission of $EuPO_4$@$CsPbBr_3$ hybrid system changed under different temperature.[236] The emission intensity of $CsPbBr_3$ at 516 nm decreased with increasing temperature. However, the characteristic emission of Eu^{3+} at 593 nm, 611 nm and 700 nm showed negligible changes. The spectral change of the hybrid system as a function of temperature can be clearly read out on the chromaticity map. When the temperature increases from 303 K to 483 K, the colour of $EuPO_4$@$CsPbBr_3$ gradually changed from yellow-green to orange-red. Therefore, this composite structure is very suitable for thermal sensing.

In addition, the electromagnetic waves (x-rays, ultraviolet rays, etc.) can also change some electrochemical properties of the materials. Based on such effects, a series of materials have been developed to detect electromagnetic waves.[130, 231, 239] For example, $DyCoO_3$ was used for ultraviolet detection.[238] The photocurrent can clearly respond to repeatedly turning off-on of the ultraviolet lamp, and it is stable under repeated cyclic tests. The photocurrent shows a good linear relationship with the UV power, facilitating the applications as UV sensors.

4.5 Catalysts

The unique 4*f* electronic structure of RE elements may result in catalytic activities that are not observed in other compounds. To date, various RE-containing PNMs are reported as efficient catalysts in for water-splitting (OER, Oxygen evolution reaction, HER, Hydrogen evolution reaction), CO and CH_4 transformation, NO_x degradations, etc.

4.5.1 Water-splitting

Hydrogen is a clean, high-energy and recyclable power, which attracts tremendous attention. Searching for highly efficient and stable catalysts for water-splitting is essential to utilize the abundant water resources. HER and OER are two half reactions of water decomposition and are used to evaluate the performance of electrocatalysts. RE-containing oxide perovskite materials have been considered as promising electrocatalysts for water splitting due to their high OER activity. In addition, they are also good candidates for the photocatalytic water splitting.

Table 5 The experimental results of oxide perovskites and derivatives for water splitting applications.

Perovskites	RE^{3+}	Overpotential (V_{RHE}@-10 mA cm^{-2})	Intrinsic activities or Tafel slopes	Ref
$LaMn_{0.75}Co_{0.25}O_{3-\delta}$	La	1.66 V (OER)	97 mV $decade^{-1}$(Tafel slope)	28
$RNiO_3$	La, Nd, Sm, Gd	1.69 V (OER)	75 mV $decade^{-1}$(Tafel slope)	48
$LaNiO_3$	La	1.45 V (OER)	36 mV $decade^{-1}$(Tafel slope)	17
$LaFe_xNi_{1-x}O_3$	La	1.53 V (OER)	50 mV $decade^{-1}$(Tafel slope)	127
$La_{0.8}Sr_{0.2}MnO_3$	La	1.51 V (OER)	42 mV $decade^{-1}$(Tafel slope)	240
$La_{0.5}(Ba_{0.4}Sr_{0.4}Ca_{0.2})_{0.5}Co_{0.8}Fe_{0.2}O_{3-\delta}$/r-GO	La	0.28 V (OER) -0.338 V (HER)	46 mV dec^{-1} (Tafel slope for HER) 80 mV $decade^{-1}$(Tafel slope for OER)	241
$La_{0.2}Sr_{0.8}Co_{1-x}Fe_xO_{3-\delta}$	La	1.53 V (OER)	56 mV $decade^{-1}$(Tafel slope)	242
$La_{1-x}Sr_xNi_{0.8}Fe_{0.2}O_{3-d}$	La	1.60 V (OER)	70 mV $decade^{-1}$(Tafel slope)	243
$LaCoO_3$	La	0.47 V (OER)	180 mV $decade^{-1}$(Tafel slope)	244
$(Ln_{0.5}Ba_{0.5})CoO_{3-d}$	Pr, Sm, Gd, Ho	1.66 V (OER)	60 mV dec^{-1} (Tafel slope)	245
$LaCo_{1-x}Fe_xO_3$	La	1.63 V (OER)	0.27 mA $cmoxide^{-2}$@1.63 VRHE (MA)	246
$La_{1-x}Sr_xFeO_{3-\#}$	La	0.37 V (OER)	60 mV $decade^{-1}$(Tafel slope)	247
$LaCoO_3$	La	1.75 V (OER)	N/A	248
$PrBaCo_2O_{6-d}$	Pr	1.72 V (OER)	70 mV $decade^{-1}$(Tafel slope)*	249
$NdNiO_3$	Nd	1.63 V (OER)	70 mV $decade^{-1}$(Tafel slope)	250
$PrBa_{0.5}Sr_{0.5}Co_{1.5}Fe_{0.5}O_{5+\delta}$	Pr	1.62 V (OER)	58 mV $decade^{-1}$(Tafel slope)	251

4.5.1.1 Electrocatalysis

Many efforts have been devoted to developing the perovskites that possess prominent performance of OER and HER. For instance, the effects of different materials,[240, 241] elements,[48, 108, 127, 242, 243, 252] and microstructure,[17, 28, 48] were studied to improve the activity and stability of the electrocatalysts, achieving much progress. (HER catalysts were also facilitated to obtain superior performance.) Most of the concerns have been concentrated on the sluggish OER catalysts research.

$La_{0.5}(Ba_{0.4}Sr_{0.4}Ca_{0.2})_{0.5}Co_{0.8}Fe_{0.2}O_{3-\delta}$ perovskite nanorods were adhered to reduced graphene oxide (rGO) nanosheets to prepare the hybrid material as bifunctional electrodes, showing excellent performance of OER and HER concurrently in the alkaline media. It was operated at the voltage of 1.76 V at 50 mV cm^{-2}, which is highly close to the commercially IrO_2/C-Pt/C couple (1.76 V @ 50 mA cm^{-2}).[241] A two-step calcination method was applied to obtain the $LaMn_{0.75}Co_{0.25}O_{3-\delta}$ perovskite nanofibers showing highly promising OER activity that was comparable to the commercial RuO_2 catalysts and 26.5 times higher than that of the $LaMnO_3$ catalysts.[28] By a $FeCl_3$ post-treatment, the bulk crystalline $LaNiO_3$ perovskite was transformed into an amorphous nickel–iron-based motifs on the perovskite matrix, which exhibited a superior OER activity and an ultra-low overpotential of 189 mV at 10 mA cm^{-2}.[17] In addition, the La and Ni were partially substituted by Sr and Fe, respectively, to obtain the $La_{1-x}Sr_xNi_{0.8}Fe_{0.2}O_{3-\delta}$. The OER results showed that the Sr and Fe co-doped perovskite exhibited an excellent OER activity even above the benchmark RuO_2, which is attributed to the promising active sites of Ni^{3+}, O_2^{2-}/O^- and an optimized Ni/Fe ratio.[243] An Fe-doped $LaFe_xNi_{1-x}O_3$ nanorods also showed a remarkable performance of OER with a low overpotential of 302 mV at 10 mA cm^{-2} and a small Tafel slope of 50 mV dec^{-1}.[127] Table 5 listed some electrocatalysts for water splitting.

To improve the performance of OER and HER electrocatalysts, the chemical properties of the surface and the conductivity of the material are important, both greatly affected by the electronic structure. Recently, many new perovskites have been developed as highly active electrocatalysts for water-splitting. The double perovskites $(Ln_{0.5}Ba_{0.5})CoO_{3-d}$ (Ln=Pr, Sm, Gd and Ho) has been reported to be a family of highly active catalysts for OER.[245] It was found that the RE-containing perovskite was much more stable than common pseudo-cubic perovskites with comparable OER actives. The high activity and stability of these double perovskites were ascribed to the appropriate distance between O p-band center and the Fermi level modified by the RE elements' adjustment. After that, the $LaCoO_3$ film grows on the $LaSr_{1-x}Mn_xO_3$ (LSMO) film by PLD was reported to exhibit a higher OER activity than that of benchmark catalysts.[248] The band gap of Co 3d-O 2p decreased due to the transfer of electrons from LSMO to the $LaCoO_3$ film, inducing the closer distance between O 2p band center and Fermi level. This indicated the lower activation energy and prominent OER activity.

$LaCoO_3$ showed remarkable performance in the base for oxygen evolution reaction, so it was often chosen as the substrate to study the electronic structure-function effect of single perovskites[244, 246, 248]. By the sol-gel method, the Fe substitution was introduced to the $LaCoO_3$ obtaining the $LaCo_{1-x}Fe_xO_3$ to improve the performance.[246] With 10% Fe substitution, there appeared a Co^{3+} spin-state transition from generally low spin state to a high spin state and enhanced Co 3d-O 2p covalency, which resulted in a transition from insulator to half-metal and promoted OER performance for $LaCo_{0.9}Fe_{0.1}O_3$. Besides the substitution, as shown in Fig. 24 D-E, lattice-orientation control growth of $LaCoO_3$ epitaxial films was applied as the strategy to optimize the spin-state regulation of the $LaCoO_3$ perovskite.[244] A spin-state transition of cobalt from a low spin state (LS $t_{2g}^6e_g^0$) to a high spin state (IS $t_{2g}^5e_g^1$) was induced by different distortion degrees of the CoO_6 octahedron for different lattice-oriented $LaCoO_3$ films. Hence, $LaCoO_3$ (100) film presented lower adsorption free energy, higher conductivity and better OER performance than the other two films.

In addition to the modulation of the electronic structure of the perovskites, the control of surface oxygen vacancies has become one of the most important issues for catalysts of water splitting. A series of Sr-doped perovskite oxide $La_{1-x}Sr_xFeO_{3-\delta}$ was synthesized by a bulk iodometric titration method[247]. $La_{0.2}Sr_{0.8}FeO_{3-\delta}$, with the optimum amount of surface oxygen vacancies and higher surface Fe valence states, exhibited the best performance of OER. As shown in Fig. 24 A-C, Liu et al. reported that the OER performance of $PrBa_{0.5}Sr_{0.5}Co_{1.5}Fe_{0.5}O_{5+\delta}$ was significantly improved by controlling the oxygen vacancies. The results indicated that the excessive oxygen defects facilitated the OH^- affiliation and brought lowered the formation energy of O^* on the surface, greatly boosting the OER kinetics.[251] A series of RE nickelates films ($RNiO_3$; R= La, $La_{0.5}Nd_{0.5}$, $La_{0.2}Nd_{0.8}$, Nd, $Nd_{0.5}Sm_{0.5}$, Sm, and Gd) ware studied for the OER performance.[48] Through changing the composition of the catalysts, the partial reduction of Ni^{3+} to Ni^{2+} induced by the oxygen vacancies evidentially improved the OER activity. However, the oxygen vacancies on the catalysts are not always beneficial for the catalytic process of water oxidation. The role of oxygen vacancies is still controversial. Shi et al. found that largely increasing the concentration of oxygen vacancies led to a significant reduction in the intrinsic OER activity. Structural studies revealed that oxygen vacancies tended to orderly align in $PrO_{1-\delta}$. This ordered structure not only lowers the cobalt oxidation states but also triggers a spin-state transition from high-spin to low-spin states for cobalt ions, both greatly slowing the OER kinetics.[249]

Table 6 The experimental results of oxide perovskites for photocatalytic water splitting.

Perovskites	RE^{3+}	Bandgap	Incident light	Scarification regents in the solutions	Electro-catalyst	Activity	Ref.
$LaSrFeO_4/La_2SrFe_2O_7$	La	2.16 eV	> 250 nm	Neutral phosphate buffer	1 wt% Pt	477 μmol h^{-1} g^{-1}	253
$LaFeO_3$	La	2.16 eV	575 nm	0.1 M NaOH	W/O	−0.1 mA cm^{-2} @1.41 V	254
$LaNiO_3/CdS$	La	2.4 eV	420 nm	W/O	W/O	3700 μmol h^{-1} g^{-1}	255
$LaFeO_3$- 0.75PANI	La	1.92 eV	> 420 nm	10% triethanolamine	3 wt% Pt	3080 μmol h^{-1} g^{-1}	256
$LaGa_{0.4}Co_{0.6}O_{3-\delta}$	La		> 420 nm	W/O	1.0 at% IrO_x	470/717 μmol h^{-1} g^{-1}	257
$LaFeO_3$	La	2.19 eV	> 420 nm	50 mM $AgNO_3$	2 wt% Au	23 μmol/202 μmol h^{-1} g^{-1}	110
$LaTaON_2$	La	1.94 eV	420 nm<a<620 nm	20 % methanol	0.5 wt% Rh	110 μmol h^{-1} g^{-1}	31
$LaTa_{0.9}Zr_{0.1}O_{1+y}N_{2-y}$	La	1.99 eV	$\lambda > 420$ nm	50 mM $AgNO_3$	1 wt% Pt	110 μmol h^{-1} g^{-1}	258
10%Er-$K_2Ta_2O_6$	Er	3.50 eV	$\lambda \geqslant 270$ nm	10% formic acid	W/O	4620 μmol h^{-1} g^{-1}	259
Er-$KTaO_3$	Er	3.37 eV	$\lambda \geqslant 270$ nm	10% formic acid	2% Pt	24705	260
Pr-$KTaO_3$	Pr	W/O	$\lambda \geqslant 270$ nm	10% formic acid	2% Rh	19830	260
Pr-$K_2Ta_2O_6$	Pr	4.40 eV	$\lambda \geqslant 270$ nm	10% formic acid	2% Pt	27948	260
Er-$K_2Ta_2O_6$	Er	W/O	$\lambda \geqslant 270$ nm	10% formic acid	2% Rh	11082	260

4.5.1.2 Photocatalyses

Besides the electrocatalysis, the perovskite-type materials are also promising photocatalysts for water splitting. To promote the performance of the photocatalysts for HER, many strategies have been developed, such as interface engineering,[256-258] energy-band engineering,[254, 259, 260] and crystal structure modulation.[31, 110, 255]

Similar to the electrocatalysts, surface structure and property of the perovskite materials are extremely important for photocatalysts. It was reported that higher surface hydrophilicity of the catalysts enhanced the photocatalytic activity of water oxidation reactions (listed in Table 6). Thus, Zr was doped into the structure of the $LaTaON_2$ to induce better surface hydrophilicity and mesoporous microstructures, which led to a more efficient mechanism of the reaction to facilitate water oxidation.[258] Besides, $LaFeO_3$ was coated by conductive polyaniline (PANI) aerogel to modify the surface hydrophilicity, showing a promoted photocatalytic performance, because of elevated effects for water adsorption and diffusion, visible-light (photon) adsorption and photoinduced carries transfer.[256] The redox ability of the catalysts is also important for photocatalysts. A Sr- and Co-doped $La_{1-x}Sr_xGa_{1-y}Co_yO_{3-\delta}$ perovskite exhibited much higher H_2 production than the benchmark without doping, attributed to the lower activation energy.[257] As shown in Fig. 24 F-G, the highly active crystal phase and structure of the perovskites have been studied. With K and Na doping, the $LaKNaTaO_5$ plates gradually transformed to core-shell $LaTaON_2$, exposing more active (010) faces to promote the H_2 evolution activity to 4 times higher.[31] The p-type $LaFeO_3$ and $LaSrFeO_4$ have an ideal bandgap and band edge positions for overall solar water splitting.[253, 254] The oxides have been prepared and the physicochemical properties such as surface area, optical absorption and crystal structure are modified to acquire superior photocatalytic performances.

The properties and origins of the charge carriers are one of the most crucial factors for photocatalysts. The heterostructure of $LaNiO_3/CdS$ showed highly improved H_2 production performance, ascribed to the effective separation and transport of photoinduced charge carriers.[255] The plasmon-based $Au/LaFeO_3$ composite photocatalyst was built to enhance the activity for water reduction and oxidation, and the complex effects of hot electrons and holes for the reaction were investigated.

4.5.2 Removal of pollutants

Clearing up nitrogen oxides, carbon monoxide and other pollutants have great significance on environment protection. RE-containing oxide perovskite materials can possess the excellent catalytic activity and high-temperature stability, thus can be widely used in the catalytic degradation of nitrogen oxides and other pollutants (dye molecules, phenol, and etc.).

4.5.2.1 Water treatment

Perovskites are effective photocatalysts for the degradation of various organic compounds in water. A series of perovskite-type titanate $M_xTi_yO_z$ (M= transition and RE metals) compounds with different structures and sizes were synthesized by the thermal decomposition method.[261] The relationship between bandgap and crystalline sizes were identified: smaller crystallite sizes induced lower band gaps, resulting in stronger visible light absorption and better performance of pyrocatechol degradation. The new double perovskite Dy_2ZnMnO_6 nanoparticles were successfully synthesized and applied as the photocatalyst of the degradation of methyl violet and methyl orange.[262] The novel $LaFeO_3$ perovskites partially substituted with Ti have been synthesized via a sol-gel method.[262] After substitution of Ti, the catalyst exhibited a greatly improved stability, which is attributed to the fewer Fe leaching during the reaction. The RE-doped $K_2Ta_2O_6$ perovskites were successfully synthesized and exhibited greatly improved degradation efficiency under UV–vis light compared with pristine $K_2Ta_2O_6$.[259]

To obtain the materials with superior photocatalytic performance, perovskites have been modified by forming composites with other functional units. Fig. 25A-B showed that the heterostructures of $LaFeO_3/Ag_2CO_3$ nanocomposites were successfully constructed and showed a very high electron−hole pair decoupling efficiency, resulting in the greatly improved photocatalytic activity for the degradation of rhodamine B (RhB).[113] Moreover, the Au/La-$SrTiO_3$ showed a superimposed effect of Au nanoparticles and La-doping, inducing a good photocatalytic activity in photodegradation of RhB.[166] The $CuO/LaFeO_3$ nanocomposite synthesized by the sol-gel method exhibits an outstanding activity of degradation of RhB, attributed to the simultaneous effects of the photocatalysis.[263] RE ions (Er, Pr) doped $KTaO_3/K_2Ta_2O_6$ photocatalysts were decorated by monometallic nanoparticles (Au, Pt, Rh), resulting in boosted photocatalytic performance compared with that of pristine $KTaO_3/K_2Ta_2O_6$.[260]

4.5.2.2 Automobile exhaust

NO_x, CO and CH_4 from the incomplete combustion of the fuel have been considered as main pollutants in the air. It is, therefore, essential to develop catalysts such as perovskite materials to eliminate these pollutants due to their high electroactivity in degradation.

For the NO_x degradation, the oxidation and reduction reaction have been both applied. The Mn-based[264, 265] perovskites with porous nanostructure have been successfully synthesized and exhibited rather well performance of NO oxidation. Furthermore, as shown in Fig. 25C-D, when La was substituted by the Co, the activity of NO oxidation was further improved.[264] The Cu-doped perovskite $LaCoO_3$ that was doped by Cu showed prominent activity than the pristine oxide.[266] The reduction of the NO were performed with the NH_3[115, 136]or CO[267-269] reactant gases. $La_{1-x}Ce_xMnO_3$/attapulgite nanocomposites were synthesized by the sol-gel method with different doping fraction of Ce. When the doping fraction x was 0.1, the highest activity of NO reduction was obtained.[115] $LaBO_3$/attapulgite (ATP) (B=Mn, Fe, Co, Ni) composites were prepared, and the order of NO reduction capacity was is $LaMnO_3$/ATP > $LaNiO_3$/ATP > $LaFeO_3$/ATP > $LaCoO_3$/ ATP.[136] Pure perovskite $LnFeO_3$ (Ln = La, Pr-Tb) porous hollow spheres and solid spheres (Ln = Dy-Yb, Y) were successfully synthesized, in which the activities of hollow spheres were obviously higher than those of the solid spheres.[267] Fig. 25 E-F showed that the $LaFeO_3$ with hierarchically porous structure was successfully prepared and showed the remarkable performance of the NO reduction reaction.[268]

Meanwhile, the oxidation of the CH_4 is crucial for green gas reduction.[270] The $La_{0.5}Ba_{0.5}MnO_3$ nanocubes have been synthesized and presented a high activity and stability for oxidation of the CO and CH_4.[114] A novel double perovskite $La_{2-x}Sr_xNiAlO_6$ catalyst showed the excellent catalytic activity with 0.1 fractions of Sr doping showed the excellent activity for CH_4 combustion.[271] The RE-containing double perovskite oxide La_2CoMnO_6 supported on CeO_2 was synthesized by three methods, and the activity of CH_4 combustion was: co-precipitation > sol-gel > impregnation.[160] The calcination temperature of preparation of perovskite-type $LaFeO_3$ oxides was reported to make a great effect on the performance of CH_4 oxidation.[111]

4.5.3 Carbon and Nitrogen conversion

The conversion of carbon-based compounds is an important chemical reaction in industry. For the special structure and chemical inertia, RE-containing oxide perovskites have very important applications in the conversion of carbon chemicals, such as the oxidative coupling of methane, oxidation of methanol or urea, conversion of carbon dioxide, and etc. Many RE oxide perovskites exhibit flexible redox properties, high surface oxygen mobility, abundant surface active sites and good thermal stability, which is applicable in a wide range of applications in traditional heterogeneous catalysis for chemical product and energy industry.[134, 272-278]

Methane convert to C2 hydrocarbons (ethane and ethylene) by oxidative coupling (OCM) is a promising direct methane conversion technology, which has been investigated extensively during the last three decades. Sekine et al. reported that $La_{0.7}Ca_{0.3}AlO_{3-\delta}$ catalyst exhibited high CO_2-OCM activity in an electric field with a C2 yield of 7.4% at 348 K, attributed to the Ca doping.[275] Jung et al. investigated the effect of pH values during $LaAlO_3$ preparation on the OCM activity. It was found that the sample prepared at pH = 8 presented the highest C2 yield due to its well-developed oxygen vacancies and electrophilic lattice oxygen.[272]

Another important route of the methane transformation is to the syngas by the partial oxidation of methane (POM)[277] or dry reforming of methane (DRM)[274]. The layered perovskite material noted as $La_{1+x}Sr_{1-x}CoO_4$ (x = 0; 0.25) and $NdCaCoO_{3.96}$ was synthesized by the solid state method, which has better stability and higher activity in the reaction of partial oxidation of methane to syngas. This originated from the different effects of alkali metals.[277] The synergistic La-Ce effect was applied to optimize the reactivity of DRM by CO_2 on the supported perovskite La_xCe_{1-x}-Fe_2O_3/Al_2O_3. With the assistance of La-Ce effect, the reactivity of the catalysts was greatly enhanced due to the promoted lattice oxygen migration.[274] As shown in Fig. 26, Gao et al. prepared the $LaMnO_3$-Pt coated on ZnO nanoarray by a simple low-temperature hydrothermal synthesis method. Pt was uniformly distributed on the surface of the catalyst, which greatly increased the oxidation of propane.[273] The most effective routes for the production of hydrogen without Cox byproducts are methane and ammonia decomposition.[276, 279] Pudukudy reported the successful synthesis of a set of porous CeO_2, zirconia and lanthana supported nickel catalysts for H_2 generation. It was noted that the lanthana-based perovskite formed during the reaction greatly improved the reactivity.[276]

4.6 Magnetics

The unpaired electrons in oxide perovskites containing transition metal ions (TM: Fe, Co, Ni, Mn, etc.) and RE ions (RE: Gd, Sm, Tb, Ho, etc.) can result in excellent magnetic properties. Those magnetic materials are of great significance in the application of magnetic devices and spintronic devices.[280, 281]

4.6.1 Ferromagnetic, antiferromagetic, and superparamagnetic materials

Table 7 The RE-based perovskite material for superconductor, electronic, magnetic devices

Perovskites	RE	Synthesis	Morphology	Magnetics; Application	Ref.
$La_{0.7}Sr_{0.3}MnO_3$	Gd, Tb, Dy, Ho	SG	NCs, ~30 nm	T_C=320-330K,	[282],
$LnFeO_3$	Eu, Gd, Tb	SG	NPs,30-115 nm	T_C=5-8K; Bioimaging	[283]
$BaTiO_3$	Eu	SG	NCs, sub 15 nm	No date	[284],
$YbMnO_3$	Yb	ST	NRs/NPLs 50-200 nm	TN~86K;	[285],
$LaFeO_3$	Ti	CP	NPs		[77],
$LaFeO_3$	Ce	CP	NPs	M_S=0.56 emu/g;	[140],
$Ce_{1-x}Eu_xCrO_3$	$Ce_{1-x}Eu_xCrO_3$	CBs	NPs, 50-100 nm	T_C=280 k/3.5T, TN~182 K;	[286]
$BiFeO_3$	Ce	SG	NPs, 30-50 nm	MH,1.766 emu/g; Mr 0.0572 emu/g; H_C 0.1468 KOe	[287]
$BiFeO_3$	Ho	SG	NPs,	Ms=5.3 emu/g, Mr =1.5 emu/g, H_C=140 Oe	[288]

Both TM and RE ions can have unpaired electrons, which endowing excellent magnetic properties many TM and RE oxide perovskites. In particular, RE-based oxides combined with nickel, cobalt, and iron have been extensively studied for their ferromagnetic and antiferromagnetic phase transitions. This provides both theoretical and experimental supports for the development of new magnetic materials.[289-291]

Despite its importance, there are limited research focusing on the quantum size and crystal structure effects on the magnetism of RE PMNs reported.[292] As the description in Fig. 27A, the saturation M/H curves of bulk-phase $La_{0.7}Ca_{0.3}MnO_3$ at 5, 100 and 200 K, respectively. Contrarily, curves measured on nano $La_{0.7}Ca_{0.3}MnO_3$ show no sign of saturation at all below (Fig. 27B). The coercive field of nano sample at 5 K is more than two orders of magnitude higher than that of bulk phase. The authors attributed the results to the size effect, which led to a strong frustration of ferromagnetic ordering in nano $La_{0.7}Ca_{0.3}MnO_3$ as compared to basically stable and homogeneous ferromagnetic ground state in bulk. The parent host $PrFeO_3$ showed superparamagnetic behavior (Fig. 27C, D). Through introducing Al^{3+} cations into the $PrFeO_3$ (site-B) with the adjustment of different proportion, the magnetization can be greatly improved.[293-295] Such observation was likely because the introduction of the ferromagnetic component results in the weaker antiferromagnetic coupling between iron spin moments and the rearrangement in $PrAl_xFe_{1-x}O_3$ nanocrystals than that of $PrFeO_3$. These results unambiguously demonstrate that quantum size and crystal structure have significant effects on the magnetism of REs host perovskite-type oxides nanomaterials.

4.6.2 Magnetocaloric materials

The entropy changes of RE-based perovskite materials between magnetic ordering and disordering states result in a magnetocaloric effect, suitable for magnetic refrigeration.[23, 296, 297] As depicted in Fig. 28A, the initial randomly oriented magnetic moments are aligned by a magnetic field, resulting in the heating of the magnetocaloric material. This heat is removed from the material to the ambient environment by heat transfer. Upon removing the field, the magnetic moments randomize, which leads to the cooling of the material below ambient temperature. The heat from the cooling process of the system can then be extracted using a heat-transfer medium. Depending on the operating temperature, the heat-transfer medium may be water (with antifreeze), air or, for very low temperatures, helium. This technology, owning the merits of high security, low energy consumption and low pollution, is expected to replace the traditional compressed liquid refrigeration. Therefore, it is of great importance to develop high-performance RE-based perovskite magnetocaloric materials.

Recently, RE-containing PNMs have been demonstrated as excellent candidates for magnetic refrigeration based on the enhanced magnetocaloric effect. Ddue to an enhanced magnetocaloric effect.[292, 298] The intense interest in perovskite-type manganese oxides $R_{1-x}B_xMnO_3$ (where R is a RE ion and B is a divalent alkali) is initially prompted by the observation of colossal magnetoresistance.[23] However, they also exhibit large magnetocaloric effects (Fig. 28B) associated with the transition from a second order ferromagnetic to a paramagnetic state near room temperature. The magnetic entropy change ($-\Delta S_M$) of 3.28 J $kg^{-1}K^{-1}$ with a relative cooling power of 120 J kg^{-1} and an adiabatic temperature change (ΔT_{ad}) of 2.11 K at 310 K under 50 kOe magnetic field are already comparable to the best Gd-based clusters.[23] In addition, the magnetic cooling performance of exfoliated nanosheets may be even better (Table 7). With excellent processability and facile large-scale production, RE-containing PNMs have opened up a new avenue and therefore are extremely worthwhile to be explored.

5. Conclusions and prospect

In this review, we summarize RE-containing PNMs with great compositional turnability, structural variability, and broad applications in optics, photovoltaics, catalysts, dielectrics, magnetics, etc. The intrinsic reasons for the property improvements induced by RE elements are briefly discussed, providing a valuable reference for the design and application of RE-containing new functional materials. Although several problems and challenges exist, the research on RE-containing perovskites is highly prospering. New opportunities associated with RE-containing PNMs such as high efficiency, superior stability, the ease of mass production, models for fundamental research, environmental protection, and interdisciplinary, will be outlooked in the following section.

5.1 High efficiency and stabilities

Although lead halide ($APbX_3$, X=Br, I) perovskites have been widely used in photovoltaics with high PECE, there is still a considerably big gap between the current PECE and its theoretical maximum. In addition, the poor stability of $APbX_3$ makes them easy to decompose and thus lose photovoltaic activity in a humid environment. Improving the PECE and stability of $APbX_3$ perovskite materials is significant for their future applications. In addition, as the photoactive materials in solar cells, perovskites (oxides, $BaSnO_3$, $TmFeO_3$, etc.; halides, $Cs_3Bi_2X_9$, $CsSnX_3$, Cs_2AgSbX_3, etc., X=Br, I.) cannot absorb NIR light. By incorporating RE into perovskite structures, it is possible to improve the absorption efficiency of solar light in the NIR range, and thus enhancing the PECE. The incorporation of RE ions can also adjust the band gap of perovskites and improve the performances of the devices. Another important area is to replace $APbX_3$ with lead-free perovskites. The application of halide perovskites as illumination sources is also hindered by the low EQE and poor stability. It is therefore of both fundamental and practical importance to improve the EQE and stability of perovskite-based illumination sources. The exploration of white-light illumination sources is also desirable and current white-light perovskite-based devices are very rare.

In catalytic applications, some halide perovskites indeed show good photo-catalytic activity, but with poor stability. To the best of authors' knowledge, there is no report regarding the catalytic performances of RE-containing halide perovskites. The exploration of RE-containing halide perovskites is, therefore, a promising area. Although oxide perovskites have been widely used in various catalytic reactions including ORR, OER, NO_x elimination, etc., the catalytic performances still need to be improved. The incorporation of RE ions with various radius and valences into perovskite structure will yield defects, strains and oxygen vacancies, and therefore enhance the catalytic performances in the reaction of ORR, carbon or nitrogen transformations.

Selective RE doping has made some breakthroughs in improving the dielectric, piezoelectric, thermoelectric and ferroelectric properties of perovskites. However, from the material compositional design point of view, there are still great challenges for RE-doped perovskites to meet the requirements of high-temperature piezoelectrics and sensor in commercial applications. The development and design of perovskite materials with high transition temperature, high dielectric and piezoelectric constants are urgently needed.

RE-based oxide perovskites are excellent electrode materials of solid oxides fuel cells with high activity and energy conversion efficiency (~60%). However, the efficiency is still considerably lower than the theoretical value. In addition, the high operation temperature and acidic (or basic) environment pose great challenges to the stability of electrodes. All of these important issues must be resolved. In the case of metal-air batteries, although some highly active catalysts have been designed, the fabrication of high-capacity, stable and efficient batteries is still difficult. Therefore, it is essential to explore reliable battery assembly process and find suitable electrode materials. Besides, the match between electrolyte and electrode materials is an important factor for high capacity batteries.

When used as magnetic materials and detectors, oxide perovskites have high stability but are rarely involved in biomedical magnetic resonance imaging. It may have great potential for researches. In addition, the majority of magnetic devices and spin devices are still in the stage of fundamental research, requiring considerable efforts to promote practical applications. Meanwhile, achieving high selectivity and sensitivity is always desirable for the detection of unknown substances. The application of perovskites in analysis and detection is a new area.

5.2 Green and Mass Production

The mass production of RE-containing perovskites is a prerequisite for their applications. The fabrication of solar cells requires large-scale preparation of halide perovskite thin films, with low cost and simple and efficient fabrication processes. The application of oxide perovskites as catalysts and electrolytes requires materials with tunable size, high crystallinity, adjustable catalytic active sites and good dispersion. It is a great challenge to the preparation of nanomaterials.

With the rising of wearable technology, the fabrication of flexible devices opens up great opportunities for perovskite materials. In particular, the large-scale preparation of flexible solar cells, flexible sensors, flexible capacitors and batteries has boosted the development of RE-containing PNMs. In the process of batch production, several factors including the cost, environmental protection and market demand must be balanced. All of these considerations are directly related to the commercial success of devices, and even determine the future development of this field.

5.3 Fundamental researches

Although some studies have shown that perovskite materials play important roles in the fields of luminescent materials, catalysts, dielectrics, magnetics, solid-state batteries and sensors, most of the studies are still preliminary. The details of how RE-doping improves the performance of perovskite materials, by modulating the composition, local structure and molecular orbitals, are still unclear. Especially, the studies on the changes such as phases, vacancies, stress and defects induced by doping are still empirical and lack of theoretical interpretations. The reliance on expensive and state-of-the-art characterization tools also limits the further exploration of mechanism. The development of new materials, especially RE-containing materials, may create new structures and therefore new functionalities, among which some have been predicted theoretically. It is essential for their syntheses and characterizations.

5.4 Environmental protection

Although lead-based halide and oxide perovskites can exhibit excellent properties in applications such as luminescent materials, solar cells, and dielectric materials, Pb is harmful to both the environment and human health. Moreover, the replacement of precious element-based perovskites with RE-containing perovskites are beneficial for broad applications. Currently, lead-free perovskite materials have shown great to achieve similar or even better photovoltaic performances. It has been demonstrated that the incorporation of RE regulates the valence band as well as the light absorption ability of lead-free perovskite materials. On the other hand, the catalytic activity of some RE-containing perovskite materials has become comparable to that of noble metals, but the stability of these oxides is still poor. To meet the Green Chemistry criteria, the preparation and application of perovskite materials should utilize environmental-friendly raw materials, high-efficiency preparation processes, and minimal waste discharges.

5.5 Interdisciplinary studies

Perovskite materials are is the focus of many disciplines. The study of RE-containing perovskite materials requires knowledge from many disciplines such as theoretical physics, chemistry, materials science, optical engineering, electromagnetics, biomedicine, etc. The interdisciplinary collaborations are therefore essential. We encourage more scientists in various fields to pay attention to this emerging field and promote the applications of perovskite materials.

Abbreviations and acronyms lists

Ln	lanthanides
RE	rare earth
PNMs	perovskite nanomaterials
t	tolerance factor
μ	octahedral factor
0D	zero-dimensional
1D	one-dimensional
2D	two-dimensional
3D	three-dimensional
PSCs	perovskite solar cells
PECE	photoelectric conversion efficiency
PL	photoluminescence
FWHM	full width at half maximum
OER	oxygen evolution reaction
ORR	oxygen reduction reaction
HER	hydrogen evolution reaction
acac	acetylacetone

WC	wet chemical
SG	sol-gel
TD	thermal decomposition
HI	hot injection
ST	solvothermal method
CP	co-precipitation
ODE	1-octadecene
TEM	transmission electron microscope
OA	oleic acid
OM	oleylamine
HT	high-temperature method
SS	solid state synthesis
MS	molten salt reaction
SCT	spin coating technique
PLD	pulsed laser deposition
ES	electrostatic spinning
CVD	chemical vapor deposition
PCE	power conversion efficiency
V_{oc}	open-circuit voltage
J_{sc}	short-circuit current density
FF	fill factor
NIR	near Infrared
ETM	electron transport material
NPs	nanoparticles
NPLs	nanoplates
NCs	nanocrystals
NWs	Nanowires
NPDs	nanopowder
NTs	nanotubes
QD	quantum dots
NCbs	nanocubes
T_p	sensors working temperature
S_a	absolute temperature sensitivity
S_r	relative temperature sensitivity
S_{bk}	Seebeck coefficient
UV	ultraviolet light
EQE	external quantum efficiency
MPB	morphotropic phase boundary
CP	columbite precursor method
RT	Room temperature
MBM	mechanochemical ball milling
PR	Pechini method
CCB	citrate auto combustion method
ME	micro-emulsion route
ATP	attapulgite
NFs	nanofilms
ε r	Dielectric constant
$\tan\delta$	Dielectric dissipation factor
d_{33}	Piezoelectric constant
L_C	Leakage current
K_p	Planar electromechanical coupling coefficient
P_r	Remanent polarization
E_c	Coercive electric field
T_c	Curie temperature point
γ	Relaxation behaviour

DC	Direct current
CB	conduction band
VB	valence band
MA	methyl amine
LHPs	Lead-based halide perovskites
UCPL	Upconversion photoluminescence
RETU	radiative energy transfer up-convsrsion
UC	upconversion
DCL	downconversion luminescence
EL	electroluminescence
PL	photoluminescence
QY	quantum yield
rGO	reduced graphene oxide
PAN	l polyaniline
RhB	rhodamine B
OCM	Oxidative coupling of methane
POM	partial oxidation of methane
DRM	dry reforming of methane
TM	transition metal
RP	Ruddlesden-Popper
AIE	A-site ionic electronegativity
H_C	coercivity
M_H	maximum magnetization
M_S	saturation magnetization
Mr	remnant magnetization
T_N	Neel temperature
CBs	Combustion method
VOCs	volatile organic compounds

Conflicts of interest

The authors declare no competing financial interest.

Acknowledgements

We gratefully acknowledge the support from the China National Funds for Excellent Young Scientists (21522106), National Natural Science Foundation of China (21971117, 21771156), 111 Project (B18030) from China, the Open Funds (RERU2019001) of the State Key Laboratory of Rare Earth Resource Utilization and the Functional Research Funds for the Central Universities, Nankai University (ZB19500202), and the Early Career Scheme (ECS) fund (Grant No.: PolyU 253026/16P) from the RGC of Hong Kong.

References

1. J. Shamsi, A. S. Urban, M. Imran, L. De Trizio and L. Manna, *Chem. Rev.*, 2019, **119**, 3296-3348.
2. Y. Zhang, W. Jie, P. Chen, W. Liu and J. Hao, *Adv. Mater.*, 2018, **30**, 1707007.
3. H. Zhu, P. Zhang and S. Dai, *ACS Catal.*, 2015, **5**, 6370-6385.
4. Y. Wei, Z. Cheng and J. Lin, *Chem. Soc. Rev.*, 2019, **48**, 310-350.
5. W.-J. Yin, B. Weng, J. Ge, Q. Sun, Z. Li and Y. Yan, *Energy Environ. Sci.*, 2019, **12**, 442-462.
6. J. Vieten, B. Bulfin, P. Huck, M. Horton, D. Guban, L. Zhu, Y. Lu, K. A. Persson, M. Roeb and C. Sattler, *Energy Environ. Sci.*, 2019, **12**, 1369-1384.
7. Z. Li, Q. Xu, Q. Sun, Z. Hou and W.-J. Yin, *Adv. Funct. Mater.*, 2019, **29**, 1807280.
8. M. J. Cliffe, E. N. Keyzer, M. T. Dunstan, S. Ahmad, M. F. L. De Volder, F. Deschler, A. J. Morris and C. P. Grey, *Chemical science*, 2019, **10**, 793-801.
9. L. Wang, H. Zhou, J. Hu, B. Huang, M. Sun, B. Dong, G. Zheng, Y. Huang, Y. Chen, L. Li, Z. Xu, N. Li, Z. Liu, Q. Chen, L. D. Sun and C. H. Yan, *Science*, 2019, **363**, 265-270.
10. R. Saha, A. Sundaresan and C. N. R. Rao, *Mater. Horiz.*, 2014, **1**, 20-31.

11. J. S. Yao, J. Ge, B. N. Han, K. H. Wang, H. B. Yao, H. L. Yu, J. H. Li, B. S. Zhu, J. Z. Song, C. Chen, Q. Zhang, H. B. Zeng, Y. Luo and S. H. Yu, *J. Am. Chem. Soc.*, 2018, **140**, 3626-3634.
12. Y. Cheng, C. Shen, L. Shen, W. Xiang and X. Liang, *ACS Appl. Mater. Interfaces*, 2018, **10**, 21434-21444.
13. J. Miao and F. Zhang, *J. Mater. Chem. C*, 2019, **7**, 1741-1791.
14. T. Addabbo, F. Bertocci, A. Fort, M. Gregorkiewitz, M. Mugnaini, R. Spinicci and V. Vignoli, *Sens. Actuators, B*, 2017, **244**, 1054-1070.
15. Z. Shi, J. Guo, Y. Chen, Q. Li, Y. Pan, H. Zhang, Y. Xia and W. Huang, *Adv. Mater.*, 2017, **29**, 1605005.
16. E. Grabowska, *Appl. Catal., B*, 2016, **186**, 97-126.
17. G. Chen, Y. Zhu, H. M. Chen, Z. Hu, S. F. Hung, N. Ma, J. Dai, H. J. Lin, C. T. Chen, W. Zhou and Z. Shao, *Adv. Mater.*, 2019, **31**, e1900883.
18. C. Wei, R. R. Rao, J. Peng, B. Huang, I. E. L. Stephens, M. Risch, Z. J. Xu and Y. Shao‐Horn, *Adv. Mater.*, 2019, **31**, 1806296.
19. F. Polo-Garzon and Z. Wu, *J. Mater. Chem. A*, 2018, **6**, 2877-2894.
20. F. Li, M. J. Cabral, B. Xu, Z. Cheng, E. C. Dickey, J. M. LeBeau, J. Wang, J. Luo, S. Taylor, W. Hackenberger, L. Bellaiche, Z. Xu, L. Q. Chen, T. R. Shrout and S. Zhang, *Science*, 2019, **364**, 264-268.
21. T. Asano, A. Sakai, S. Ouchi, M. Sakaida, A. Miyazaki and S. Hasegawa, *Adv. Mater.*, 2018, **30**, 1803075.
22. S. Wang, Q. Bai, A. M. Nolan, Y. Liu, S. Gong, Q. Sun and Y. Mo, *Angew. Chem. Int. Ed. Engl.*, 2019, **58**, 8039-8043.
23. B. Arun, V. R. Akshay, G. R. Mutta, C. Venkatesh and M. Vasundhara, *Mater. Res. Bull*, 2017, **94**, 537-543.
24. Y. Cao, S. Cao, W. Ren, Z. Feng, S. Yuan, B. Kang, B. Lu and J. Zhang, *Appl. Phys. Lett.*, 2014, **104**, 232405.
25. X. Chen, J. Song, X. Chen and H. Yang, *Chem. Soc. Rev.*, 2019, **48**, 3073-3101.
26. S. Khalfin and Y. Bekenstein, *Nanoscale*, 2019, **11**, 8665-8679.
27. N. Phung and A. Abate, *Small*, 2018, **14**, e1802573.
28. J. Bian, Z. Li, N. Li and C. Sun, *Inorg. Chem.*, 2019, **58**, 8208-8214.
29. Z. Wang, Z. Shi, T. Li, Y. Chen and W. Huang, *Angew. Chem. Int. Ed. Engl.*, 2017, **56**, 1190-1212.
30. K. Huang, L. Yuan and S. Feng, *Inorg. Chem. Front.*, 2015, **2**, 965-981.
31. X. Wang, T. Hisatomi, Z. Wang, J. Song, J. Qu, T. Takata and K. Domen, *Angew. Chem. Int. Ed. Engl.*, 2019, **58**, 10666-10670.
32. T. J. Milstein, K. T. Kluherz, D. M. Kroupa, C. S. Erickson, J. J. De Yoreo and D. R. Gamelin, *Nano Lett.*, 2019, **19**, 1931-1937.
33. R. RameshKumar, T. Ramachandran, K. Natarajan, M. Muralidharan, F. Hamed and V. Kurapati, *J. Electron. Mater.*, 2019, **48**, 1694-1703.
34. A. Annadi, G. Cheng, H. Lee, J. W. Lee, S. Lu, A. Tylan-Tyler, M. Briggeman, M. Tomczyk, M. Huang, D. Pekker, C. B. Eom, P. Irvin and J. Levy, *Nano Lett.*, 2018, **18**, 4473-4481.
35. C. F. Pena, M. E. Soffner, A. M. Mansanares, J. A. Sampaio, F. C. G. Gandra, E. C. da Silva and H. Vargas, *Phys. B*, 2017, **523**, 39-44.
36. G. Pan, X. Bai, D. Yang, X. Chen, P. Jing, S. Qu, L. Zhang, D. Zhou, J. Zhu, W. Xu, B. Dong and H. Song, *Nano Lett.*, 2017, **17**, 8005-8011.
37. L. Yang, D.-Y. Zheng, K.-X. Guo, W.-N. Zhao, Z.-H. Peng, G.-G. Peng and T. Zhou, *J. Mater. Sci. Mater. Electron.*, 2018, **29**, 18011-18019.
38. M. A. Shahzad, M. Shahid, I. Bibi, M. A. Khan, M. A. Nawaz, M. F. A. Aboud, M. Asghar, R. N. Paracha and M. F. Warsi, *Ceram. Int.*, 2017, **43**, 1073-1079.
39. Z. Yi, N. H. Ladi, X. Shai, H. Li, Y. Shen and M. Wang, *Nanoscale Adv.*, 2019, **1**, 1276-1289.
40. M. D. Smith, B. A. Connor and H. I. Karunadasa, *Chem. Rev.*, 2019, **119**, 3104-3139.
41. D. Chen and X. Chen, *J. Mater. Chem. C*, 2019, **7**, 1413-1446.
42. Q. Fan, G. V. Biesold-McGee, Q. Xu, S. Pan, J. Peng, J. Ma and Z. Lin, *Angew. Chem. Int. Ed. Engl.*, 2019, DOI: 10.1002/anie.201904862.
43. W. Xiang, Z. Wang, D. J. Kubicki, W. Tress, J. Luo, D. Prochowicz, S. Akin, L. Emsley, J. Zhou, G. Dietler, M. Grätzel and A. Hagfeldt, *Joule*, 2019, **3**, 205-214.
44. X. Qin, X. W. Liu, W. Huang, M. Bettinelli and X. G. Liu, *Chem. Rev.*, 2017, **117**, 4488-4527.
45. R. Rajeswari, N. Islavath, M. Raghavender and L. Giribabu, *Chem. Rec.*, 2019, **19**, 1-25.
46. F. Li, D. Lin, Z. Chen, Z. Cheng, J. Wang, C. Li, Z. Xu, Q. Huang, X. Liao, L. Q. Chen, T. R. Shrout and S. Zhang, *Nat. Mater.*, 2018, **17**, 349-354.
47. A. Fuertes, *Mater. Horiz.*, 2015, **2**, 453-461.
48. L. Wang, K. A. Stoerzinger, L. Chang, J. Zhao, Y. Li, C. S. Tang, X. Yin, M. E. Bowden, Z. Yang, H. Guo, L. You, R. Guo, J. Wang, K. Ibrahim, J. Chen, A. Rusydi, J. Wang, S. A. Chambers and Y. Du, *Adv. Funct. Mater.*, 2018, **28**, 1803712.
49. Q. Sun, Z. Wang, D. Wang, Z. Hong, M. Zhou and X. Li, *Catal. Sci. Technol.*, 2018, **8**, 4563-4575.
50. Flemings and M. C., *Annu. Rev. Mater. Sci.*, 1999, **29**, 1-23.
51. C. Shi, C.-H. Yu and W. Zhang, *Angew. Chem. Int. Ed.*, 2016, **55**, 5798-5802.
52. W. Travis, E. N. K. Glover, H. Bronstein, D. O. Scanlon and R. G. Palgrave, *Chemical science*, 2016, **7**, 4548-4556.
53. C. J. Bartel, C. Sutton, B. R. Goldsmith, R. Ouyang, C. B. Musgrave, L. M. Ghiringhelli and M. Scheffler, *Sci. Adv.*, 2019, **5**, eaav0693.
54. D. H. Ji, S. L. Wang, X. Z. Ge, Q. Q. Zhang, C. M. Zhang, Z. W. Zeng and Y. Bai, *PCCP*, 2017, **19**, 17121-17127.
55. S. P. Jiang, *Int. J. Hydrogen Energy*, 2019, **44**, 7448-7493.
56. M. Askerka, Z. Li, M. Lempen, Y. Liu, A. Johnston, M. I. Saidaminov, Z. Zajacz and E. H. Sargent, *J. Am. Chem. Soc.*, 2019, **141**, 3682-3690.
57. P. K. Todd and J. R. Neilson, *J. Am. Chem. Soc.*, 2019, **141**, 1191-1195.
58. H. Lin, C. Zhou, Y. Tian, T. Siegrist and B. Ma, *ACS Energy Lett.*, 2018, **3**, 54-62.

59. F. A. Roghabadi, M. Alidaei, S. M. Mousavi, T. Ashjari, A. S. Tehrani, V. Ahmadi and S. M. Sadrameli, *J. Mater. Chem. A*, 2019, **7**, 5898-5933.
60. L. Etgar, *Energy Environ. Sci.*, 2018, **11**, 234-242.
61. Y. Chen, Y. Sun, J. Peng, J. Tang, K. Zheng and Z. Liang, *Adv. Mater.*, 2018, **30**, 1703487.
62. G. Grancini and M. K. Nazeeruddin, *Nat. Rev. Mater.*, 2019, **4**, 4-22.
63. Z. Shen, B. Qiao, Z. Xu, D. Song, D. Gao, P. Song, J. Cao, Q. Bai, Y. Wu and S. Zhao, *Nanoscale*, 2019, **11**, 4008-4014.
64. F. U. Kosasih and C. Ducati, *ChemSusChem*, 2018, **11**, 4193-4202.
65. Y. Zhu, W. Zhou and Z. Shao, *Small*, 2017, **13**, 1603793.
66. C. Moure and O. Peña, *Prog. Solid State Chem.*, 2015, **43**, 123-148.
67. Z. Xiao, Z. Song and Y. Yan, *Adv. Mater.*, 2019, DOI: 10.1002/adma.201803792, e1803792.
68. A. Hossain, P. Bandyopadhyay and S. Roy, *J. Alloys Compd.*, 2018, **740**, 414-427.
69. A. E. Maughan, A. M. Ganose, M. M. Bordelon, E. M. Miller, D. O. Scanlon and J. R. Neilson, *J. Am. Chem. Soc.*, 2016, **138**, 8453-8464.
70. T. Tiittanen, S. Vasala and M. Karppinen, *Chem. Commun. (Cambridge, U. K.)*, 2019, **55**, 1722-1725.
71. X. Zhang, L. Li, Z. Sun and J. Luo, *Chem. Soc. Rev.*, 2019, **48**, 517-539.
72. X. Liu, D. Yu, X. Song and H. Zeng, *Small*, 2018, **14**, e1801460.
73. N. Das, M. A. Nath, G. S. Thakur, M. Thirumal and A. K. Ganguli, *J. Solid State Chem.*, 2015, **229**, 97-102.
74. F. Igbari, Z. K. Wang and L. S. Liao, *Adv. Energy Mater.*, 2019, **9**, 1803150.
75. Y. Mahor, W. J. Mir and A. Nag, *J. Phys. Chem. C*, 2019, **123**, 15787-15793.
76. J. Bak, H. Bin Bae and S. Y. Chung, *Nat. Commun.*, 2019, **10**, 2713.
77. C. Berger, E. Bucher, A. Windischbacher, A. D. Boese and W. Sitte, *J. Solid State Chem.*, 2018, **259**, 57-66.
78. G. Song, Y. Chen, G. Li and B. Gao, *RSC Adv.*, 2019, **9**, 2143-2151.
79. B. Walker, G. H. Kim and J. Y. Kim, *Adv. Mater.*, 2019, **31**, 1807029.
80. X. Wu, H. Li, K. Wang, X. Sun and L. Wang, *RSC Adv.*, 2018, **8**, 11095-11101.
81. N. Chen, T. Cai, W. Li, K. Hills-Kimball, H. Yang, M. Que, Y. Nagaoka, Z. Liu, D. Yang, A. Dong, C. Y. Xu, R. Zia and O. Chen, *ACS Appl. Mater. Interfaces*, 2019, **11**, 16855-16863.
82. W. Lee, S. Hong and S. Kim, *J. Phys. Chem. C*, 2019, **123**, 2665-2672.
83. M. Pazoki, A. Röckert, M. J. Wolf, R. Imani, T. Edvinsson and J. Kullgren, *J. Mater. Chem. A*, 2017, **5**, 23131-23138.
84. J. Pejchal, J. Barta, T. Trojek, R. Kucerkova, A. Beitlerova and M. Nikl, *Radiat. Meas.*, 2019, **121**, 26-31.
85. X. Liu, H. Gong, T. Wang, H. Guo, L. Song, W. Xia, B. Gao, Z. Jiang, L. Feng and J. He, *Chem. Asian. J.*, 2018, **13**, 528-535.
86. Z. Zhang, D. Schwanz, B. Narayanan, M. Kotiuga, J. A. Dura, M. Cherukara, H. Zhou, J. W. Freeland, J. Li, R. Sutarto, F. He, C. Wu, J. Zhu, Y. Sun, K. Ramadoss, S. S. Nonnenmann, N. Yu, R. Comin, K. M. Rabe, S. Sankaranarayanan and S. Ramanathan, *Nature*, 2018, **553**, 68-72.
87. P. Yang, B. Tai, W. Wu, J. M. Zhang, F. Wang, S. Guan, W. Guo, Y. Lu and S. A. Yang, *Phys. Chem. Chem. Phys.*, 2017, **19**, 16189-16197.
88. J. Wu, K. Fujii, M. Yashima, A. Staykov, T. Akbay, T. Ishihara and J. A. Kilner, *J. Mater. Chem. A*, 2018, **6**, 11819-11829.
89. D. Guan, J. Zhou, Y. C. Huang, C. L. Dong, J. Q. Wang, W. Zhou and Z. Shao, *Nat. Commun.*, 2019, **10**, 3755.
90. D. Zhou, D. Liu, G. Pan, X. Chen, D. Li, W. Xu, X. Bai and H. Song, *Adv. Mater.*, 2017, **29**, 1704149.
91. R. Wang, M. Mujahid, Y. Duan, Z.-K. Wang, J. Xue and Y. Yang, *Adv. Funct. Mater.*, 2019, DOI: 10.1002/adfm.201808843.
92. A. Bala and V. Kumar, *J. Phys. Chem. C*, 2019, **123**, 6965-6969.
93. Y. Qiao, S. Li, W. Liu, M. Ran, H. Lu and Y. Yang, *Nanomaterials (Basel, Switzerland)*, 2018, **8**, 43.
94. K. Han, B. Yang, F. Hong, J. Chen, Y. Tang, L. Yang, Y. Sang, X. Xia, J. Guo, H. He, S. Yang and W. Deng, *Angew. Chem. Int. Ed. Engl.*, 2018, **58**, 2278-2283.
95. Y. Wu, X. M. Li and H. B. Zeng, *ACS Energy Lett.*, 2019, **4**, 673-681.
96. H. Dong, L.-D. Sun and C.-H. Yan, *Chem. Soc. Rev.*, 2015, **44**, 1608-1634.
97. L. Zhou, T. Liu, J. Zheng, K. Yu, F. Yang, N. Wang, Y. Zuo, Z. Liu, C. Xue, C. Li, B. Cheng and Q. Wang, *J. Phys. Chem. C*, 2018, **122**, 26825-26834.
98. G. Pan, X. Bai, W. Xu, X. Chen, D. Zhou, J. Zhu, H. Shao, Y. Zhai, B. Dong, L. Xu and H. Song, *ACS Appl. Mater. Interfaces*, 2018, **10**, 39040-39048.
99. P. J. Deren and K. Lemanski, *J. Lumin.*, 2014, **154**, 62-67.
100. K. V. Dabre and S. J. Dhoble, *J. Lumin.*, 2014, **150**, 55-58.
101. A. A. Kumar, J. Singh, D. S. Rajput, A. Placke, A. Kumar and J. Kumar, *Mater. Sci. Semicond. Process.*, 2018, **83**, 83-88.
102. K. Ueda, T. Aoki, Y. Shimizu, F. Massuyeau and S. Jobic, *Inorg. Chem.*, 2018, **57**, 8718-8721.
103. N. Ding, Q. Liu, L. Wang, L. Zhang, Y. Feng and Q. Zhang, *J. Mater. Sci. Mater. Electron.*, 2018, **29**, 4122-4127.
104. C. Balamurugan, S. J. Song and D. W. Lee, *Sens. Actuators, B*, 2018, **272**, 400-414.
105. R. B. Macedo Filho, A. Pedro Ayala and C. William de Araujo Paschoal, *Appl. Phys. Lett.*, 2013, **102**, 192902.
106. Z. Zhou, L. Guo, H. Yang, Q. Liu and F. Ye, *J. Alloys Compd.*, 2014, **583**, 21-31.
107. J. Kang, Y. Yang, X. Qian, K. Xu, X. Cui, Y. Fang, V. Chandragiri, B. Kang, B. Chen, A. Stroppa, S. Cao, J. Zhang and W. Ren, *Iucrj*, 2017, **4**, 598-603.
108. Z. Wang, R. Gao, X. Deng, G. Chen, W. Cai and C. Fu, *Ceram. Int.*, 2019, **45**, 1825-1830.
109. P. Garcia-Munoz, C. Lefevre, D. Robert and N. Keller, *Appl. Catal., B*, 2019, **248**, 120-128.

110. Y. Huang, J. Liu, D. Cao, Z. Liu, K. Ren, K. Liu, A. Tang, Z. Wang, L. Li, S. Qu and Z. Wang, *Int. J. Hydrogen Energy*, 2019, **44**, 13242-13252.
111. B. Kucharczyk, J. Okal, W. Tylus, J. Winiarski and B. Szczygieł, *Ceram. Int.*, 2019, **45**, 2779-2788.
112. J. Bian, R. Su, Y. Yao, J. Wang, J. Zhou, F. Li, Z. L. Wang and C. Sun, *ACS Appl. Energy Mater.*, 2019, **2**, 923-931.
113. B. M. Pirzada, Pushpendra, R. K. Kunchala and B. S. Naidu, *ACS Omega*, 2019, **4**, 2618-2629.
114. S. Liang, T. Xu, F. Teng, R. Zong and Y. Zhu, *Appl. Catal., B*, 2010, **96**, 267-275.
115. X. Li, Y. Yin, C. Yao, S. Zuo, X. Lu, S. Luo and C. Ni, *Particuology*, 2016, **26**, 66-72.
116. K. Kamonsuangkasem, S. Therdthianwong, A. Therdthianwong and N. Thammajak, *Appl. Catal., B*, 2017, **218**, 650-663.
117. O. Pavlovska, I. Lutsyuk, A. Kondyr, Y. Zhydachevskyy, Y. Vakhula, A. Pieniążek and L. Vasylechko, *Acta Phys. Pol., A*, 2018, **133**, 802-805.
118. F. A. Rabuffetti and R. L. Brutchey, *Dalton Trans.*, 2014, **43**, 14499-14513.
119. Q. Choudhry, M. A. Khan, G. Nasar, A. Mahmood, M. Shahid, I. Shakir and M. F. Warsi, *J. Magn. Magn. Mater.*, 2015, **393**, 67-72.
120. X. Liu, C.-H. Yan and J. A. Capobianco, *Chem. Soc. Rev.*, 2015, **44**, 1299-1301.
121. K. Lemański, B. Bondzior, D. Szymański and P. J. Dereń, *New J. Chem.*, 2019, **43**, 6242-6248.
122. P. Niu, X. Liu, Z. Xie and W. Zhao, *J. Lumin.*, 2018, **198**, 34-39.
123. J. Duan, Y. Zhao, X. Yang, Y. Wang, B. He and Q. Tang, *Adv. Energy Mater.*, 2018, **8**, 1802346.
124. B. Yang, Y. Wang, T. Wei, Y. Pan, E. Zhou, Z. Yuan, Y. Han, M. Li, X. Ling, L. Yin, X. Xie and L. Huang, *Adv. Funct. Mater.*, 2018, **28**, 1801782.
125. J. Wu, D. Xiao and J. Zhu, *Chem. Rev.*, 2015, **115**, 2559-2595.
126. W. Lv, L. Li, M. Xu, J. Hong, X. Tang, L. Xu, Y. Wu, R. Zhu, R. Chen and W. Huang, *Adv. Mater.*, 2019, **31**, 1900682.
127. H. Wang, J. Wang, Y. Pi, Q. Shao, Y. Tan and X. Huang, *Angew. Chem. Int. Ed. Engl.*, 2019, **58**, 2316-2320.
128. X. Sheng, Y. Liu, Y. Wang, Y. Li, X. Wang, X. Wang, Z. Dai, J. Bao and X. Xu, *Adv. Mater.*, 2017, **29**, 1700150.
129. E. Cao, A. Wu, H. Wang, Y. Zhang, W. Hao and L. Sun, *ACS Appl. Nano Mater.*, 2019, **2**, 1541-1551.
130. L. Casillas-Trujillo, D. A. Andersson, B. Dorado, M. Nikl, K. E. Sickafus, K. J. McClellan and C. R. Stanek, *Phys. Status Solidi B*, 2014, **251**, 2279-2286.
131. C. S. Lewis, H. Liu, J. Han, L. Wang, S. Yue, N. A. Brennan and S. S. Wong, *Nanoscale*, 2016, **8**, 2129-2142.
132. D. J. Daniel, O. Annalakshmi, U. Madhusoodanan and P. Ramasamy, *J. Rare Earths*, 2014, **32**, 496-500.
133. B. J. Moon, S. J. Kim, S. Lee, A. Lee, H. Lee, D. S. Lee, T. W. Kim, S. K. Lee, S. Bae and S. H. Lee, *Adv. Mater.*, 2019, **31**, e1901716.
134. H. Zhong, J. Wang, K. An, K. Fang and Y. Liu, *Catal. Sci. Technol.*, 2019, **9**, 3454-3468.
135. K. Guo, R. Zhang, T. He, H. Kong and C. Deng, *J. Rare Earths*, 2016, **34**, 1228-1234.
136. H. Shi, X. Li, J. Xia, X. Lu, S. Zuo, S. Luo and C. Yao, *J. Inorg. Organomet. Polym. Mater.*, 2017, **27**, S166-S172.
137. A. Heuer-Jungemann, N. Feliu, I. Bakaimi, M. Hamaly, A. Alkilany, I. Chakraborty, A. Masood, M. F. Casula, A. Kostopoulou, E. Oh, K. Susumu, M. H. Stewart, I. L. Medintz, E. Stratakis, W. J. Parak and A. G. Kanaras, *Chem. Rev.*, 2019, **119**, 4819-4880.
138. Y. Zhou, J. Chen, O. M. Bakr and H.-T. Sun, *Chem. Mater.*, 2018, **30**, 6589-6613.
139. D. Preziosi, L. Lopez-Mir, X. Li, T. Cornelissen, J. H. Lee, F. Trier, K. Bouzehouane, S. Valencia, A. Gloter, A. Barthelemy and M. Bibes, *Nano Lett.*, 2018, **18**, 2226-2232.
140. P. Shikha, T. S. Kang and B. S. Randhawa, *J. Alloys Compd.*, 2015, **625**, 336-345.
141. J. M. Hodges, J. R. Morse, J. L. Fenton, J. D. Ackerman, L. T. Alameda and R. E. Schaak, *Chem. Mater.*, 2017, **29**, 106-119.
142. M. Afqir, M. Elaatmani, A. Zegzouti, A. Oufakir and M. Daoud, *J. Mater. Sci. Mater. Electron.*, 2019, **30**, 5495-5502.
143. P. Rawat, S. K. Saroj, M. Gupta, G. V. Prakash and R. Nagarajan, *J. Fluorine Chem.*, 2017, **200**, 1-7.
144. Y. Tao, L. Wu, X. Zhao, X. Chen, R. Li, M. Chen, D. Zhang, G. Li and H. Li, *ACS Appl. Mater. Interfaces*, 2019, **11**, 25967-25975.
145. W. Li, S. Wang and J. Li, *Chem. Asian. J.*, 2019, **14**, 2815-2821.
146. M. Imran, V. Caligiuri, M. Wang, L. Goldoni, M. Prato, R. Krahne, L. De Trizio and L. Manna, *J. Am. Chem. Soc.*, 2018, **140**, 2656-2664.
147. S. E. Creutz, E. N. Crites, M. C. De Siena and D. R. Gamelin, *Chem. Mater.*, 2018, **30**, 4887-4891.
148. X. Li, Y. Wu, S. Zhang, B. Cai, Y. Gu, J. Song and H. Zeng, *Adv. Funct. Mater.*, 2016, **26**, 2435-2445.
149. Y.-P. Du, Y.-W. Zhang, Z.-G. Yan, L.-D. Sun, S. Gao and C.-H. Yan, *Chem. Asian. J.*, 2007, **2**, 965-974.
150. Z. Quan, P. Yang, C. Li, J. Yang, D. Yang, Y. Jin, H. Lian, H. Li and J. Lin, *J. Phys. Chem. C*, 2009, **113**, 4018-4025.
151. J. E. Roberts, *J. Am. Chem. Soc.*, 1961, **83**, 1087-1088.
152. S. Shi, L. D. Sun, Y. X. Xue, H. Dong, K. Wu, S. C. Guo, B. T. Wu and C. H. Yan, *Nano Lett.*, 2018, **18**, 2964-2969.
153. J. Zhang, Y. Yang, H. Deng, U. Farooq, X. Yang, J. Khan, J. Tang and H. Song, *ACS nano*, 2017, **11**, 9294-9302.
154. Q. S. Hu, Z. Li, Z. F. Tan, H. B. Song, C. Ge, G. D. Niu, J. T. Han and J. Tang, *Adv. Opt. Mater.*, 2018, **6**, 1700864.
155. B. Yang, J. Chen, F. Hong, X. Mao, K. Zheng, S. Yang, Y. Li, T. Pullerits, W. Deng and K. Han, *Angew. Chem. Int. Ed.*, 2017, **56**, 12471-12475.
156. X. Yi, R. Li, H. Zhu, J. Gao, W. You, Z. Gong, W. Guo and X. Chen, *J. Mater. Chem. C*, 2018, **6**, 2069-2076.
157. E. Devi, B. J. Kalaiselvi, K. Madhan, D. Vanidha, S. S. Meena and R. Kannan, *J. Appl. Phys.*, 2018, **124**, 084102.
158. S.-X. Chen, Y. Wang, A.-P. Jia, H.-H. Liu, M.-F. Luo and J.-Q. Lu, *Appl. Surf. Sci.*, 2014, **307**, 178-188.
159. S. Manzoor and S. Husain, *J. Appl. Phys.*, 2018, **124**, 065110.
160. J. Li, R. Hu, J. Zhang, W. Meng, Y. Du, Y. Si and Z. Zhang, *Fuel*, 2016, **178**, 148-154.
161. M. Rakibuddin, H. Kim and M. E. Khan, *Appl. Surf. Sci.*, 2018, **452**, 400-412.
162. M. A. Gomes, A. S. Lima, K. I. B. Eguiluz and G. R. Salazar-Banda, *J. Mater. Sci.*, 2016, **51**, 4709-4727.

163. S. K. Saroj, P. Rawat, M. Gupta, G. V. Prakash and R. Nagarajan, *Eur. J. Inorg. Chem.*, 2018, DOI: 10.1002/ejic.201801123, 4826-4833.

164. D. Chen, G. Fang, X. Chen, L. Lei, J. Zhong, Q. Mao, S. Zhou and J. Li, *J. Mater. Chem. C*, 2018, **6**, 8990-8998.

165. K. Di, X. Li, X. Jing, S. Yao and J. Yan, *J. Alloys Compd.*, 2016, **661**, 435-440.

166. G. Wang, P. Wang, H.-K. Luo and T. S. A. Hor, *Chem. Asian. J.*, 2014, **9**, 1854-1859.

167. O. B. Pavlovska, L. O. Vasylechko, I. V. Lutsyuk, N. M. Koval, Y. A. Zhydachevskii and A. Pieniazek, *Nanoscale Res. Lett.*, 2017, **12**, 153.

168. N. Tsvetkov, Q. Lu, L. Sun, E. J. Crumlin and B. Yildiz, *Nat. Mater.*, 2016, **15**, 1010-1016.

169. T. Katayama, A. Chikamatsu, Y. Hirose, M. Minohara, H. Kumigashira, I. Harayama, D. Sekiba and T. Hasegawa, *J. Mater. Chem. C*, 2018, **6**, 3445-3450.

170. L. Chang, L. Wang, L. You, Z. Yang, A. Abdelsamie, Q. Zhang, Y. Zhou, L. Gu, S. A. Chambers and J. Wang, *ACS Appl. Mater. Interfaces*, 2019, **11**, 16191-16197.

171. J. Hwang, Z. Feng, N. Charles, X. R. Wang, D. Lee, K. A. Stoerzinger, S. Muy, R. R. Rao, D. Lee, R. Jacobs, D. Morgan and Y. Shao-Horn, *Mater. Today*, 2019, DOI: 10.1016/j.mattod.2019.03.014.

172. H. Han, D. Kim, S. Chae, J. Park, S. Y. Nam, M. Choi, K. Yong, H. J. Kim, J. Son and H. M. Jang, *Nanoscale*, 2018, **10**, 13261-13269.

173. L. Huang, Q. Gao, L. D. Sun, H. Dong, S. Shi, T. Cai, Q. Liao and C. H. Yan, *Adv. Mater.*, 2018, **30**, e1800596.

174. Y. Zhu, W. Zhou, Y. Zhong, Y. Bu, X. Chen, Q. Zhong, M. Liu and Z. Shao, *Adv. Energy Mater.*, 2017, **7**, 1602122.

175. X. Zhang, Y. Gong, S. Li and C. Sun, *ACS Catal.*, 2017, **7**, 7737-7747.

176. W. Zhang, H. Wang, K. Guan, Z. Wei, X. Zhang, J. Meng, X. Liu and J. Meng, *ACS Appl. Mater. Interfaces*, 2019, **11**, 26830-26841.

177. E. Bi, H. Chen, F. Xie, Y. Wu, W. Chen, Y. Su, A. Islam, M. Gratzel, X. Yang and L. Han, *Nat. Commun.*, 2017, **8**, 15330.

178. A. K. Jena, A. Kulkarni, Y. Sanehira, M. Ikegami and T. Miyasaka, *Chem. Mater.*, 2018, **30**, 6668-6674.

179. G. E. Eperon, G. M. Paternò, R. J. Sutton, A. Zampetti, A. A. Haghighirad, F. Cacialli and H. J. Snaith, *J. Mater. Chem. A*, 2015, **3**, 19688-19695.

180. M. Kulbak, D. Cahen and G. Hodes, *J. Phys. Chem. Lett.*, 2015, **6**, 2452-2456.

181. R. E. Beal, D. J. Slotcavage, T. Leijtens, A. R. Bowring, R. A. Belisle, W. H. Nguyen, G. F. Burkhard, E. T. Hoke and M. D. McGehee, *J. Phys. Chem. Lett.*, 2016, **7**, 746-751.

182. K. Wang, L. Zheng, T. Zhu, X. Yao, C. Yi, X. Zhang, Y. Cao, L. Liu, W. Hu and X. Gong, *Nano Energy*, 2019, **61**, 352-360.

183. Y. Xiang, Z. Ma, J. Zhuang, H. Lu, C. Jia, J. Luo, H. Li and X. Cheng, *J. Phys. Chem. C*, 2017, **121**, 20150-20157.

184. R. Meng, X. Feng, Y. Yang, X. Lv, J. Cao and Y. Tang, *ACS Appl. Mater. Interfaces*, 2019, **11**, 13273-13278.

185. P. Song, P. Zhu and C. Zhang, *J. Alloys Compd.*, 2018, **731**, 1009-1013.

186. L. Zhang, L. Dong, B. Shao, S. Zhao and H. You, *Dalton Trans.*, 2019, **48**, 11460-11468.

187. Z. Sun, C. Ma, M. Liu, J. Cui, L. Lu, J. Lu, X. Lou, L. Jin, H. Wang and C. L. Jia, *Adv. Mater.*, 2017, **29**, 1604427.

188. G. Wang, J. L. Li, X. Zhang, Z. M. Fan, F. Yang, A. Feteira, D. Zhou, D. C. Sinclair, T. Ma, X. L. Tan, D. W. Wang and I. M. Reaney, *Energy Environ. Sci.*, 2019, **12**, 582-588.

189. X. Hao, Y. Wang, L. Zhang, L. Zhang and S. An, *Appl. Phys. Lett.*, 2013, **102**, 163903.

190. Chitra and K. C. Singh, *J. Mater. Sci. Mater. Electron.*, 2018, **29**, 17630-17637.

191. F. Kousar, S. Nazim, M. F. Warsi, M. A. Khan, M. N. Ashiq, Z. A. Gilani, I. Shakir and A. Wadood, *J. Alloys Compd.*, 2015, **629**, 315-318.

192. T.-X. Zhao, J.-H. Qiu, M.-G. Ma, Z.-H. Chen, C.-B. Li and X.-G. Jia, *J. Nanosci. Nanotechnol.*, 2019, **19**, 5661-5666.

193. Z.-h. Chen, Z.-w. Li, J.-h. Qiu, T.-x. Zhao, K.-q. Zhu, J.-n. Ding, W.-q. Zhu and J.-j. Xu, *Phys. Status Solidi A*, 2018, **215**, 1700417.

194. M. Chen, Z. Xu, R. Chu, Z. Wang, S. Gao, G. Yu, W. Li, S. Gong and G. Li, *Mater. Res. Bull.*, 2014, **59**, 305-310.

195. M. Kroutvar, Y. Ducommun, D. Heiss, M. Bichler, D. Schuh, G. Abstreiter and J. J. Finley, *Nature*, 2004, **432**, 81-84.

196. W. Wu, M. Chen, Y. Ding and C. Liu, *J. Alloys Compd.*, 2014, **588**, 496-501.

197. S. Zhang, F. Li, X. Jiang, J. Kim, J. Luo and X. Geng, *Prog. Mater. Sci.*, 2015, **68**, 1-66.

198. J. Roedel, W. Jo, K. T. P. Seifert, E.-M. Anton, T. Granzow and D. Damjanovic, *J. Am. Ceram. Soc.*, 2009, **92**, 1153-1177.

199. K. Guo, Q. Mou, T. He, H. Kong and R. Zhang, *J. Mater. Sci.: Mater. Electron.*, 2016, **28**, 1971-1975.

200. A. Pelaiz-Barranco, J. D. S. Guerra, F. Calderon-Pinar, C. Arago, O. Garcia-Zaldivar, R. Lopez-Noda, J. A. Gonzalo and J. A. Eiras, *J. Mater. Sci.*, 2009, **44**, 204-211.

201. X. Xiao, M. Widenmeyer, W. Xie, T. Zou, S. Yoon, M. Scavini, S. Checchia, Z. Zhong, P. Hansmann, S. Kilper, A. Kovalevsky and A. Weidenkaff, *PCCP*, 2017, **19**, 13469-13480.

202. P. Kaya, G. Gregori, F. Baiutti, P. Yordanov, Y. E. Suyolcu, G. Cristiani, F. Wrobel, E. Benckiser, B. Keimer, P. A. van Aken, H. U. Habermeier, G. Logvenov and J. Maier, *ACS Appl. Mater. Interfaces*, 2018, **10**, 22786-22792.

203. Y. Kinemuchi, K.-i. Mimura and K. Kato, *J. Electron. Mater.*, 2015, **44**, 1773-1776.

204. T. Reimann and J. Toepfer, *J. Alloys Compd.*, 2017, **699**, 788-795.

205. Y. Kinemuchi, K.-i. Mimura, A. Towata and K. Kato, *J. Electron. Mater.*, 2014, **43**, 2011-2016.

206. A. Rai and A. K. Thakur, *J. Alloys Compd.*, 2017, **695**, 3579-3588.

207. H. H. Kumar, C. M. Lonkar and K. Balasubramanian, *Appl. Phys. A*, 2017, **123**, 615.

208. A. Kumar, V. V. B. Prasad, K. C. J. Raju and A. R. James, *J. Alloys Compd.*, 2016, **654**, 95-102.

209. A. Mahmood, M. F. Warsi, M. N. Ashiq and M. Ishaq, *J. Magn. Magn. Mater.*, 2013, **327**, 64-70.

210. S. Das, R. C. Sahoo, K. P. Bera and T. K. Nath, *J. Magn. Magn. Mater.*, 2018, **451**, 226-234.

211. R. Jana, V. Pareek, P. Khatua, P. Saha, A. Chandra and G. D. Mukherjee, *J. Phys.: Condens. Matter*, 2018, **30**, 335401.

212. M. Azhar Khan, K. Khan, A. Mahmood, G. Murtaza, M. N. Akhtar, I. Ali, M. Shahid, I. Shakir and M. Farooq Warsi, *Ceram. Int.*, 2014, **40**, 13211-13216.
213. A. Aziz, E. Ahmed, M. N. Ashiq, M. A. Khan, N. Karamat and I. Ali, *Prog. Nat. Sci.: Mater. Int.*, 2016, **26**, 325-333.
214. A. Bahari, A. Ramzannezhad, D. Shajari and H. Najafi, *Int. J. Mod. Phys. B*, 2017, **31**, 1750015.
215. A. Aziz, E. Ahmed, I. Ali, M. Athar, M. F. Ehsan and M. N. Ashiq, *J. Electron. Mater.*, 2015, **44**, 4300-4307.
216. S. Dutta, A. Antony Jeyaseelan and S. Sruthi, *Thin Solid Films*, 2014, **562**, 190-194.
217. E. E. Ateia and F. S. Soliman, *Mater. Sci. Eng., B*, 2019, **244**, 29-37.
218. C. A. Diaz-Moreno, Y. Ding, J. Portelles, J. Heiras, A. Hurtado Macias, A. Syeed, A. Paez, C. Li, J. Lopez and R. Wicker, *Ceram. Int.*, 2018, **44**, 4727-4733.
219. X. Zhang, Y. Zhang, X. Zhang, W. Yin, Y. Wang, H. Wang, M. Lu, Z. Li, Z. Gu and W. W. Yu, *J. Mater. Chem. C*, 2018, **6**, 10101-10105.
220. G. M. Arumugam, C. Xu, S. K. Karunakaran, Z. Shi, F. Qin, C. Zhu and F. Chen, *J. Mater. Chem. C*, 2018, **6**, 12537-12546.
221. T. J. Milstein, D. M. Kroupa and D. R. Gamelin, *Nano Lett.*, 2018, **18**, 3792-3799.
222. J. Zhong, D. Chen, S. Yuan, M. Liu, Y. Yuan, Y. Zhu, X. Li and Z. Ji, *Inorg. Chem.*, 2018, **57**, 8978-8987.
223. R. T. Wegh, H. Donker, K. D. Oskam and A. Meijerink, *Science*, 1999, **283**, 663-666.
224. W. Zheng, P. Huang, Z. Gong, D. Tu, J. Xu, Q. Zou, R. Li, W. You, J.-C. G. Bünzli and X. Chen, *Nat. Commun.*, 2018, **9**, 3462.
225. J. Sang, J. Zhou, J. Zhang, H. Zhou, H. Li, Z. Ci, S. Peng and Z. Wang, *ACS Appl. Mater. Interfaces*, 2019, **11**, 20150-20156.
226. D. M. Kroupa, J. Y. Roh, T. J. Milstein, S. E. Creutz and D. R. Gamelin, *ACS Energy Lett.*, 2018, **3**, 2390-2395.
227. Y. Liu, G. Pan, R. Wang, H. Shao, H. Wang, W. Xu, H. Cui and H. Song, *Nanoscale*, 2018, **10**, 14067-14072.
228. G. M. Arumugam, C. Xu, S. K. Karunakaran, Z. Shi, C. Zhu, M. Wei and Q. Feifei, *Appl. Phys. Lett.*, 2018, **112**, 054104.
229. M. Suta, W. Urland, C. Daul and C. Wickleder, *PCCP*, 2016, **18**, 13196-13208.
230. J. Wang, F. Wang, C. Wang, Z. Liu and X. Liu, *Angew. Chem. Int. Ed.*, 2011, **50**, 10369-10372.
231. J. J. Schuyt and G. V. M. Williams, *J. Lumin.*, 2018, **204**, 472-479.
232. M. Ding, M. Xu, C. Lu, J. Xi, Z. Ji and D. Chen, *J. Alloys Compd.*, 2017, **721**, 531-537.
233. D. K. Singh and J. Manam, *J. Mater. Sci. Mater. Electron.*, 2016, **27**, 10371-10381.
234. Q. Sun, S. Wang, B. Devakumar, L. Sun, J. Liang and X. Huang, *RSC Adv.*, 2019, **9**, 3303-3310.
235. Y. Chen, D. Wang, H. Qin, H. Zhang, Z. Zhang, G. Zhou, C. Gao and J. Hu, *J. Rare Earths*, 2019, **37**, 80-87.
236. C. Wang, H. Lin, X. Xiang, Y. Cheng, Q. Huang, Y. Gao, X. Cui and Y. Wang, *J. Mater. Chem. C*, 2018, **6**, 9964-9971.
237. X. S. Niu, W. M. Du, W. P. Du and K. Jiang, *Rare Metal Mater.Engineer.*, 2005, **34**, 124-127.
238. C. R. Michel, M. A. Lopez-Alvarez, A. H. Martinez-Preciado and G. G. Carbajal-Arizaga, *J. Sens.*, 2019, DOI: 10.1155/2019/5682645.
239. C. R. Stanek, M. R. Levy, K. J. McClellan, B. P. Uberuaga and R. W. Grimes, *Phys. Status Solidi B*, 2005, **242**, R113-R115.
240. H. Wang, L. Yan, T. Nakotte, W. Xu, M. Zhou, D. Ding and H. Luo, *Inorg. Chem. Front.*, 2019, **6**, 1029-1039.
241. B. Hua, M. Li, Y.-Q. Zhang, Y.-F. Sun and J.-L. Luo, *Adv. Energy Mater.*, 2017, **7**, 1700666.
242. B. J. Kim, E. Fabbri, D. F. Abbott, X. Cheng, A. H. Clark, M. Nachtegaal, M. Borlaf, I. E. Castelli, T. Graule and T. J. Schmidt, *J. Am. Chem. Soc.*, 2019, **141**, 5231-5240.
243. M. Li, A. R. Insani, L. Zhuang, Z. Wang, A. U. Rehman, L. X. Liu and Z. Zhu, *J. Colloid Interface Sci.*, 2019, **553**, 813-819.
244. Y. Tong, Y. Guo, P. Chen, H. Liu, M. Zhang, L. Zhang, W. Yan, W. Chu, C. Wu and Y. Xie, *Chem*, 2017, **3**, 812-821.
245. A. Grimaud, K. J. May, C. E. Carlton, Y. L. Lee, M. Risch, W. T. Hong, J. Zhou and Y. Shao-Horn, *Nat. Commun.*, 2013, **4**, 2439.
246. Y. Duan, S. Sun, S. Xi, X. Ren, Y. Zhou, G. Zhang, H. Yang, Y. Du and Z. J. Xu, *Chem. Mater.*, 2017, **29**, 10534-10541.
247. S. She, J. Yu, W. Tang, Y. Zhu, Y. Chen, J. Sunarso, W. Zhou and Z. Shao, *ACS Appl. Mater. Interfaces*, 2018, **10**, 11715-11721.
248. Z. Liu, Y. Sun, X. Wu, C. Hou, Z. Geng, J. Wu, K. Huang, L. Gao and S. Feng, *CrystEngComm*, 2019, **21**, 1534-1538.
249. X. Miao, L. Wu, Y. Lin, X. Yuan, J. Zhao, W. Yan, S. Zhou and L. Shi, *Chem. Commun. (Cambridge, U. K.)*, 2019, **55**, 1442-1445.
250. L. Wang, K. A. Stoerzinger, L. Chang, X. Yin, Y. Li, C. S. Tang, E. Jia, M. E. Bowden, Z. Yang, A. Abdelsamie, L. You, R. Guo, J. Chen, A. Rusydi, J. Wang, S. A. Chambers and Y. Du, *ACS Appl. Mater. Interfaces*, 2019, **11**, 12941-12947.
251. Y. Zhu, L. Zhang, B. Zhao, H. Chen, X. Liu, R. Zhao, X. Wang, J. Liu, Y. Chen and M. Liu, *Adv. Funct. Mater.*, 2019, DOI: 10.1002/adfm.201901783, 1901783.
252. G. Chen, Y. Zhu, H. M. Chen, Z. Hu, S.-F. Hung, N. Ma, J. Dai, H.-J. Lin, C.-T. Chen, W. Zhou and Z. Shao, *Adv. Mater.*, 2019, **31**, 1900883.
253. H. Chen, X. Sun and X. Xu, *Electrochim. Acta*, 2017, **252**, 138-146.
254. G. P. Wheeler and K.-S. Choi, *ACS Energy Lett.*, 2017, **2**, 2378-2382.
255. J. Xu, C. Sun, Z. Wang, Y. Hou, Z. Ding and S. Wang, *Chemistry*, 2018, **24**, 18512-18517.
256. Z. Chen, T. Fan, Q. Zhang, J. He, H. Fan, Y. Sun, X. Yi and J. Li, *J. Colloid Interface Sci.*, 2019, **536**, 105-111.
257. Z. Chen, Q. Jiang, F. Cheng, J. Tong, M. Yang, Z. Jiang and C. Li, *J. Mater. Chem. A*, 2019, **7**, 6099-6112.
258. Y. Wang, S. Jin, G. Pan, Z. Li, L. Chen, G. Liu and X. Xu, *J. Mater. Chem. A*, 2019, **7**, 5702-5711.
259. A. Krukowska, M. J. Winiarski, J. Strychalska-Nowak, T. Klimczuk, W. Lisowski, A. Mikolajczyk, H. P. Pinto, T. Puzyn, T. Grzyb and A. Zaleska-Medynska, *Appl. Catal., B*, 2018, **224**, 451-468.
260. A. Krukowska, G. Trykowski, W. Lisowski, T. Klimczuk, M. J. Winiarski and A. Zaleska-Medynska, *J. Catal.*, 2018, **364**, 371-381.
261. Y. Absalan, I. G. Bratchikova and O. V. Kovalchukova, *J. Mol. Liq.*, 2018, **268**, 882-894.
262. M. Baladi, F. Soofivand, M. Valian and M. Salavati-Niasari, *Ultrason. Sonochem.*, 2019, **57**, 172-184.
263. Y. Soltanabadi, M. Jourshabani and Z. Shariatinia, *Sep. Purif. Technol.*, 2018, **202**, 227-241.
264. F. Lin, J. Shao, H. Tang, Y. Li, Z. Wang, G. Chen, D. Yuan and K. Cen, *Appl. Surf. Sci.*, 2019, **479**, 234-246.
265. Q. Wang and L. Ma, *New J. Chem.*, 2019, **43**, 2974-2980.
266. C. Zhou, X. Liu, C. Wu, Y. Wen, Y. Xue, R. Chen, Z. Zhang, B. Shan, H. Yin and W. G. Wang, *PCCP*, 2014, **16**, 5106-5112.

267. X. Li, C. Tang, M. Ai, L. Dong and Z. Xu, *Chem. Mater.*, 2010, **22**, 4879-4889.
268. S. Zhao, Y. Wang, L. Wang and Y. Jin, *Inorg. Chem. Front.*, 2017, **4**, 994-1002.
269. A. Garbujo, M. Pacella, M. M. Natile, M. Guiotto, J. Fabro, P. Canu and A. Glisenti, *Appl. Catal., A*, 2017, **544**, 94-107.
270. Y. Lu, K. A. Michalow, S. K. Matam, A. Winkler, A. E. Maegli, S. Yoon, A. Heel, A. Weidenkaff and D. Ferri, *Appl. Catal., B*, 2014, **144**, 631-643.
271. R. Hu, Y. Bai, H. Du, H. Zhang, Y. Du, J. Zhang and Q. Zhou, *J. Rare Earths*, 2015, **33**, 1284-1292.
272. Y. Sim, J. Yoo, J.-M. Ha and J. C. Jung, *J. Energy Chem.*, 2019, **35**, 1-8.
273. S. Wang, S. Du, W. Tang, S. Hoang, X. Lu, W. Xiao, B. Zhang, J. Weng, E. Schneer, Y. Guo, J. Ding, Z. Zhang and P.-X. Gao, *ChemCatChem*, 2018, **10**, 2184-2189.
274. M. Tang, K. Liu, D. M. Roddick and M. Fan, *J. Catal.*, 2018, **368**, 38-52.
275. T. Yabe, Y. Kamite, K. Sugiura, S. Ogo and Y. Sekine, *J. CO2 Util.*, 2017, **20**, 156-162.
276. M. Pudukudy, Z. Yaakob and M. S. Takriff, *Energy Convers. Manage.*, 2016, **126**, 302-315.
277. A. G. Dedov, A. S. Loktev, D. A. Komissarenko, K. V. Parkhomenko, A. C. Roger, O. A. Shlyakhtin, G. N. Mazo and I. I. Moiseev, *Fuel Process. Technol.*, 2016, **148**, 128-137.
278. J. Kuc, M. Neumann, M. Armbruester, S. Yoon, Y. Zhang, R. Erni, A. Weidenkaff and S. K. Matam, *Catal. Sci. Technol.*, 2016, **6**, 1455-1468.
279. K. Okura, K. Miyazaki, H. Muroyama, T. Matsui and K. Eguchi, *RSC Adv.*, 2018, **8**, 32102-32110.
280. D. Meng, H. Guo, Z. Cui, C. Ma, J. Zhao, J. Lu, H. Xu, Z. Wang, X. Hu, Z. Fu, R. Peng, J. Guo, X. Zhai, G. J. Brown, R. Knize and Y. Lu, *Proc. Natl. Acad. Sci. U. S. A.*, 2018, **115**, 2873-2877.
281. B.-X. Wang, S. Rosenkranz, X. Rui, J. Zhang, F. Ye, H. Zheng, R. F. Klie, J. F. Mitchell and D. Phelan, *Phys. Rev. Mater.*, 2018, **2**, 064404.
282. P. Veverka, O. Kaman, K. Knizek, P. Novak, M. Marysko and Z. Jirak, *J. Phys.: Condens. Matter*, 2017, **29**, 035803.
283. S. L. C. Pinho, J. S. Amaral, A. Wattiaux, M. Duttine, M.-H. Delville and C. F. G. C. Geraldes, *Eur. J. Inorg. Chem.*, 2018, **2018**, 3570-3578.
284. F. A. Rabuffetti, S. P. Culver, J. S. Lee and R. L. Brutchey, *Nanoscale*, 2014, **6**, 2909-2914.
285. R. Das and P. Poddar, *J. Phys. Chem. C*, 2014, **118**, 13268-13275.
286. M. Taheri, F. S. Razavi and R. K. Kremer, *Phys. C*, 2018, **553**, 8-12.
287. M. Arora and M. Kumar, *Ceram. Int.*, 2015, **41**, 5705-5712.
288. W.-L. Tang, H. Lin, S.-H. Yang, Y.-L. Zhang, Y.-X. Tong and S.-L. Xie, *Ferroelectrics*, 2015, **489**, 65-72.
289. K. Yoshimatsu, J. Ishimaru, K. Watarai, K. Yamamoto, Y. Hirata, H. Wadati, Y. Takeda, K. Horiba, H. Kumigashira, O. Sakata and A. Ohtomo, *Phys. Rev. B*, 2019, **99**, 235129.
290. R. Dusad, F. K. K. Kirschner, J. C. Hoke, B. R. Roberts, A. Eyal, F. Flicker, G. M. Luke, S. J. Blundell and J. C. S. Davis, *Nature*, 2019, **571**, 234-239.
291. Q. Chen, S. Fan, K. M. Taddei, M. B. Stone, A. I. Kolesnikov, J. Cheng, J. L. Musfeldt, H. Zhou and A. A. Aczel, *J. Am. Chem. Soc.*, 2019, **141**, 9928-9936.
292. E. Rozenberg, M. I. Tsindlekht, I. Felner, E. Sominski, A. Gedanken and Y. M. Mukovskii, *IEEE Trans. Magn.*, 2007, **43**, 3052-3054.
293. R. M. Khafagy and E. H. El-khawas, *J. Alloys Compd.*, 2014, **606**, 288-297.
294. X. A. Velasquez Moya, R. Cardona, J. I. Villa Hernandez, D. A. Landinez Tellez and J. Roa-Rojas, *J. Electron. Mater.*, 2018, **47**, 3421-3429.
295. J. Xiong, J. Yan, A. A. Aczel and P. M. Woodward, *J. Solid State Chem.*, 2018, **258**, 762-767.
296. Z. B. Guo, Y. W. Du, J. S. Zhu, H. Huang, W. P. Ding and D. Feng, *Phys. Rev. Lett.*, 1997, **78**, 1142-1145.
297. B. F. Yu, Q. Gao, B. Zhang, X. Z. Meng and Z. Chen, *Int. J. Refrig*, 2003, **26**, 622-636.
298. O. Tegus, E. Brück, K. H. J. Buschow and F. R. de Boer, *Nature*, 2002, **415**, 150-152.

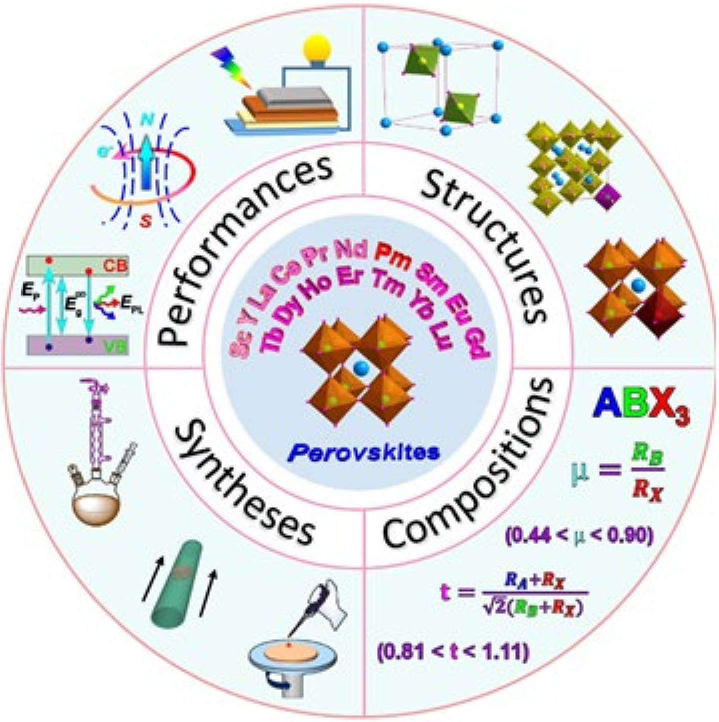

Scheme 1 Schematic illustration of the structures, compositions, synthesis and performances of RE based perovskite nanomaterials.

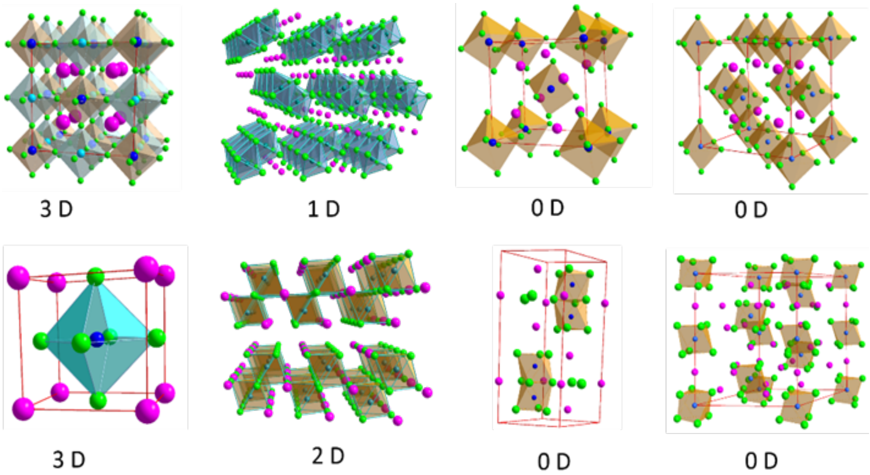

Fig. 1 The crystal structures of 3 D, 2 D, 1 D and 0 D perovskites.

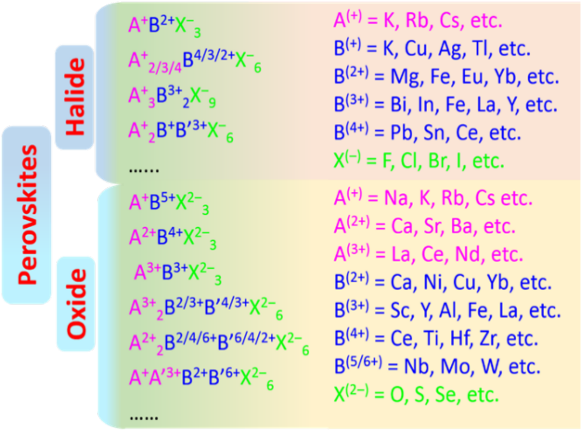

Fig. 2 The various types and and components of halide and oxide perovskites.

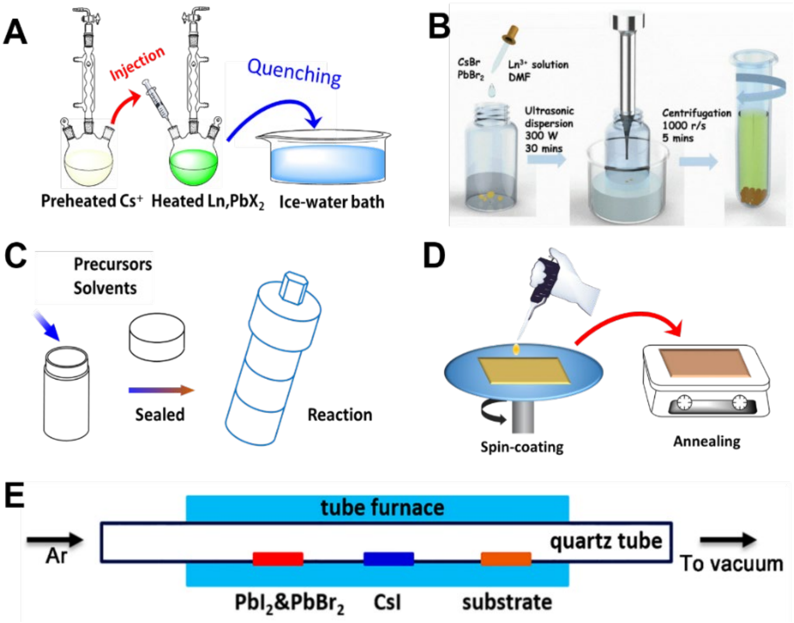

Fig. 3 The various preparation methods for PNMs preparation. (A) Hot-injection method, (B) ultrasonic co-precipitation method. Ref. 137. Copyright 2018, Wiley-VCH.(C) solvothermal method, (D) spin-coating technique, (E) chemical vapour deposition method. Ref. 138. Copyright 2018, Wiley-VCH.

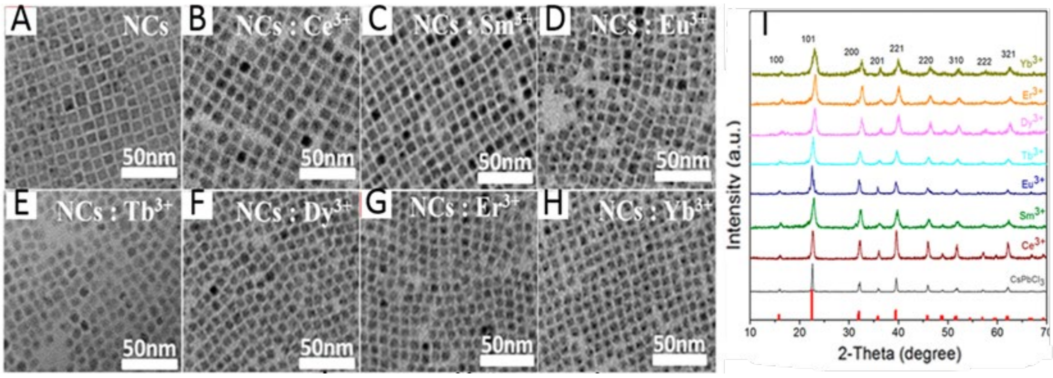

Fig. 4 The RE-doped $CsPbCl_3$ NCs synthesized by HI method. (A–H) TEM (transmission electron microscope) images of Ln^{3+} doped $CsPbCl_3$ NCs (Ln = Ce, Sm, Eu, Tb, Dy, Er, Yb). (I) XRD (x-ray diffraction) patterns of $CsPbCl_3$ NCs doped with Ln^{3+}. Ref. 36. Copyright 2017, American Chemical Society.

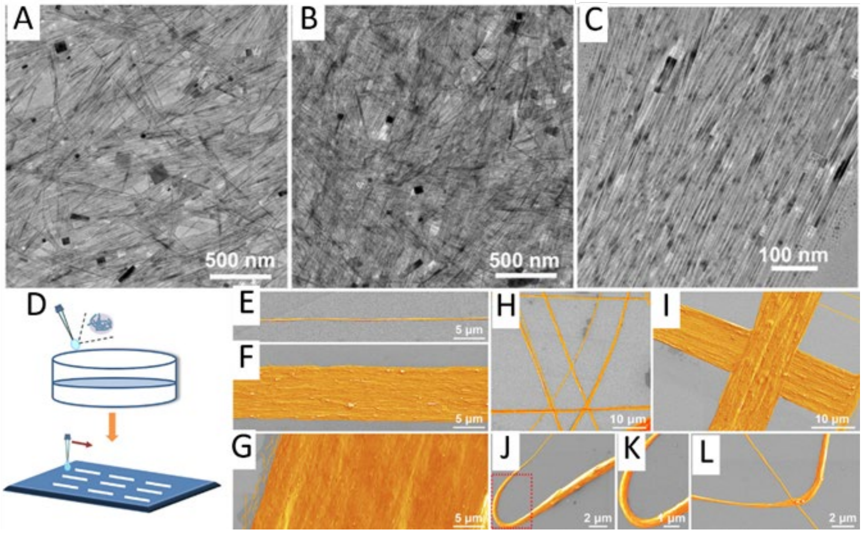

Fig. 5 RE-doped $KMnF_3$ nanowires were synthesized by CP method and. TEM images of (A) $KMnF_3$: Yb/Ho, (B) $KMnF_3$: Yb/Tm, (C) $KMnF_3$: Yb/Er. (D) The nanowires arrays prepared by direct-writing method. SEM images of (E–G) the aligned, (H, I) crossed, and (J–L) curved $KMnF_3$: Yb/Er NWs on Si substrate. Ref. 154. Copyright 2018, American Chemical Society.

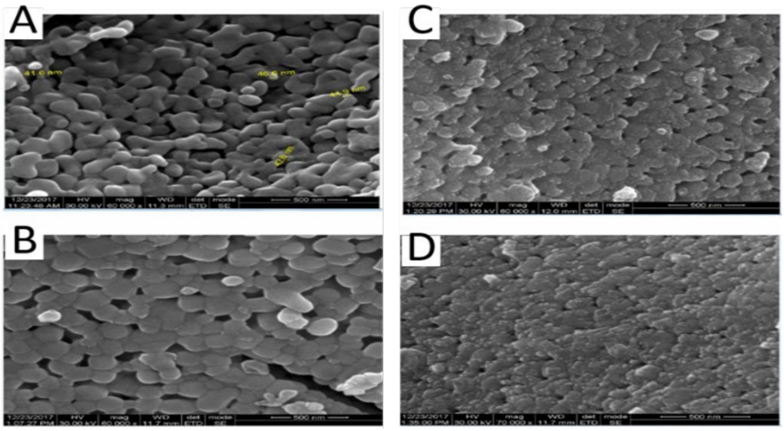

Fig. 6 The $La_{1-x}Na_xFeO_3$ NPTs were synthesized by SG method. The SEM images of samples (A) $LaFeO_3$, (B) $La_{0.95}Na_{0.05}FeO_3$, (C) $La_{0.9}Na_{0.1}FeO_3$, (D) $La_{0.85}Na_{0.15}FeO_3$. Ref. 158. Copyright, 2018 Author(s).

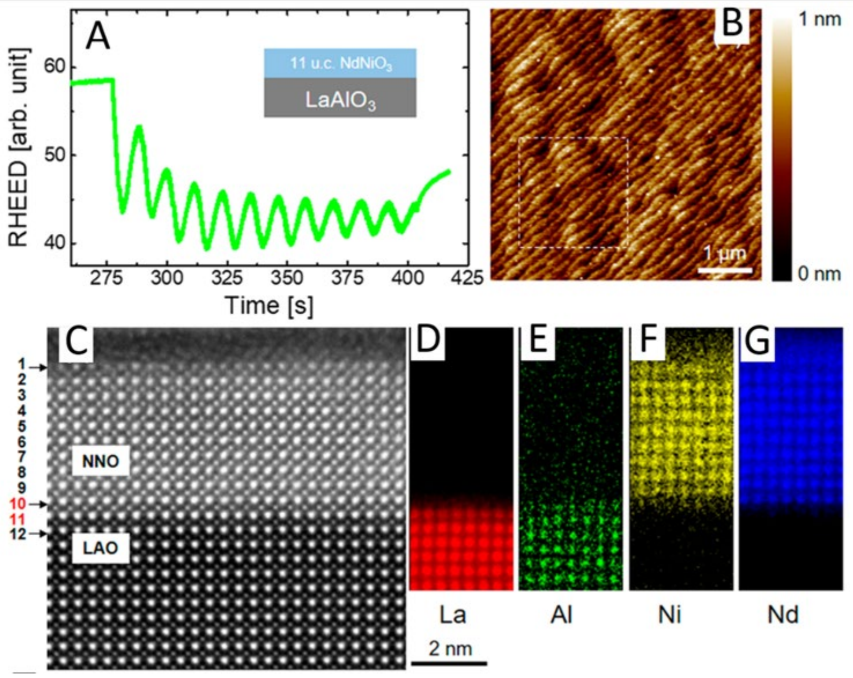

Fig. 7 The growth of $NdNiO_3$ nanofilms onto the substrates of $LaAlO_3$ by PLD method. (A) RHEED (reflection high-energy electron diffraction) oscillations results shown a layer-by-layer growth process. (B) AFM (atomic force microscopy) images of the film gave a stem-and-terrace morphology. (C) HAADF-STEM (high-angle annular dark field, Scanning transmission electron microscope) images of the transverse section of $NdNiO_3$ films and $LaAlO_3$ substrates. (D – G) Atomic-resolution EELS (Electron energy loss spectroscopy) mapping of the La, Al, Ni, and Nd from the edges of the heterojunction. Ref. 141. Copyright 2018, American Chemical Society.

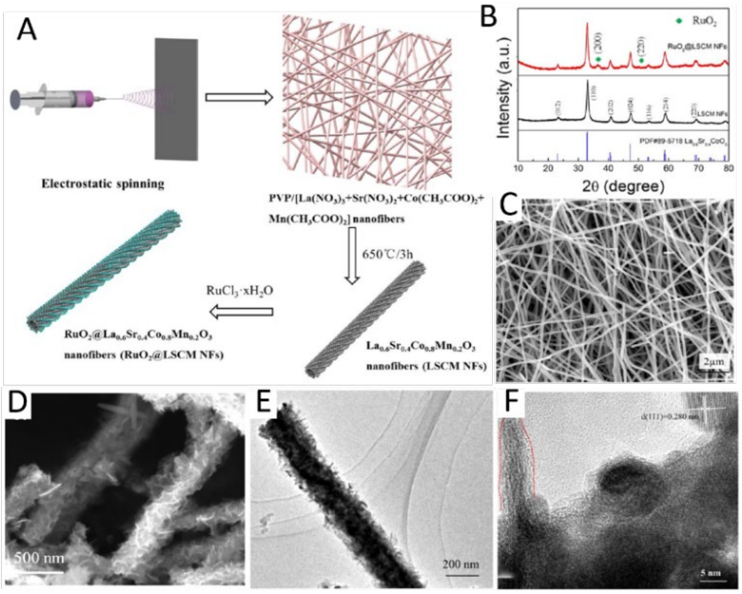

Fig. 8 (A) The schematic illustration of preparing RuO_2@ $La_{0.6}Sr_{0.4}Co_{0.8}Mn_{0.2}O_3$ (LSCM) nanofibers by electrospinning technique. (B) The XRD patterns of LSCM and RuO_2@LSCM NFs. (C) SEM images of RuO_2@LSCM NFs. (D,E) TEM images of RuO_2@LSCM NFs. (F) HRTEM image of RuO_2@LSCM NFs. Ref. 174. Copyright 2017, American Chemistry Society.

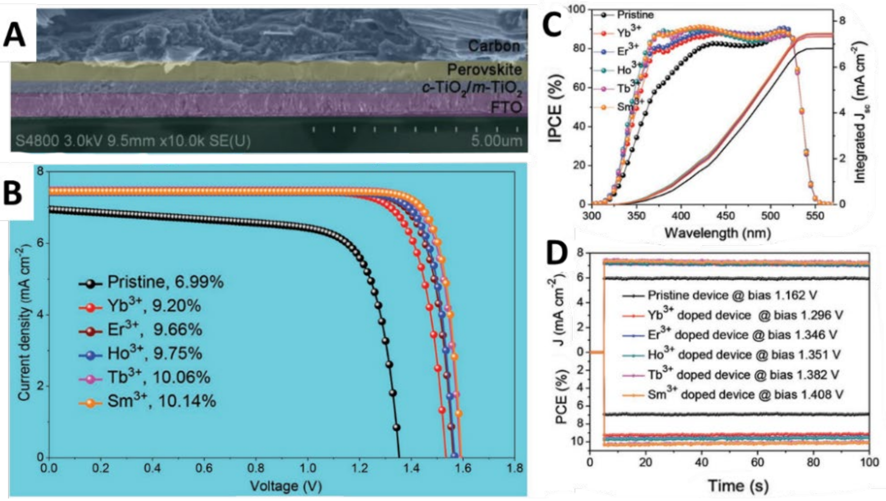

Fig. 9 (A) The images of the cross section of the all-in-organic PSC. (B) The J-V curves of the PSCs with Yb^{3+}, Er^{3+}, Ho^{3+}, Tb^{3+}, Sm^{3+} doped $CsPbBr_3$ perovskite absorbers. (C) The incident photon-to-current efficiency spectra of the PSCs. (D) The power output curves of the PSCs. Ref. 123. Copyright 2018, Wiley-VCH.

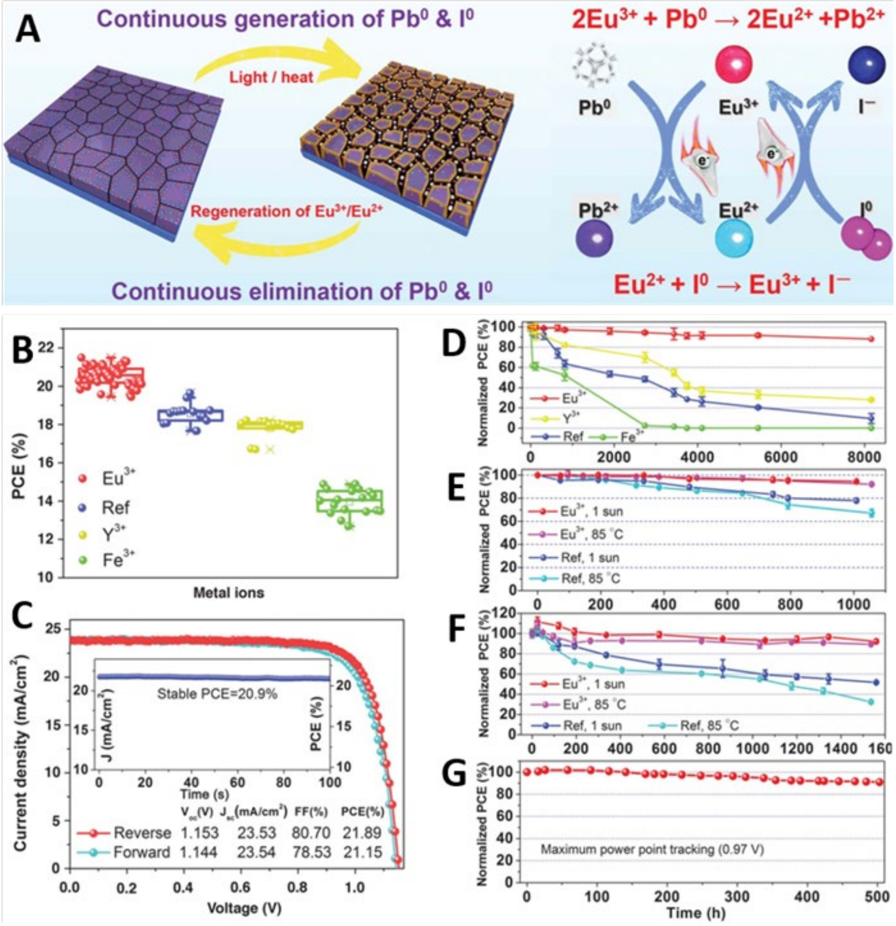

Fig. 11 (A) The mechanism diagram of defect (Pb and I) elimination by Eu^{3+} -Eu^{2+}.(B)The PEC of (FA, MA, Cs)Pb(I,Br)$_3$(Cl) based PSCs with different different M(acac)$_3$ (M=Eu^{3+}, Y^{3+}, Fe^{3+}) incorporation. (C) The performances of Eu^{3+}-incorporated PSCs. (D), (E), (F) and (G) are the long-term stability of the PSCs with different M(acac)$_3$ incorporation. Ref. 9. Copyright 2019, AAAS

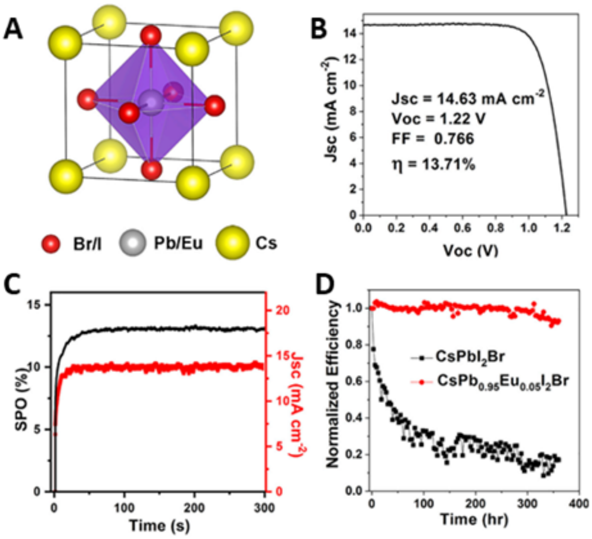

Fig. 10 (A) The crystal structure of europium doped $CsPbI_2Br$. (B) J-V curve of $CsPb_{0.95}Eu_{0.05}I_2Br$ based device. (C) The stable power output of the device at maximum-power point tracking (100 mW cm^{-2} irradiation). (D) Normalized PECE of Eu-doped and undoped $CsPbI_2Br$ devices as a function of working time (under continuous white light irradiation). Ref. 43. Copyright 2018. Elsevier Inc.

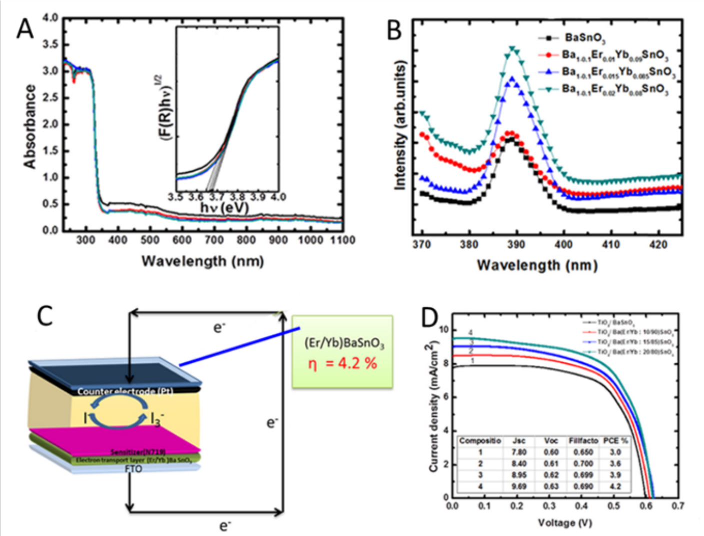

Compositio	Jsc	Voc	Fillfacto	PCE %
1	7.80	0.60	0.650	3.0
2	8.40	0.61	0.700	3.6
3	8.95	0.62	0.699	3.9
4	9.69	0.63	0.690	4.2

Fig. 13 (A) UV–Vis absorption and (B) Photo-luminescence spectra of $BaSnO_3$ and $Er^{3+}/Yb^{3+}:BaSnO_3$ NCs. (C) The schematic diagram of solar cell. (D) The J-V curves of $BaSnO_3$ and $Er^{3+}/Yb^{3+}:BaSnO_3$ NCs. Ref. 101. Copyright 2018, Elsevier Ltd.

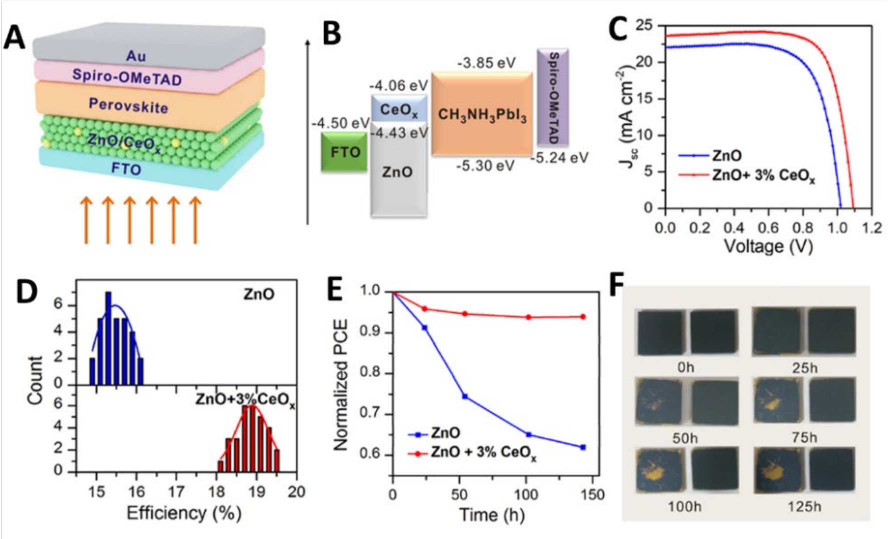

Fig. 12 (A) Schematic images of cell structure. (B) The energy band diagram of the PSCs. (C) Best J-V curves of ZnO and CeO_2/ZnO based PSCs. (D) The PECEs among 30 cells with and without CeO_2 addition. (E)The stability of the cells at 85 ºC (at inert atmosphere). (F) The photos of CeO_2 doped (right) and un-doped (left) perovskite films treatment with the same conditions in (E). Ref. 181. Copyright 2019, American Chemical Society.

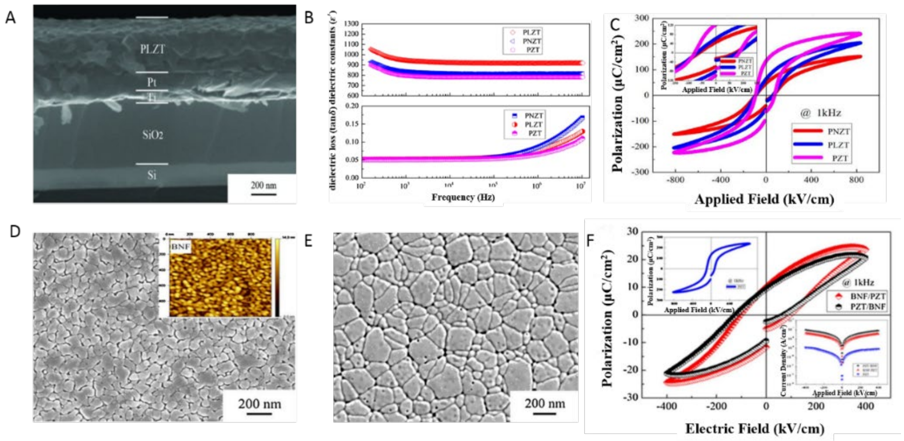

Fig. 15 (A) The cross sectional SEM image of PZT; (B) Dielectric spectroscopy of PZT and its doping series; (C) Comparison of PZT and its partial replacements at 25 V. Ref. 37. Copyright 2018, Springer. (D) (E) Microstructures of both BNF and PZT layer respectively, the inset in (D) is an AFM image of BNF/PZT layer. The thickness of each layer is 300 nm for comparison purposes. (F) P-E loops of PZT-BNF bilayer films, the upper inset in (F) presents the P-E curve of pure PZT film, the lower inset is the DC leakage characteristics of the laminar film. Ref.199. Copyright 2018, Springer.

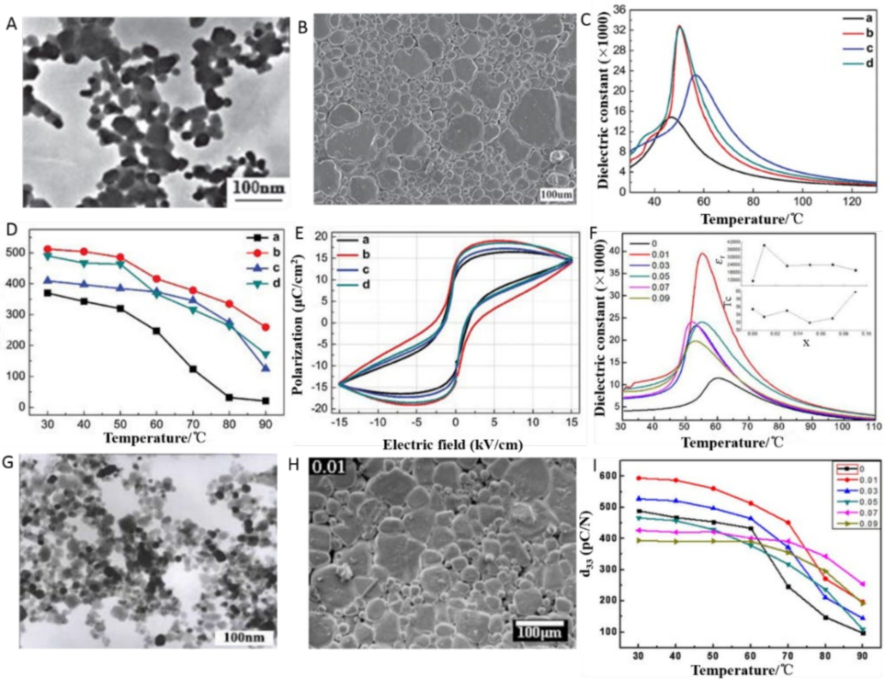

Fig. 14 (A) TEM images of CeO_2 nanoparticles calcined at 800 °C; (B) SEM images of BCTS-nanoCeO_2 (0.03 mol%) ceramics; (C) The temperature-dependent dielectric constant of BCTS-CeO_2 at 1 kHz, the line a, b and c are the ceramics doped with 0, 0.03 and 0.07 mol% nanoCeO_2, respectively, and line d is the ceramics doped with 0.03 mol% micro-CeO_2; (D) The thermal stability of BCTS-CeO_2 ceramics from 30 °C to 90 °C; (E)Polarization-electric field hysteresis loop of BCTS-CeO_2 ceramics at 3.5 kV/cm and 1 Hz. Ref. 192. Copyright 2019. American Scientific Publishers. (F) Temperature-dependent dielectric constant for the BCTS-Y ceramics at 1 kHz; (G)TEM images of Y_2O_3 nanoparticles calcined at 900 °C; (H) SEM images of the BCTS-Y ceramics with 0.01% Y_2O_3; (I) The thermal depoling behaviour of the BCTS-Y ceramics. Ref. 193. Copyright 2017. Wiley-VCH.

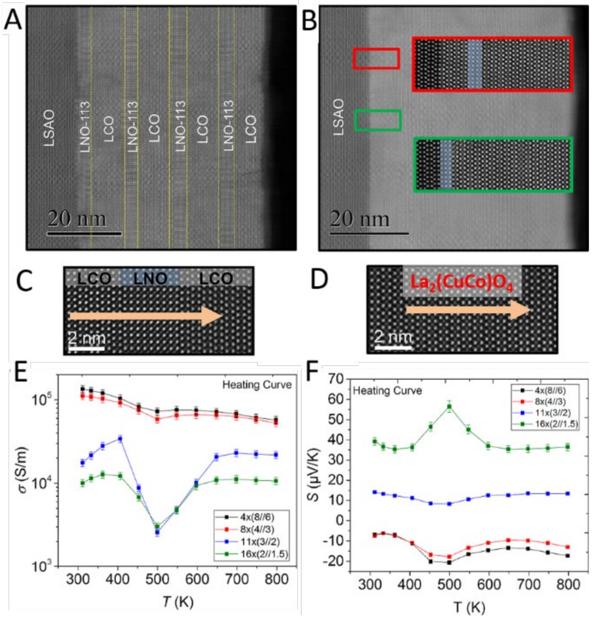

Fig. 16 HAADF images of k×(n//m), where k is the layer number of $LaNiO_3$-La_2CuO_4 heterojunctions, n is the number of $LaNiO_3$ unit cell, and m is the number of La_2CuO_4 unit cells. (A, C) 4× (8//6) and (B, D)16× (2//1.5). (E, F) Temperature-dependent curves of the conductivity and Seebeck coefficient of the heterojunction layers. Ref. 202. Copyright 2018, American Chemical Society.

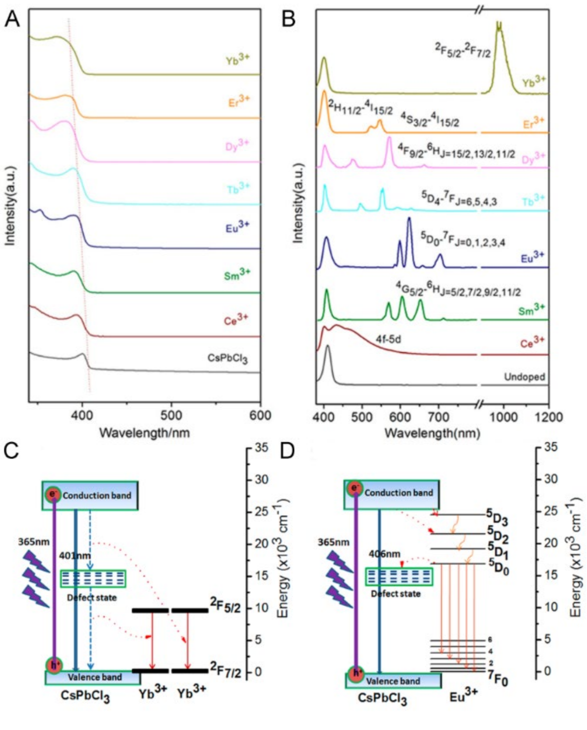

Fig. 17 (A) Absorption spectra and (B) emission spectra of Ln^{3+}-doped $CsPbCl_3$ NCs. The energy level diagrams and possible luminescence mechanism of Ln^{3+}-doped $CsPbCsCl_3$ NCs: (C) doped with Yb^{3+}; (D) doped with Eu^{3+}.Ref. 36. Copyright 2017, American Chemical Society.

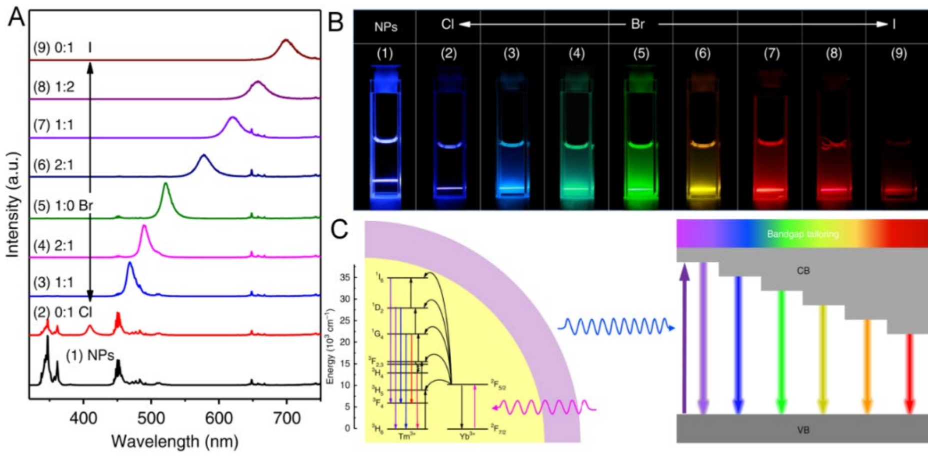

Fig. 19 (A) The emission of $LiYbF_4$:0.5% Tm@$LiYF_4$ core/shell NPs and the NP-sensitized $CsPbX_3$ QDs (X=Cl, Br, I) under the laser excitation (980 nm). (B) The photographs of the samples (from $CsPbCl_3$, $CsPbBr_3$ to $CsPbI_3$) under 980 nm illumination, adjustable color from blue to red. (C) Upconversion turning in $CsPbX_3$ QDs sensitized by $LiYbF_4$:0.5%Tm@$LiYF_4$ nanoparticles. Ref. 224. Copyright 2018, Springer Nature.

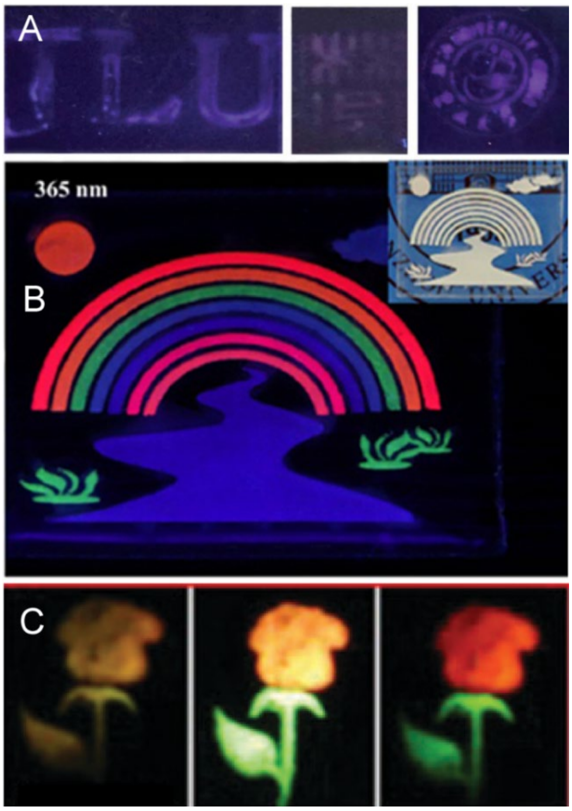

Fig. 18 (A) The patterns printed by CsPb $(Cl_{0.7}F_{0.3})_3$:La^{3+} QDs inks on the paper under the 365 nm UV irradiation. Ref. 225. Copyright 2019, Royal Society of Chemistry. (B) Fabrication of RE^{3+}-doped $LiNbO_3$ (RE = Pr, Tm, Er, Yb) luminescent rainbow river logos printed on a PDMS substrate. Ref. 226. Copyright 2019, American Chemical Society. (C) The plantlet (flowers and leaves) images printed by the inks of $KCdF_3$:2% Yb^{3+}, 5% Mn^{2+}, 0.01% Er^{3+} and $KCdF_3$:2% Yb^{3+}, 5% Mn^{2+}, 0.01% Ho^{3+}, respectively. Ref. 227. Copyright 2019, Royal Society of Chemistry.

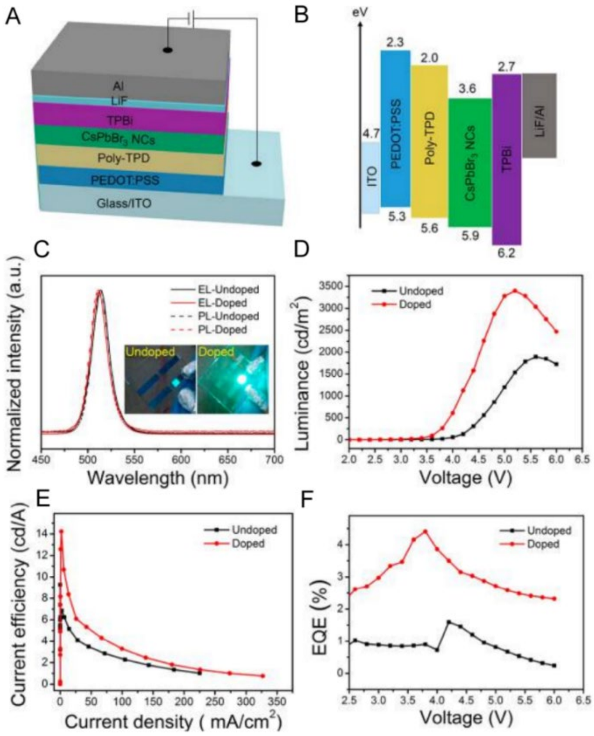

Fig. 20 (A) The structure diagram of the LEDs. (B) The band distribution in each functional layer of the device. (C) PL and EL spectra of the $CsPbBr_3$ and Ce^{3+} doped $CsPbBr_3$ samples and corresponding devices. (D) The luminance changes with the driving voltage of the devices. (E) Relationship between current efficiency and current density of these devices. (F) The relationship between the driving voltage and the EQE of these devices. Ref. 11. Copyright 2018, American Chemical Society.

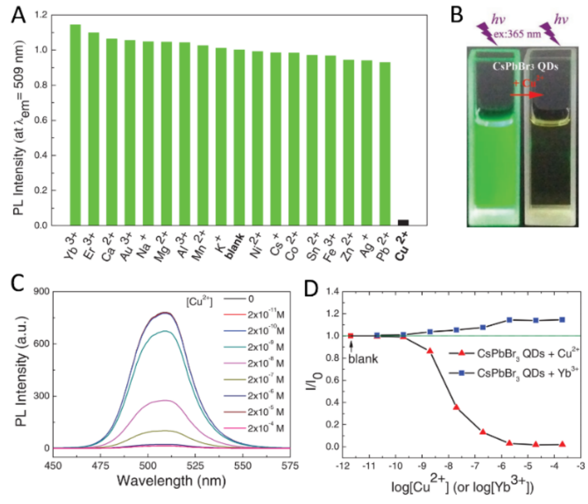

Fig. 21 (A) The PL intensity of $CsPbBr_3$ QDs (≈1.0×10^{-9} M) with addition of different metal ions (2.0×10^{-6} M). (B) The images of $CsPbBr_3$ QDs in cyclohexane without and with Cu^{2+} under UV light. (C) The PL spectra of $CsPbBr_3$ QDs with addition of different amounts Cu^{2+}. (D) The PL intensity of $CsPbBr_3$ QDs changes with addition of Cu^{2+} and Yb^{3+}. Ref. 128. Copyright 2017, WILEY-VCH.

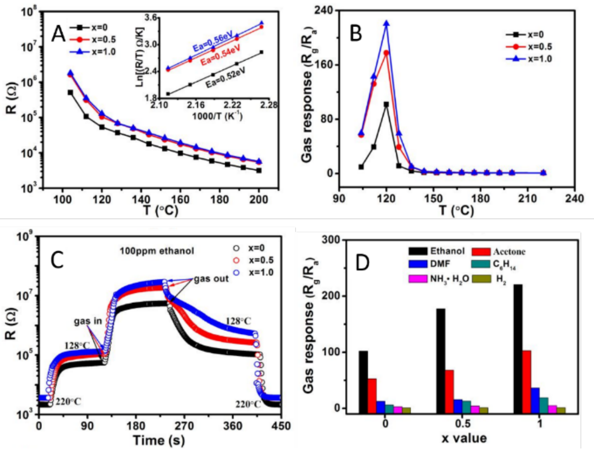

Fig. 22 (A) The resistance of $LaFeO_3$-x% $HAuCl_4$ (x=0, 0.5, 1.0) in air (104 A) The resistance of $LaFeO_3$-x% $HAuCl_4$ (x=0, 0.5, 1.0) in air (104 – 200 ºC), inset: the curves of lnR/T *vs.* 1000/T (168 − 200 ºC). (B） Temperature dependence of ethanol (100 ppm) gas response. (C) The response curves of resistance to ethanol (120 ºC, 100 ppm). (D) The response performances of different gases (120 ºC, 100 ppm). Ref. 129. Copyright 2019, American Chemical Society.

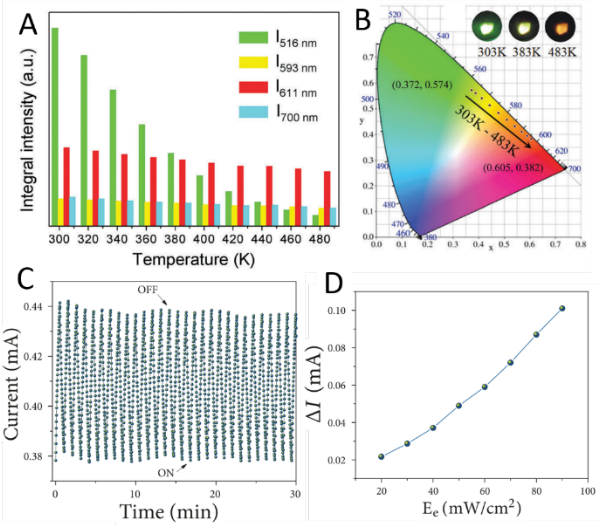

Fig. 23 A) Temperature (303 – 483 K) dependent PL emission intensities of $CsPbBr_3$ and Eu^{3+} at different peaks (λ_{ex} = 393 nm). B) The CIE (x,y) diagram of the emission colour with different temperatures, inset: photos of the samples under different temperature. Ref. 236. Copyright 2018, Royal Society of Chemistry. C) The electrical current of $DyCoO_3$ pellet under on/off cycles (30 s) UV irradiation. D) Quantitative current response of $DyCoO_3$ to UV light (with different Ee values). Ref. 238. Open Access.

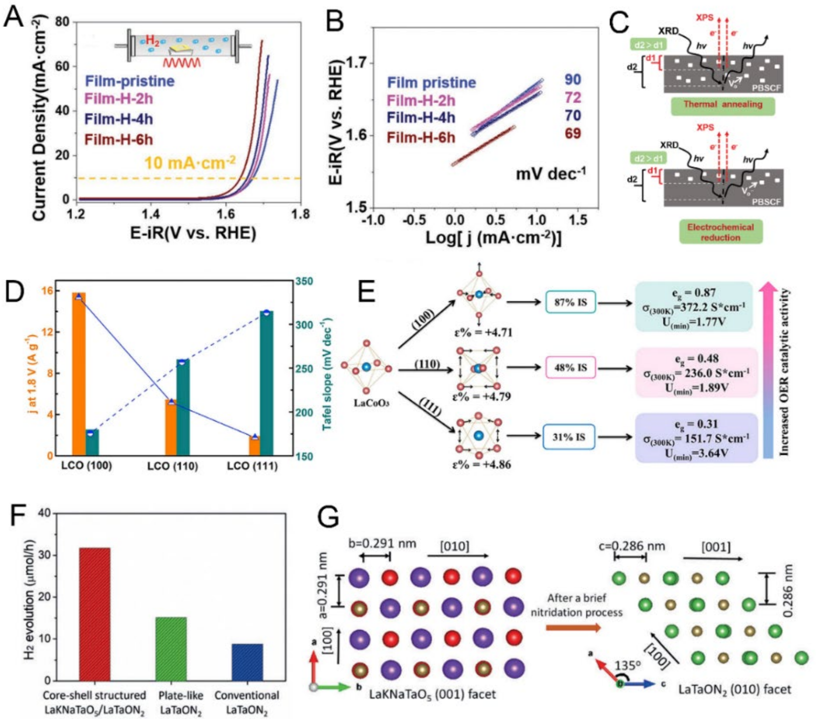

Fig. 24 (A) The polarization curves and (B) Tafel plots of OER for the $PrBa_{0.5}Sr_{0.5}Co_{1.5}Fe_{0.5}O_{5+\delta}$ (PBSCF) thin films after thermal annealing. (C) Schematic diagram of the difference in oxygen vacancy distribution in PBSCF thin film after annealing and electrochemical reduction. Ref. 252. Copyright 2019, WILEY-VCH. (D) Comparison of the reactivity (solid line) and Tafel slope (dashed line) for obtained LCO films. (E) Schematic diagram of the relationship between spin configuration (free energy, conductivity and e_g electrons filling status) and OER activity of the LCO films with different orientation. Ref. 245. Copyright 2017, Elsevier Inc. (F) Direct comparison of H_2 production rates for the core–shell-structured $LaKNaTaO_5/LaTaON_2$, the plate-like $LaTaON_2$ and the conventional $LaTaON_2$ powder. (G) The crystal structures views of the (001) facets of $LaKNaTaO_5$ and (010) facets of $LaTaON_2$. Ref. 31. Copyright 2019, WILEY-VCH.

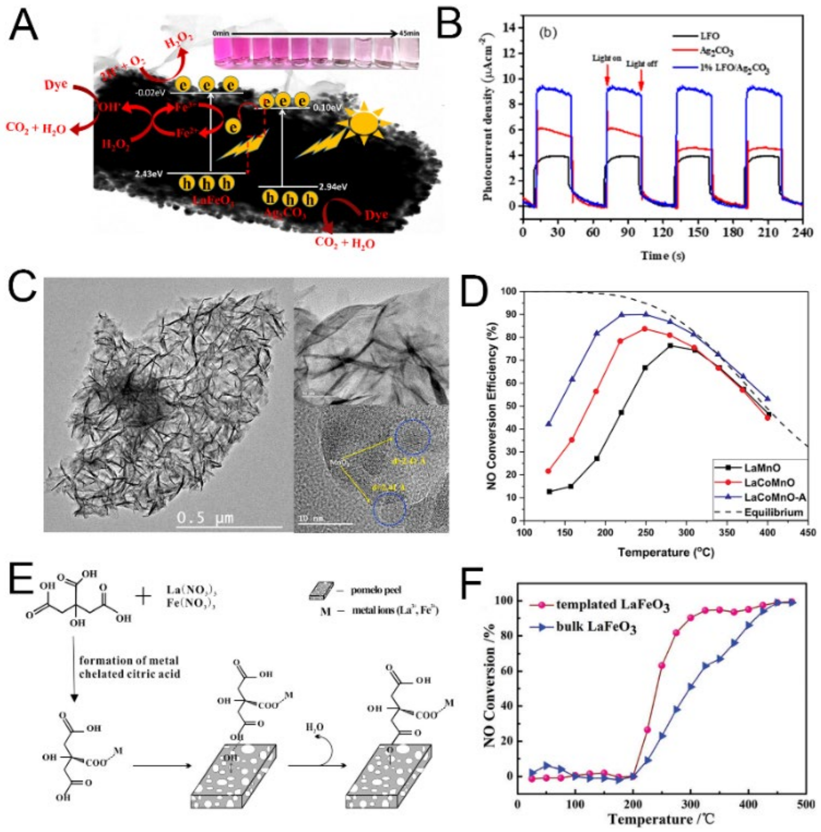

Fig. 25 (A) The HRTEM image and the scheme diagram of the mechanism for the generation of different reactive oxygen species. (B) Photocurrent tests of the pure LFO, Ag_2CO_3, and 1% LFO/Ag_2CO_3 samples. Ref. 113. Copyright 2019, American Chemical Society. (C) The HRTEM of the LaCoMnO-A sample. Ref. 265. Copyright 2019, Elsevier B.V. (D) NO conversion for studied LaMnO, LaCoMnO and LaCoMnO-A samples. (E) The supposed scheme diagrams for adsorption of metal ion precursors on the surface of pomelo peel. (F) NO conversion of template $LaFeO_3$ and bulk $LaFeO_3$ samples at different temperatures. Ref. 269. Copyright 2017, the Partner Organizations.

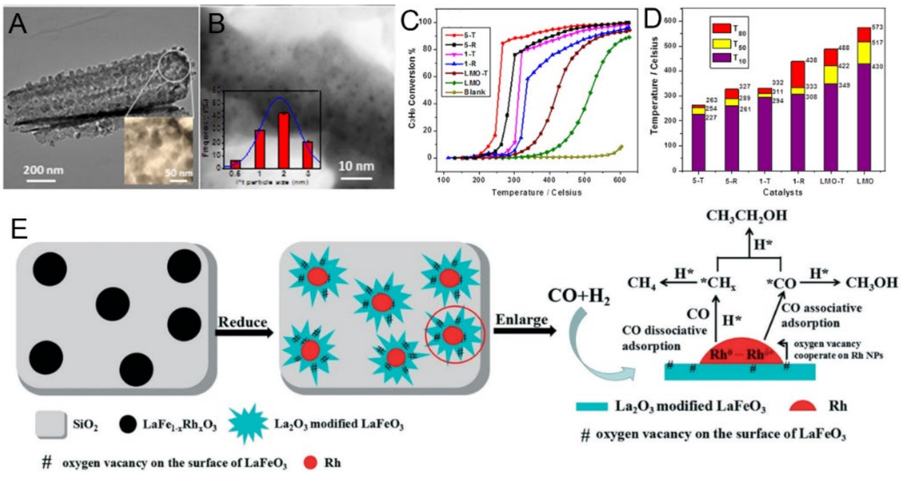

Fig. 26 (A) The TEM image of a mesoporous $LaMnO_3$ nanotube with Pt loading and (B) HAADF images of aged $LaMnO_3$ nanotube with Pt nanoparticles. (C) Propane conversion over all tested catalysts. (D) Bar charts of propane conversion over all samples tested at T10, T50 and T80. Ref. 274. Copyright 2018,Wiley-VCH. (E) Scheme diagram of the structure conversion of $LaFe_{1-x}Rh_xO_3/SiO_2$ during the reduction process and reaction pathways among over the catalyst. Ref.134. Copyright 2019, The Royal Society of Chemistry.

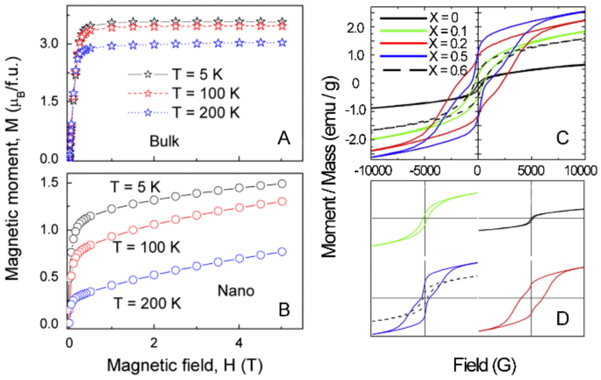

Fig. 27 Field dependences of the magnetizations measured on bulk (a) and nanosized (b) samples at different temperatures below its Curie points. Ref. 293. Copyright 2007 IEEE. The magnetic hysteresis curves for $PrAl_xFe_{1-x}O_3$ at x = 0.0, 0.1, 0.2, 0.5 and 0.6; (c) overlaid, (d) separated. Ref. 294. Copyright, 2014 Elsevier.

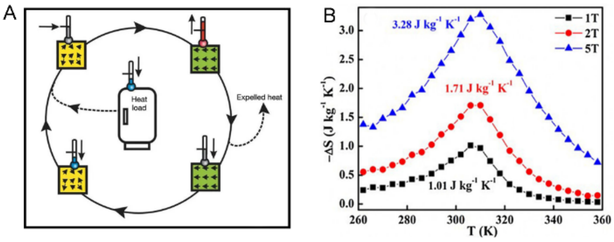

Fig. 28 (A) Mechanism for cryogenic magnetic refrigeration. Ref. 299. Copyright 2002, Springer Nature. (B) The magnetic entropy change at 10 kOe, 20 kOe and 50 kOe magnetic fields. Ref. 23. Copyright 2017, Elsevier B.V.